SIZE EFFECTS IN ^{3}He FILMS

by

Mark Russel Freeman

Materials Science Center

Cornell University
ITHACA, NEW YORK
14853

This report has been prepared by
the Central Report Facility of the
Materials Science Center.

SIZE EFFECTS IN ^{3}He FILMS

by

Mark Russel Freeman

SIZE EFFECTS IN ^{3}He FILMS

A Dissertation

Presented to the Faculty of the Graduate School

of Cornell University

in Partial Fulfillment of the Requirements for the Degree of

Doctor of Philosophy

by

Mark Russel Freeman

August, 1988

SIZE EFFECTS IN ^{3}He FILMS

Mark Russel Freeman, Ph.D.

Cornell University 1988

This thesis addresses two related problems. One is the effect of small geometries on the superfluid phases of ^{3}He, and the other is the nature of the scattering of ^{3}He quasiparticles at surfaces. The sample consists of 300 nm-thick films of ^{3}He created by confining the liquid between closely spaced Mylar sheets. The fluid is probed simultaneously by two methods. Nuclear magnetic resonance monitors the spin dynamics of the system, yielding information with which I identify the superfluid phase. The hydrodynamic response of the fluid is determined from the period and damping of a torsion pendulum which generates oscillatory motion of the substrate. In the normal and superfluid phases alike, this response is strongly dependent on microscopic details of the quasiparticle interactions with the surface.

I compare the superfluid measurements to the Ginzburg-Landau model in which the order parameter vanishes at the walls (the so-called diffusive boundary condition). Results for the superfluid transition temperature, the superfluid density and the NMR frequency shift are in good quantitative agreement. Also in accord with theory, I find that the superfluid A phase is stabilized by the walls over a wide range of pressures and temperatures at which the B phase is stable in bulk. In contrast with calculations, however, I do not observe the A-B phase boundary.

The ^{3}He-solid interface is modified in these experiments by the introduction of small quantities of ^{4}He. ^{4}He plates out preferentially on the surfaces at low temperatures, an effect which persists until a layer several atoms deep has been built up. The

boundary condition on the order parameter is observed to vary continuously with the surface ^{4}He coverage, spanning almost the full range between the limits corresponding to diffusive and specular quasiparticle scattering.

I find other interesting boundary-related phenomena in the normal phase. For pure ^{3}He, exchange averaging of the liquid and adsorbed surface layer NMR signals is seen. The torsion pendulum experiments reveal an apparent decrease in the friction between the ^{3}He and the substrate occurring at the superfluid transition in the surface ^{4}He layer. This slip signature is used in turn to track the evolution of a ^{4}He film under ^{3}He pressure. The results indicate that ^{4}He film superfluidity on mylar persists to pressures well above the bulk solidification point of ^{4}He.

Biographical Sketch

Mark Russel Freeman was brought into this world on March 17, 1960 at the University of Alberta Hospital in Edmonton. He has enjoyed the continued, tangible presence of a university in his life from the beginning. Links between things are important to him. Mark remembers his childhood with great fondness, and not only because his memory is weak and he tends to look on the bright side. He was eleven years old before he understood that the life which he knew would not last forever. Little more than the comfort of forced-air heating in winter was required to carry him through this spiritual crisis.

Mark's early education took place in the community of Laurier Heights, mostly at the combined elementary/junior-high school. Some of the teachers at this school were the finest he has had. He went on to Ross Sheppard Composite High School, where his interest in experimental physics began to develop, and found some outlet with the help of bits of high voltage equipment from his father's lab. Graduating from Ross Shep in June of 1977, he enrolled in the physics program at the University of Alberta. This was a very positive experience, and was immeasurably enhanced by various summer jobs around the country. On October 13, 1979, Mark met Jennie Lambert at a dance in Dinwoodie Lounge, and she quickly became a central character in all that was to follow.

On the advice of a couple of trusted mentors, he came to Cornell, sight unseen, in 1981. Also in 1981, Jennie foolishly agreed to marry him. It was a good year for making decisions.

Mark and Jennie are about to move to Yorktown Heights, where they will await the (imminent) arrival of their first child before Mark begins postdoctoral work at IBM. They plan eventually to return to the true north, strong and free.

To

Jennie

Acknowledgements

I have truly enjoyed working in the low temperature group for the past six years. I thank my advisor, Bob Richardson, for his support during this time. I particularly valued the opportunities, such as to attend many terrific conferences, that are often not the lot of a graduate student, but were made possible by Bob. The other key ingredients of the group – John Reppy, Dave Lee, Jeevak Parpia and Eric Smith – have all been sources of valuable advice and have set enduring examples. John Reppy and John Wilkins deserve special thanks for serving on my special committee.

Jennie Lambert helped me decide to give low temperature physics a try in the first place. She has been tremendously patient and supportive during the evolution of that decision into its present condition. She encompasses the real meaning of life.

I owe great debt of gratitude to the other students with whom I have spent so many nights and days in the trenches. From Doug Wildes I learned to be patient and careful, before the apparatus had a chance to teach me the hard way. Mike Roukes was a particularly important influence. His vision of the SQUID project kept me in H-corridor, and he also got the ball rolling when it finally came time for me to move on to the next phase of life. Thanks for many things go to Bob Germain, friend and colleague, hoser and machining animal, without whom this experience would have been more like sailing in a gentle breeze instead of an invigorating, brisk wind.

Several shorter term collaborations also evoke fond memories. I thank Erin Houseman and Lorinda Opsahl for the time they spent on the nuke rig team (step on their toes if you're not sure who is who). I also had a lot of fun working with Roman Movshovich (the human fountain).

Much of what I have learned has been by osmosis from other people. Dave McQueeney set the standards for construction and automation, and for being generally amazing. Tom Gramila set the standards for doing NMR and for listening to blues.

I enjoyed many conversations with Kenny Blum, and am forever grateful to him for discovering the rupture of a cooling water line inside the shielded room, shortly after the course of experiments reported in this thesis began. Nick Bigelow and Yue Hu were large contributors to the generally friendly atmosphere in the group. Numerous other members of the community have helped me to maintain a rational perspective. The Edmonton Oilers lifted my spirits with *four* truly impressive Stanley Cup victories.

I benefited from stimulating conversations with various people during their extended visits to the laboratory, in particular Erkki Thuneberg, Moses Chan and Jason Ho.

It is a pleasure to recall the many occasions on which the staff and facilities of LASSP and of the Materials Science Center have enabled me to accomplish things better, faster, or even at all. I have been supported by the Graduate School of Cornell University, the Natural Sciences and Engineering Research Council (Canada), the Alberta Heritage Fund, and by the National Science Foundation and the NSF through MSC.

Finally, to acknowledge debts that have accumulated over many more years than the ones I have so far mentioned, I thank my parents for their dependable and effective support, and my sister Michele for her concern and openness.

Table of Contents

List of Tables

List of Figures

Chapter 1

Introduction

... and that sets up a link of things. Is the person next to you cold? Are there other people in the world who are cold? ... All sorts of things occur to you.

Wallace Shawn and Andre Gregory

This thesis documents the results of experiments on helium films created by confinement between closely spaced mylar sheets. The physical effects of particular interest here are created by reducing the thickness dimension of the films to the scale of the so-called *correlation length* of the ^{3}He superfluid phase, which is the distance over which substantial variations of the order parameter characterizing the macroscopic quantum condensate can occur. These effects are discussed in Section 1.2. Microscopic details of the boundary often dominate the observed behaviour in these situations. In the ^{3}He system the boundary can conveniently be altered by the introduction of small quantities of ^{4}He. The history of our measurements with dilute ^{4}He-^{3}He mixtures begins in Section 2.4. We continue in Chapter 3 with an account of our initial attempts to study the evolution of the ^{4}He -rich surface layer as a function of pressure, using the ^{3}He as both hydraulic medium and probe.

The present chapter begins with a discussion of size effects in general terms. In Section 1.1 we point out some other condensed matter systems in which phenomena analogous to those which we observe have been studied. Superfluid ^{3}He and the Ginzburg-Landau description of a p-wave superfluid are introduced in Section 1.2.

This is followed by a presentation of the predictions of the theory when the smallest dimension of a ^{3}He sample is comparable to, but still greater than, the temperature dependent correlation length. Section 1.3 establishes the context of other experimental work related to ours. When the size shrinks below the correlation length, qualitatively different behaviour associated with reduced dimensionality may be observed. This is a territory uncharted by experiments. One of the goals of the present work is to assess the possibility of gaining access to this regime. We find it to be feasible, and Section 1.4 outlines some of the theoretical predictions. Finally, we summarize the results of Chapters 2 and 3.

1.1 Size Effects

In a trivial sense, size effects are omnipresent. The sample is of finite size in any real experiment, and therefore has boundaries which at some level influence the measurement. To probe bulk properties this influence must be immeasurably small or otherwise negligible. This is the situation when all of the sample dimensions are much larger than the length scales on which the physics is determined, The results are independent of the sample size in this limit. A breakdown of the bulk approximation heralds the onset of the size effect regime.

Examples of size effects occur most frequently in the physics of transport. The flow of a classical gas when the mean free path is longer than the diameter of the tube was considered by Knudsen[1]. Electrical transport in thin metal films was treated by Thomson[2] and later by Fuchs[3] and by Sondheimer[4]. The mean free path, l_0, of conduction electrons in bulk metals at low temperatures is limited by scattering at impurities and defects. In unannealed OFHC copper, for example, it is typically a few micrometers. The resistivities of clean films which are thinner than this depend strongly on surface characteristics. Diffusely scattering surfaces limit the mean free

path to approximately the film thickness. Specular surfaces preserve the bulk resistivity, ρ_0, as may be easily seen if one imagines 'unfolding' all of the surface reflections. In the Fuchs-Sondheimer model, the resistivity of a film is written[5]

$$\rho = \rho_0 \left[1 + \frac{3}{8}\left(1 - s\right)\frac{l_0}{d} \right] \tag{1.1}$$

where s is the fraction of surface reflections that are specular and d is the thickness of the film. The magnitude of the size effect is inversely proportional to the dimensionless width, $w = d/l_0$.

It is often possible to demonstrate the importance of the boundary condition by changing it with adsorbed gas. An example is shown in Figure 1.1 . The resistivity change of a 10 nm thick copper film on glass at liquid nitrogen temperature is plotted as a function of CO coverage, n, on its exposed surface. In order to obtain a continuous film, the copper is deposited at 77K. It is crystallized by an anneal above room temperature, but the crystallite size is limited to about the film thickness. The resistivity increase can be explained by additional scattering sites at the surface caused by the CO. The monolayer coverage is somewhere around $10^{15}/\mathrm{cm}^2$. At coverages small compared to this, the specularity parameter changes linearly with n, and the resistivity change, $\Delta\rho(n)$, has an initial slope proportional to ρ_0/w. At higher coverages, the surface can again begin to appear smoother.

An example on a more macroscopic scale arises in thermal transport in insulating single crystals. Figure 1.2 shows some results[6] for a silicon bar with a smallest dimension of 5 mm. The phonon mean free path is initially 10 cm and decreases abruptly as gas adsorbs on the surface. The effect with Ne saturates when the mean free path is double the rough surface limit of 5 mm. This can be characterized as 50 % specularity. Sensitivity to the wavelength of the excitations is apparent in the data. The thinner gas films have less effect as the temperature drops and the thermal phonon wavelength increases.

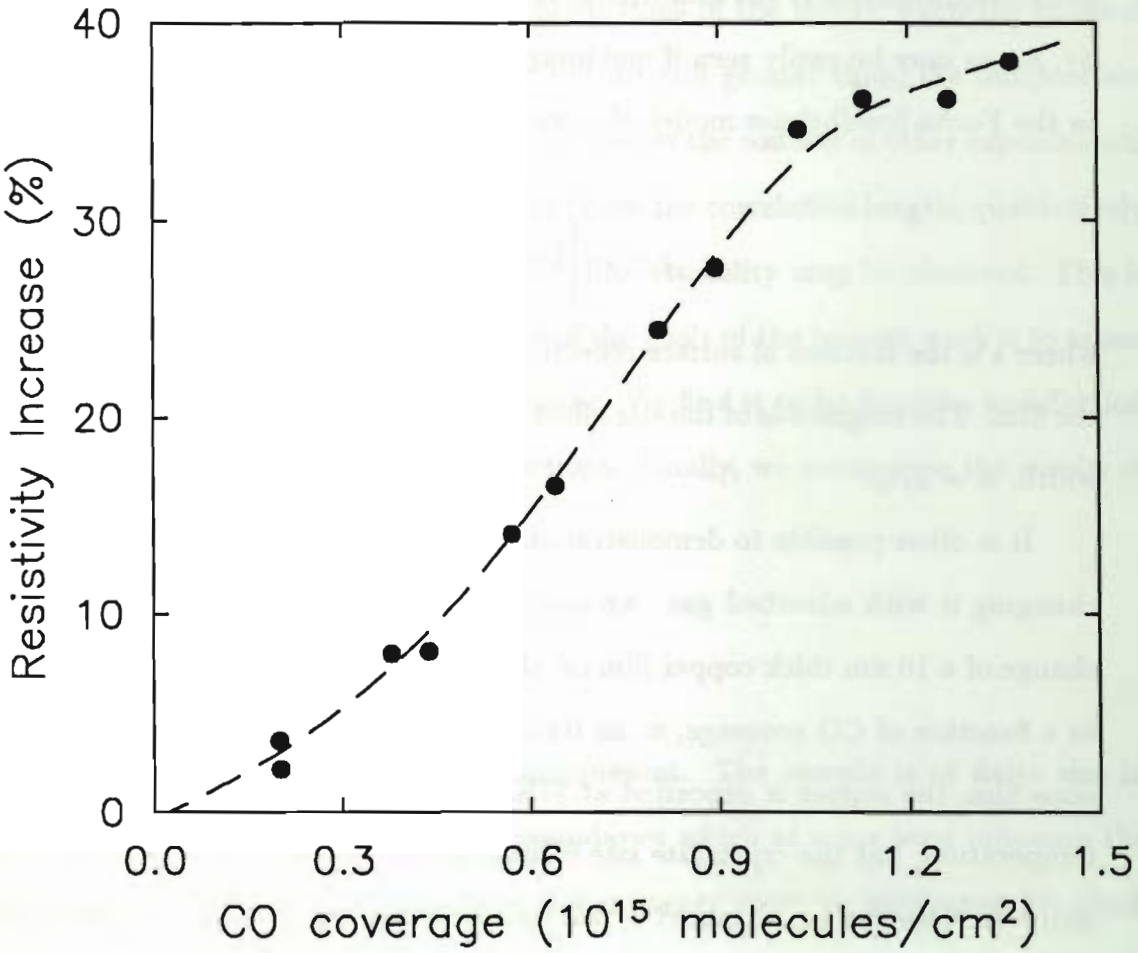

Figure 1.1

Demonstration of the importanceof surface scattering by the resistivity increase of a 10 nm Cu film as a function of carbon monoxide coverage. The measurements were made at 77 K. After Ref. 5.

We also use gas adsorption in the present work to change the boundary condition. This is discussed beginning in Section 2.4. In our case the sign of the effect is different – that is, the tendency of the gas is to make the surfaces more specular. Our primary interest here is not transport properties, however, but the effect of confined geometry and the boundary condition on a phase transition (the transition to superfluidity in ^{3}He). A well established analogy from solid state physics is the case of ferromagnetism in thin films. One asks how the Curie temperature, T_C, and the saturation

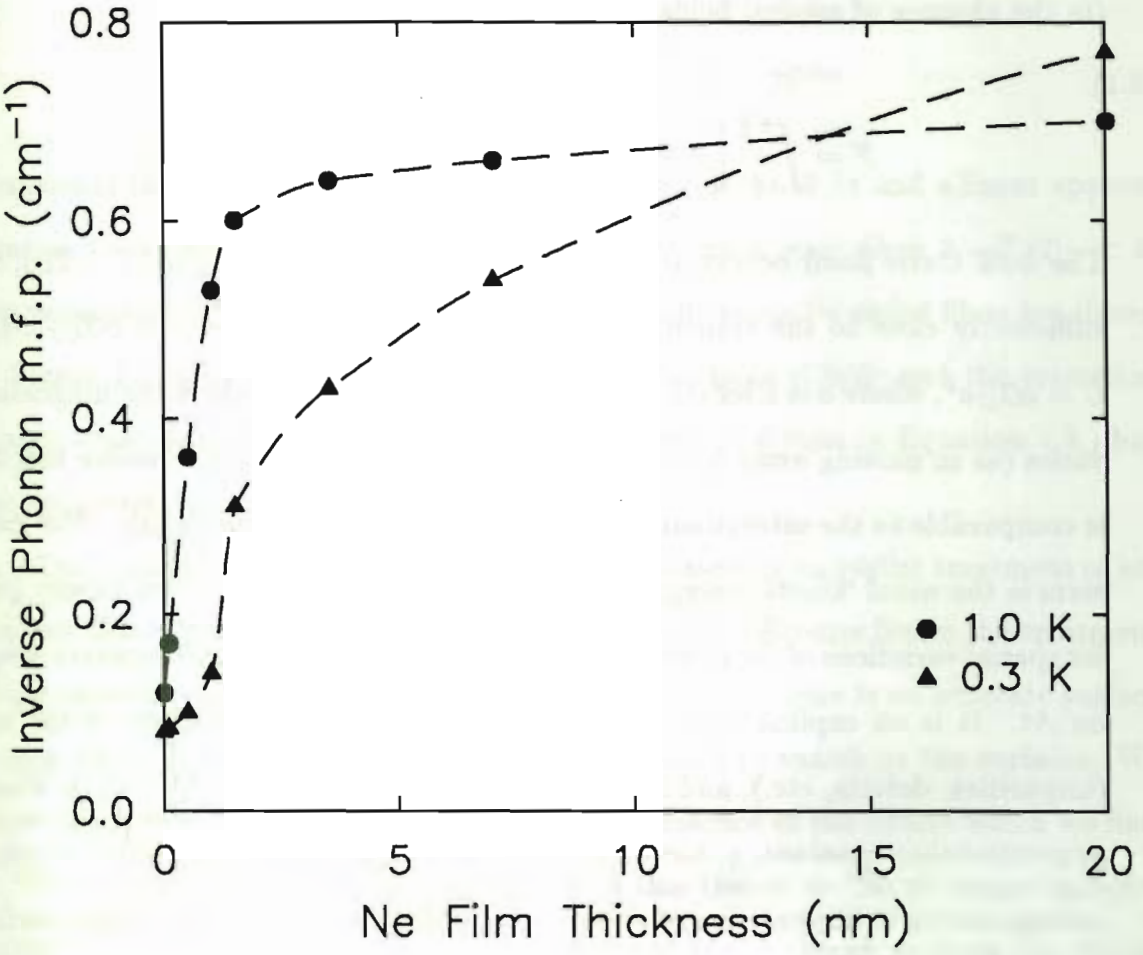

Figure 1.2

The inverse phonon mean free path in a 5 mm single crystal bar of silicon, as determined by thermal conduction. In such a clean system, the size effect dominates even for samples that we would normally consider to be bulk-like. The data are shown as a function of neon gas coverage on the surface, for two different temperatures. After Ref. 6.

magnetization, $M_0 = M(T \ll T_C)$, vary with film thickness. Using the Landau theory of continuous phase transitions[7] (which we hereafter refer to as Ginzburg-Landau theory, from the application to superconductivity[8]), one expands the thermodynamic potential in powers of an order parameter, in this case the magnetization. The thin film is assumed uniform in the plane, and an areal magnetization density, $\mathcal{M}(z)$, is defined which may vary across the thickness of the film. The free energy is written

(in the absence of applied fields)[9]

$$\mathcal{F} = \int_{-\frac{d}{2}}^{+\frac{d}{2}} \left\{ A\mathcal{M}^2 + B\mathcal{M}^4 + C\left(\frac{d\mathcal{M}}{dz}\right)^2 \right\} dz + \mathcal{F}_{surf}. \tag{1.2}$$

The bulk Curie point occurs at the zero of A, which follows $A = \alpha(T - T_C), \alpha > 0$, sufficiently close to the transition. The other coefficients are $B = \alpha T_C / 2M_0^2$ and $C = \alpha T_C a^2$, where a is a length characteristic of the scale on which the magnetization varies (as in moving away from a surface – it is also known as a 'healing length'). a is comparable to the interatomic spacing in typical magnetic materials. The gradient term is the usual 'kinetic energy' contribution which assesses the free energy penalty for spatial variations of the order parameter. $\mathcal{F}_{surf}$ determines the boundary condition on $\mathcal{M}$. It is an explicit term accounting for the physical condition of the surface (impurities, defects, etc.), and is written $\mathcal{F}_{surf} = qC(\mathcal{M}^2(\frac{d}{2}) + \mathcal{M}^2(-\frac{d}{2}))$, where the proportionality constant, q, has units of inverse length. q can be positive or negative, corresponding to suppression or enhancement of the magnetization at the surface.

The free energy functional is minimized to solve for the magnetization. When $q > 0$, the Curie temperature and the magnetization in the film are smaller than the bulk values because of the reduction at the surface. In the limit $qd \gg 1$, the ferromagnetic transition in the film occurs at the temperature

$$T_c^{film} = T_C\left(1 - \left(\frac{\pi a}{2d}\right)^2\right). \tag{1.3}$$

Defining a magnetization fraction (relative to the bulk) for the film,

$$\langle m \rangle = \frac{1}{M_0}\frac{2}{d}\int_0^{\frac{d}{2}} \mathcal{M}(z)dz, \tag{1.4}$$

we find that

$$\langle m \rangle^2 = \frac{8}{3\pi}(1 - \frac{T}{T_C} - \left(\frac{\pi a}{2d}\right)^2), T < T_c^{film}. \tag{1.5}$$

Remember that this assumes an expansion of $\mathcal{F}$ in powers of $\mathcal{M}$ and a linear approximation to A near T_C, and therefore can be relied upon only when $1 - T/T_C \ll 1$. Experimental results for the variation of T_C with thickness for nickel films are shown in Figure 1.3 . These data are not confined to the large d limit and the transition temperature varies with a somewhat different power of d than in Equation 1.3 , but the qualitative effect is apparent.

This analysis of ferromagnetic films is in fact based on an earlier treatment of superfluid films by Ginzburg and Pitaevskii[10]. The main difference lies in the treatment of the boundary condition. For the case of superfluidity, there is no separate surface energy term, and the order parameter, ψ, is assumed to vanish at the surfaces. We quote the results here, because they capture the essence of the effects which we find in ^{3}He, but we remark that the application of this theory to ^{4}He no longer appears justified. In addition to the fact that Ginzburg-Landau theory predicts the wrong critical behaviour for bulk superfluid ^{4}He (by neglecting the fluctuations in the order parameter), the boundary condition on ψ and the concept of a healing length do not seem to apply[11]. The change in the superfluid transition temperature for not too thin films is found to be[10]

$$\frac{\Delta T_c}{T_c} = \left(\frac{\pi \xi}{d}\right)^2, \tag{1.6}$$

where ξ is the correlation length, $\xi = \hbar/\sqrt{2m\alpha}$, and α is again the (temperature independent part of) the coefficient of quadratic term in the free energy. The superfluid density is determined from ψ through[10] $\rho_s = m|\psi|^2$, where m is the mass of the helium atom. The spatial average of the superfluid density in a film is calculated by Kiknadze and Mamaladze[12] who find (for $(1 - T/T_{c,bulk}) \ll 1$)

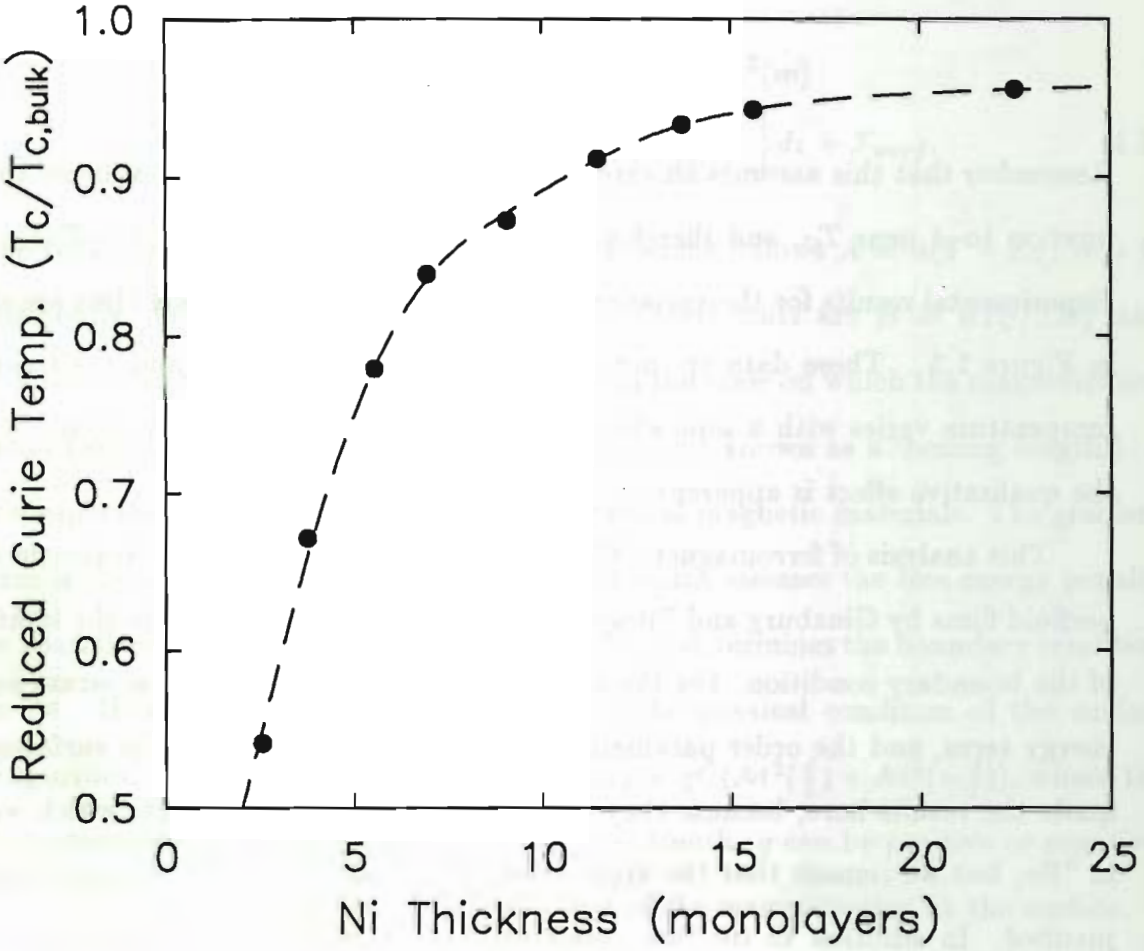

Figure 1.3

The variation of the Curie temperature with film thickness for thin nickel films deposited on a rhenium substrate. The suppression of magnetization near the surface is analogous to the behaviour of the order parameter in superfluid ^{3}He. After Ref. 53.

$$\langle \rho_s \rangle = \frac{4}{3}\rho_{s,bulk}\left(1 - \frac{\pi\xi}{d}\right). \tag{1.7}$$

Such a discussion can also be applied to an ordinary superconducting film. The Ginzburg-Landau model has a microscopic basis in this case, as shown by Gor'kov in his derivation from the Bardeen-Cooper-Schrieffer (BCS) theory[13]. (Of course,

the magnetic results can also be derived from a microscopic perspective – see Ref. 14. In the case of superconductivity, the boundary condition also can enhance[15] or diminish[16] the order parameter.)

1.2 Superfluid ^{3}He in Confined Geometries: Theory

The superfluid state of ^{3}He is of the BCS type and admits of a Ginzburg-Landau description in the transition region. Qualitatively this case is similar to any other continuous phase transition, such as the ferromagnetic transition discussed above. The complication is that the p-wave order parameter has 18 degrees of freedom which can lead, in principle, to a wide variety of stable phases. In addition to changes of the transition temperature and the amplitude of the order parameter, the consequences of confined geometry may include the stabilization of states not found in the bulk. The Ginzburg-Landau free energy difference between an s-wave BCS superfluid and the normal phase is written[8] (this is Equation 1.2 with a change of notation and no surface term)

$$\mathcal{F} = -\alpha|A|^2 + \beta|A|^4 + K|\nabla A|^2 \tag{1.8}$$

where A is a complex scalar related to the order parameter (energy gap) through $A = \Delta e^{i\phi}$. ϕ is the phase, and $A = \sqrt{\alpha/2\beta}$ in the absence of gradients. α is proportional to $T - T_c$, and the temperature-dependent correlation length is $\xi(T) = \sqrt{K/\alpha}$.

The initial experimental evidence for spin triplet, and hence odd angular momentum, pairing in ^{3}He was the non-vanishing low temperature susceptibility and the linear splitting of the A transition in a magnetic field. For Cooper pairing in a relative p-wave, A is a complex 3×3 matrix and the free energy becomes (in zero magnetic field)[17]

$$\mathcal{F} = \alpha \mathrm{Tr} A A^\dagger + \beta_1 |\mathrm{Tr} A \tilde{A}|^2 + \beta_2 (\mathrm{Tr} A A^\dagger)^2 + \beta_3 \mathrm{Tr}(A\tilde{A})(A\tilde{A})^* + \beta_4 \mathrm{Tr}(A A^\dagger A A^\dagger) + \beta_5 \mathrm{Tr}(A A^\dagger)(A A^\dagger)^* + \mathcal{F}_{grad} \quad (1.9)$$

$\tilde{A}$ denotes the transpose and $A^\dagger$ the Hermitean conjugate of A. The nuclear dipole interaction is the only coupling between spin and orbital coordinates in this system, and is neglected here. Equation 1.9 is the most general form to fourth order in A which is invariant under rotations in both spin space and real space. The order parameter is often used in the form of a 2×2 matrix in spin space, $\Delta_{\mu\nu} \sim \sum_{\mu\nu} \sigma_\nu A_{\mu\nu} \hat{k}_\nu (i\sigma_y)$. The energy gap is $\mathrm{Tr}\Delta^\dagger\Delta$.

In the jargon of superfluid ^{3}He, 'strong coupling' refers to the changes in the pairing interaction resulting from the formation of the condensate. This is an important effect[18] more so than in the case of electronic superconductivity because there is no separate lattice with which the ^{3}He quasiparticles interact. In the limit of 'weak coupling' we have

$$\alpha = \frac{N(0)}{3}(1 - \frac{T}{T_c}), \quad (1.10)$$

and $\beta_i = \beta_{BCS}\tilde{\beta}_i$, where $\tilde{\beta}_i = (-1, 2, 2, 2, -2)$ and

$$\beta_{BCS} = \frac{7\zeta(3)}{240} N(0) \left(\frac{1}{\pi k_B T_c} \right)^2. \quad (1.11)$$

Strong coupling effects are included as corrections, $\Delta\beta_i$, to the β_i.

The problem of minimizing the free energy for arbitrary β_i is intractable. Fortunately, experimental information can be used to constrain the choices for A. For example[19], $AA^\dagger$ is real and symmetric because there is no spontaneous magnetization. Of particular interest is the case in which the order parameter matrix $\Delta_{\mu\nu}$ is unitary. This is true for two bulk phases, A and B, stable in zero magnetic field. The B phase is isotropic, and can be represented by

$$A_B = \frac{1}{\sqrt{3}} \begin{pmatrix} 1 & 0 & 0 \\ 0 & 1 & 0 \\ 0 & 0 & 1 \end{pmatrix}. \tag{1.12}$$

The A phase energy gap has two point nodes in k-space. It's order parameter is determined by

$$A_A = \frac{1}{\sqrt{2}} \begin{pmatrix} 1 & i & 0 \\ 0 & 0 & 0 \\ 0 & 0 & 0 \end{pmatrix}. \tag{1.13}$$

There exist two other phases with unitary order parameters[20], known as the planar and polar phases. These phases may be stabilized in confined geometries, as we shall now discuss.

Spatial variations of the order parameter and the boundary conditions at smooth and rough surfaces were considered by Ambegaokar, de Gennes and Rainer[21] (AGR). The dominant terms of the gradient free energy are quadratic in the gradients, and AGR write

$$\mathcal{F}_{grad} = \sum_p \{K_L |\nabla \cdot \mathbf{A}_p|^2 + K_T |\nabla \times \mathbf{A}_p|^2\}, \tag{1.14}$$

where the vector $\mathbf{A}_p$ has components A_{pi}. Longitudinal and transverse gradients of the order parameter are governed by different correlation lengths,

$$\xi_L^2 = \sqrt{K_L/\alpha} = \frac{9}{5}\xi_s^2/(1 - \frac{T}{T_c}) \tag{1.15}$$

$$\xi_T^2 = \sqrt{K_T/\alpha} = \frac{3}{5}\xi_s^2/(1 - \frac{T}{T_c}), \tag{1.16}$$

where ξ_s is the low temperature correlation length in the s-wave BCS case,

$$\xi_s = \sqrt{\frac{7\zeta(3)}{48}} \frac{\hbar v_F}{\pi k_B T_c}. \tag{1.17}$$

At an arbitrary boundary the order parameter may not easily separate into longitudinal and transverse components, and the shortest correlation length alone is often referred to[23] as $\xi(T) = \xi(0)/\sqrt{1 - T/T_c}$ (where $\xi(0) = \sqrt{3/5}\xi_s$). Tabulated below is $\xi(0)$ computed using Greywall's 1986 thermodynamic parameters (Ref. 2.3).

Table 1.1 The Ginzburg-Landau Correlation Length Coefficient, $\xi(0)$.

Pressure (bar)	$\xi(0)$ (nm)
0	50.1
3	32.8
6	25.1
9	20.7
12	18.0
15	16.0
18	14.4
21	13.3
24	12.3
27	11.5
30	10.9

To discuss the boundary conditions, AGR consider a semi-infinite volume of ^{3}He, bounded by the xy plane. At T_c, the A matrix is linear in z,

$$A_{pi} = \text{const}(b_i + z). \tag{1.18}$$

If quasiparticles scatter specularly from the surface, AGR find that

$$A_{px} = A_{py} = \text{const}; A_{pz} = \text{const} \cdot z. \tag{1.19}$$

That is, the transverse components of the order parameter are unchanged, but the perpendicular component *vanishes* at the wall. This behaviour is illustrated schematically in Figure 1.4 . AGR find for diffusely scattering surfaces a reduction of the tangential components by a factor $\xi_s/\xi(T)$, with the normal component again vanishing. In the vicinity of the transition, then, the order parameter is effectively zero at the wall, while at lower temperatures the transverse components have a finite amplitude at the boundary. The rough surface can be thought of as a plane of elastically scattering impurities, which are pair-breakers in anisotropic superfluids (Anderson's theorem[52] does not hold).

One immediate consequence of these boundary conditions is that the B phase is unstable in any geometry having a dimension comparable to the correlation length.† Qualitatively, the quenching of the longitudinal component in films leads to the planar phase, characterized by

$$A_{planar} = \frac{1}{\sqrt{2}} \begin{pmatrix} 1 & 0 & 0 \\ 0 & 1 & 0 \\ 0 & 0 & 0 \end{pmatrix}. \tag{1.20}$$

In a long, narrow tube only the component along the axis survives and one expects the polar phase,

$$A_{polar} = \begin{pmatrix} 1 & 0 & 0 \\ 0 & 0 & 0 \\ 0 & 0 & 0 \end{pmatrix}. \tag{1.21}$$

These qualitative predictions have been fleshed out by detailed calculations, a number of which I will now mention (this listing is not exhaustive). For the cylindrical pore, Barton and Moore predict the stability of two additional phases in the

† The boundary conditions are different if spin rotations are also allowed in the scattering. Sauls has considered this and found a special circumstance in which the B phase could be stabilized right up to a wall (private comm).

That is, the transverse components of the order parameter are unchanged, but the perpendicular component *vanishes* at the wall. This behaviour is illustrated schematically in Figure 1.4 . AGR find for diffusely scattering surfaces a reduction of the tangential components by a factor $\xi_s/\xi(T)$, with the normal component again vanishing. In the vicinity of the transition, then, the order parameter is effectively zero at the wall, while at lower temperatures the transverse components have a finite amplitude at the boundary. The rough surface can be thought of as a plane of elastically scattering impurities, which are pair-breakers in anisotropic superfluids (Anderson's theorem[52] does not hold).

One immediate consequence of these boundary conditions is that the B phase is unstable in any geometry having a dimension comparable to the correlation length.† Qualitatively, the quenching of the longitudinal component in films leads to the planar phase, characterized by

$$A_{planar} = \frac{1}{\sqrt{2}} \begin{pmatrix} 1 & 0 & 0 \\ 0 & 1 & 0 \\ 0 & 0 & 0 \end{pmatrix}. \tag{1.20}$$

In a long, narrow tube only the component along the axis survives and one expects the polar phase,

$$A_{polar} = \begin{pmatrix} 1 & 0 & 0 \\ 0 & 0 & 0 \\ 0 & 0 & 0 \end{pmatrix}. \tag{1.21}$$

These qualitative predictions have been fleshed out by detailed calculations, a number of which I will now mention (this listing is not exhaustive). For the cylindrical pore, Barton and Moore predict the stability of two additional phases in the

† The boundary conditions are different if spin rotations are also allowed in the scattering. Sauls has considered this and found a special circumstance in which the B phase could be stabilized right up to a wall (private comm).

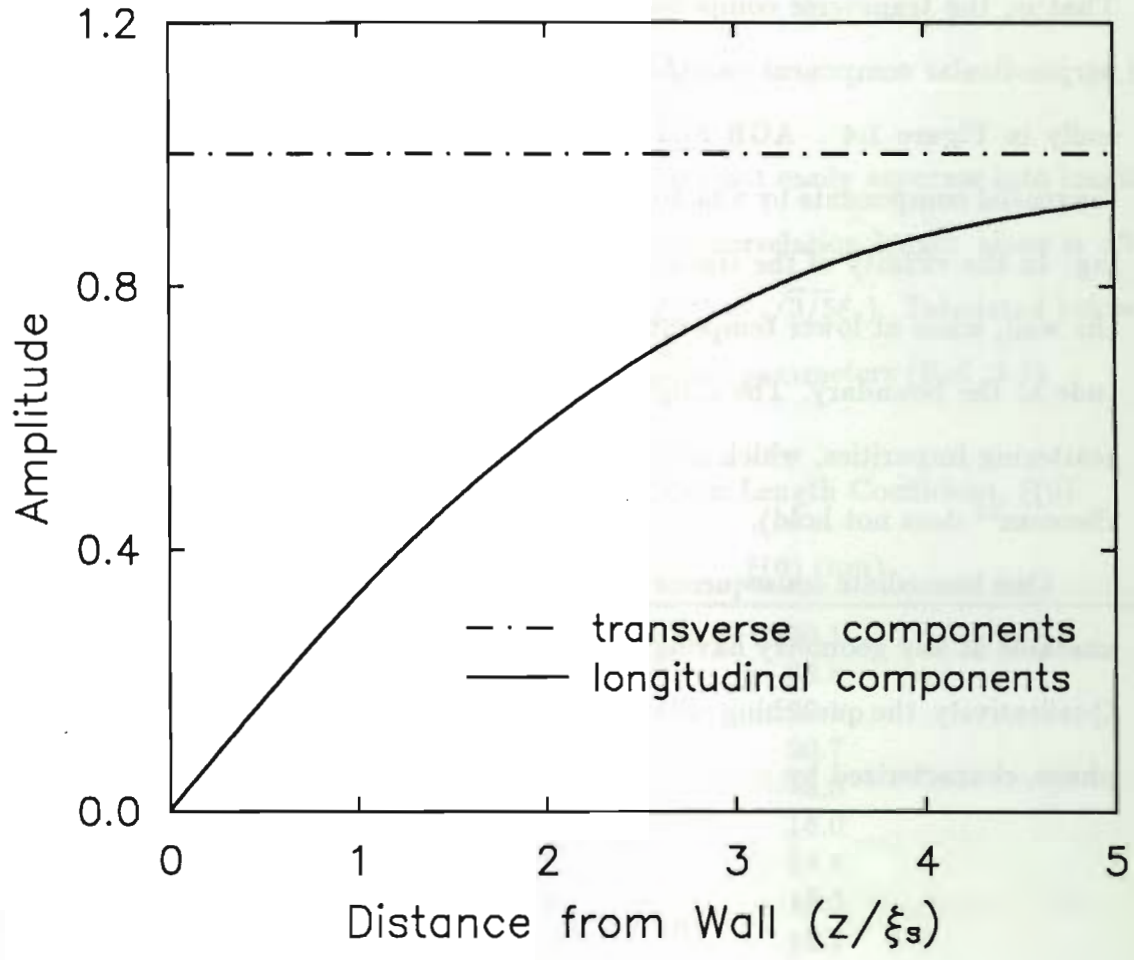

Figure 1.4

Spatial variation of the amplitudes of components of the order parameter near a specular wall, at a temperature not far below T_c.

intermediate size regime between the polar and B phases[23]. Privorotskii observes that walls stabilize the A phase in the vicinity of the polycritical point, in analogy to Wheatley's 'profound' effect of a magnetic field[24]. This analysis has been extended by Kuroda and Nagi[25] and by Fujita *et al.* [26]. The latter authors adopt trial functions for the order parameter and perform a variational calculation to minimize the free energy. Their trial functions for the B phase are planar-like at the walls (the transverse components are in fact slightly *enhanced* near a specular surface). A transition from the A phase to a distorted B phase is predicted at a film thickness of between

7 and 15 correlation lengths, depending upon the strong coupling corrections. (Note that our definition of the correlation length is $\sqrt{2}$ smaller than that of Ref. 26, and $\sqrt{15}$ larger than Ref. 27.) Strong coupling corrections favor the A phase. In the weak coupling limit there is no transition, just a continuous distortion of the B phase into the planar state as a function of decreasing thickness.

The boundary condition at specular surfaces requires a certain form of the order parameter but does not diminish its amplitude. Consequently there is no change of the transition temperature. The diminution of the transverse components at diffusely scattering walls leads to a reduction of the transition temperature in confined geometries, in analogy to the ferromagnetic film with $q > 0$. A numerical calculation of this, based on the AGR theory, has been performed by Kjäldman, Kurkijärvi and Rainer[27] for the cylindrical and thin film geometries. In the limit of small suppressions (sizes greater than, say, eight zero-temperature correlation lengths, so that the transition is close to the bulk T_c), they recover the Ginzburg-Landau results. For the films, that is

$$\frac{T_c^{film}}{T_c} = \exp(\frac{\pi^2 \xi^2(0)}{d^2}). \tag{1.22}$$

This underestimates the transition temperature by about 25% at $d = 3\xi(0)$. The complete solution reveals a critical size, $d_c = 2.0\xi(0)$, below which no superfluidity occurs (to convert the notation of KKR, $\xi_0 = \xi(0)\sqrt{20/7\zeta(3)}$). Note that the GL result can be approximated by $(1 - \frac{\pi^2 \xi^2(0)}{d^2})$.

More recently, variational calculations by Fetter and Ullah[28] and by Li and Ho[29] have further explored the phase diagram and responses of the order parameter (the superfluid density, critical current, and NMR behaviour).

Thuneberg[30], in analogy to his studies of vortex core structures[31], has examined surface states of ^{3}He-B using Ginzburg-Landau theory and the specular boundary condition. He finds a surface A phase which seems to be a strong coupling effect,

in addition to the planar phase. Zhang *et al.*[32] have extended this work beyond the Ginzburg-Landau regime with the quasiclassical theory of ^{3}He and a model for surface roughness. They do not include strong-coupling effects, but this is an important direction for the theory as it provides predictions for the full temperature range. Similar work with a different description of diffuse scattering has been done by Buchholtz[33].

A quasiclassical calculation of the B-planar transition in a film with specular surfaces by Hara and Nagai[34] suggests that extrapolations of the Ginzburg-Landau results are quite reliable provided one uses the correct temperature dependence of the energy gap. Such extrapolations are unlikely to work as well for rough surfaces, however, because of the temperature dependence of the boundary condition on the transverse components of the order parameter.

We summarize many of the interesting features anticipated by the theory in the phase diagram of Figure 1.5 . The dots indicate the normal-superfluid and A-B transition lines for the bulk liquid. In a 250 nm film with diffuse surfaces, these become the solid lines. The transition temperature is reduced, but the domain of the A phase is vastly increased. The order parameter is of course distorted from the bulk A and B forms in this case. When the walls are made specular, the transition temperature recovers and the A phase encroaches a little more on the B. Diffuse surfaces help to stabilize the B phase. This is because one component of the B phase order parameter must be suppressed at the wall in any case, and the diffuse boundary condition already requires this.

1.3 Superfluid ^{3}He in Confined Geometries: Experiment

The word 'confined' applies in one sense or another to every superfluid ^{3}He experiment, as wall effects typically propagate macroscopic distances into the fluid. To re-iterate, our interest here is on size effects in which spatial variation of the *amplitude* of the order parameter is important. This, too, applies in every experiment

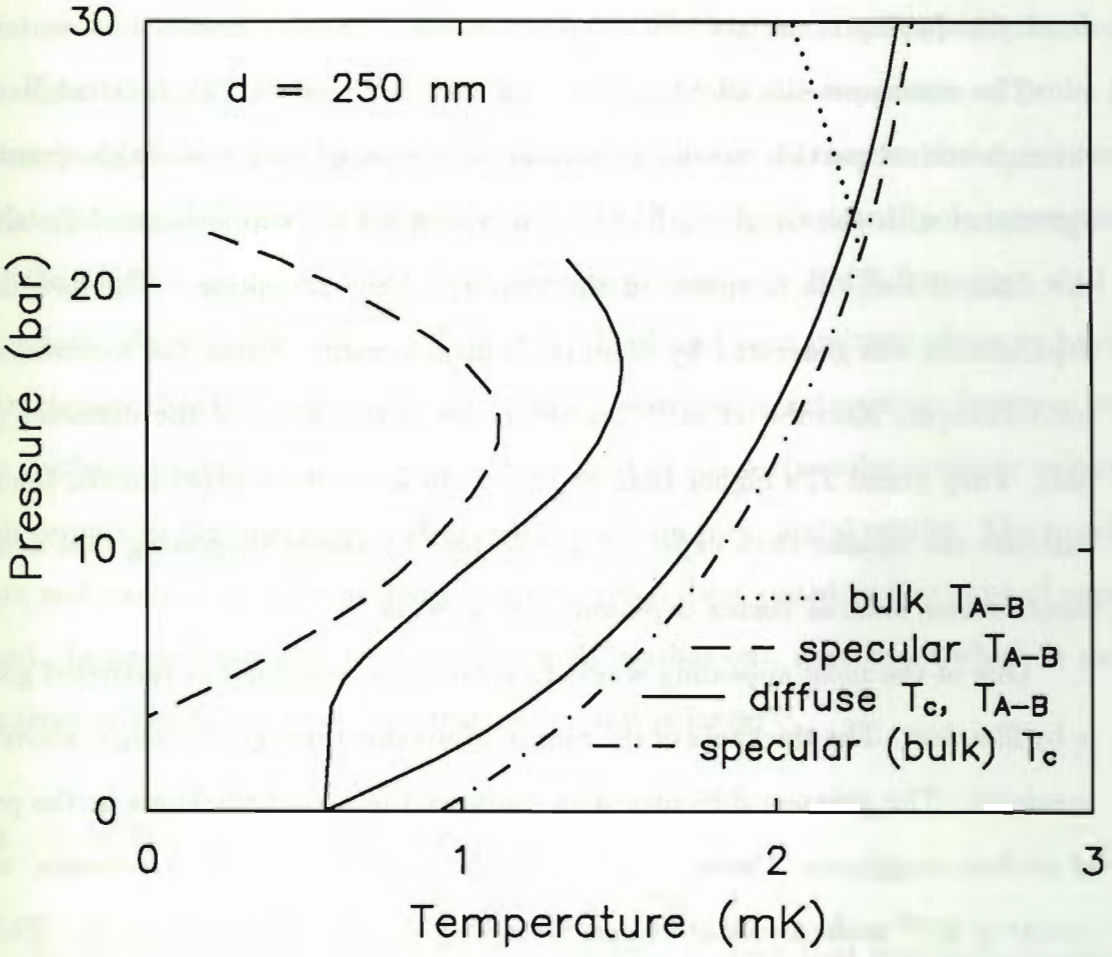

Figure 1.5

A schematic phase diagram for the thin film geometry, showing the anticipated effects of both specular and diffuse surfaces. The thin-film A-B phase boundaries are after Ref. 29. A region of two-dimensional superfluidity (characterized by $\xi(T) > d$)is possible close to the bulk transition line, and is discussed more in Sec. 1.4.

sufficiently close to T_c, but typical temperature control and sensitivity levels require some dimension to be micrometer-sized or smaller. The focus of many early experiments in micron-scale geometries was on control of the 'texture', or *orientation* of the order parameter. More recently, Ginzburg-Landau behaviour at diffusely scattering walls has been indicated by measurements of the transition temperature and critical

current in narrow channels[35–37] and in saturated films[38–40], and by the superfluid density in porous materials[41,42].

The measurements of Manninen and Pekola[35] and of Pekola *et al.*[37] of flow through etched particle tracks in polycarbonate paper find reasonable quantitative agreement with the Ginzburg-Landau prediction for the suppression of T_c, although the data of Ref. 35 is sparse in the vicinity of the transition. The flow in these experiments was generated by diaphragm displacement. Using the torsional oscillator technique, Kotsubo *et al.*[36] probed pores of roughly half the diameter ($\sim$ 350 nm). They found T_c's higher than expected. In all of these experiments, the critical currents are smaller than expected due to pair breaking, suggesting that additional mechanisms, such as vortex depinning, are at work.

One of the most appealing ways of probing the superfluid in restricted geometry is by film flow. The thickness of the film is adjustable through the height above a bulk meniscus. The greatest difficulty is in knowing the actual thickness in the presence of surface roughness. Davis *et al.*[39] decline to make an absolute estimate, whereas Daunt *et al.*[38] make a valiant attempt based on Atkins' oscillations of ^{4}He. The latter authors measure T_c's consistent with Ref. 36. Very recently, however, they have found that *smoother* surfaces than those employed in Ref. 38 produce *greater* suppressions[40]. This suggests that the earlier films were thicker than previously believed.

There are always uncertainties surrounding geometric characterization in these experiments. In fourth sound[41] and torsional oscillator[42] measurements of the superfluid density in packed powders, no reduction of T_c is observed on account of the distribution in pore sizes. A pore size distribution may be incorporated into the analysis of the data[41], but this introduces many unwanted degrees of freedom. It is also difficult to assess effects of the interconnectedness of the pores and of the proximity effect, particularly in the transition region. The data of Ref. 41 seems to be consistent with an extrapolation of Ginzburg-Landau behaviour to low temperatures, however.

The properties which we have been discussing – superfluid density, critical temperature and critical current – are more dependent on the amplitude of the order parameter than on its structure. NMR is the most valuable experimental probe for determining the superfluid phase. In Section 1.2 we neglected the two elements crucial in determining the NMR response of superfluid ^{3}He – the nuclear dipole interaction, and the applied magnetic field. The surprising transverse NMR frequency shift of superfluid ^{3}He was elucidated by Leggett[43]. He found each unitary phase to have a characteristic NMR 'fingerprint'. The NMR behaviour is anisotropic, however, and in a confined geometry it is important that most of the surfaces be similarly oriented with respect to the magnetic field in order to obtain meaningful results. The parallel plate and straight cylinder geometries are therefore best suited to this type of experiment. In packed powders the signal actually washes out, a problem which is more apparent at low fields, where the transverse shift is larger[44].

1.4 Two Dimensional Superfluidity

The prevailing notion in the ^{3}He community has been that real surfaces scatter ^{3}He quasiparticles diffusively. We have seen in section 1.2 that this precludes superfluidity in films thinner than about $2\xi(0)$ at any temperature. Close to the bulk transition temperature the critical thickness is $\pi\xi(T)$. (These thicknesses are halved if only one side of the film is in contact with a solid and the free surface is specular.) With specular surfaces, however, the regime of two-dimensional superfluidity (with $D < \xi(T)$) becomes accessible experimentally. The cw-NMR response in the 2D regime has been treated theoretically by Tešanović and Valls[45]. Qualitatively different behaviour is predicted. In particular, the *sign* of the frequency shift at small tipping angles is opposite to what is found for the A phase. Stein and Cross[46] have considered phase transitions in two dimensional films of the A phase. They note possibilities for a Kosterlitz-Thouless transition among vortices in the phase of the order parameter,

and for an Ising-like transition among "islands of reversed $\vec{l}$". Brusov and Popov[47] have examined a model of superfluid films with a view to the stable phases and their excitation spectra.

A host of other phenomena are predicted for progressively smaller sizes. At thicknesses which can be counted up in not so many Fermi wavelengths, the Fermi sphere is no longer a quasi-continuum along one axis and we have the predictions of Tešanović and Valls for quantum size effects[48] and of Volovik for quantized Hall[49]. When the film thickness is only a monolayer or two, the dimensionality of the *normal* phase is also reduced. Kurihara[50] has predicted a mechanism (based upon third sound) for singlet superfluidity of 2D ^{3}He on ^{4}He films. Superfluid transitions among ^{3}He *dimers* in He II (either on the surface, or dissolved in thin layers, or bound in vortex cores) have been considered by Bashkin[51].

1.5 Summary of the Following Chapters

The focus of the remainder of this thesis is on our experimental results for ^{3}He films. Instead of using saturated films (with a free surface), however, we confine the liquid between two solid walls. This enables us to elevate the pressure, in order to scan the phase diagram for the A-B transition line and to study the behaviour near the normal-superfluid transition for a range of correlation lengths.

The data which we present in the first half of Chapter 2 displays reasonable quantitative agreement with the Ginzburg-Landau theory. To our knowledge, this is the first time that such agreement has been found for measurements *in the vicinity of the transition*, which is the only region in which the theory may be applied with confidence. An interesting side-issue which arises out of the NMR work in these sections is the averaging of the solid and liquid ^{3}He NMR signals due to exchange at the surface.

A natural step in the process of understanding the NMR behaviour was to supplant the 'localized' ^{3}He layer with ^{4}He. This act had unexpected consequences, which deflected much of our subsequent attention to the question of the microscopic nature of the boundary condition. Our Mylar substrate has probably the smoothest geometrical surface available short of going to the extremes of preparation required in surface physics. Nevertheless, the scattering of ^{3}He quasiparticles from this surface depends sensitively on whether it is covered by adsorbed monolayers of ^{3}He or of ^{4}He. A continuous tunability with ^{4}He coverage of the boundary condition on the superfluid order parameter is indicated by the results of the last section of Chapter 2.

In Chapter 3, we pursue the boundary condition question into the normal phase. The quasiparticle-surface scattering determines the amount of slip in the hydrodynamic response of the fluid. Our initial results reveal two interesting new aspects of the system. Firstly, we find that the apparent 'specularity' for ^{3}He scattering increases at the transition to superfluidity in the ^{4}He film. Secondly (moving somewhat farther afield), we find that the transition in the ^{4}He film persists to pressures substantially above the bulk solidification point of ^{4}He. As many surface probes cannot distinguish between liquid and disordered solid states, a superfluid transition is a welcome signature.

References for Chapter 1

1.1 M. Knudsen, *Kinetic Theory of Gases*, Methuen, London (1950).

1.2 J.J. Thomson, Proc. Camb. Phil. Soc. **11**, 120 (1901).

1.3 K. Fuchs, *ibid.* **34**, 100 (1938).

1.4 E.H. Sondheimer, Adv. Phys. **1**, 1 (1952).

1.5 P. Wißmann, in Springer Tracts, vol. 77 (1975).

1.6 T. Klitsner and R.O. Pohl, Phys. Rev. **B34**, 6045 (1986).

1.7 L.D. Landau, ZETP **7**, 19 (1937). English translation in *Collected Papers of L.D. Landau*, D. ter Haar, ed., Gordon and Breach, London (1965), p. 193.

1.8 V.L. Ginzburg and L.D. Landau, ZETP **20**, 1064 (1950). English translation in *Collected Papers*, p. 546.

1.9 M.I. Kaganov and A.N. Omel'yanchuk, Sov. Phys. JETP **34**, 895 (1972). I am indebted to Kenny Blum for bringing this article to my attention.

1.10 V.L. Ginzburg and L.P. Pitaevskii, *ibid.* **7**, 858 (1958).

1.11 T.C. Padmore and J.D. Reppy, Phys. Rev. Lett. **33**, 1410 (1974).

1.12 L.V. Kiknadze and Yu. G. Mamaladze, Sov. J. Low Temp. Phys. **1**, 106 (1975).

1.13 L.P. Gor'kov, Sov. Phys. JETP **9**, 1364 (1959).

1.14 L. Valenta, Czech. J. Phys. **7**, 133 (1957).

1.15 D. Saint-James and P.G. de Gennes, Phys. Lett. **7**, 306 (1963).

1.16 H.K. Wong, B.Y. Jin, H.Q. Yang, J.B. Ketterson and J.E. Hilliard, J. Low Temp. Phys. **63**, 307 (1986).

1.17 N.D. Mermin and G. Stare, Phys. Rev. Lett. **30**, 1135 (1973).

1.18 P.W. Anderson and W.F. Brinkman, Phys. Rev. Lett. **30**, 1108 (1973).

1.19 G. Stare, Ph.D. Thesis, Cornell University (1974).

1.20 V. Ambegaokar and N.D. Mermin, in *Proc. 24th Nobel Symposium*, Academic, New York (1974), p. 97.

1.21 V. Ambegaokar, P.G. de Gennes and D. Rainer, Phys. Rev. **A9**, 2676 (1974).

1.22 L.J. Buchholtz and A.L. Fetter, Phys. Rev. **B15**, 5225 (1977).

1.23 G. Barton and M.A. Moore, J. Low Temp. Phys. **21**, 489 (1975).

1.24 I.A. Privorotskii, Phys. Rev **B12**, 4825 (1975).

1.25 Y. Kuroda and A.D.S. Nagi, Physica **85B**, 131 (1977).

1.26 T. Fujita, M. Nakahara, T. Ohmi and T. Tsuneto, Prog. Theor. Phys. **64**, 396 (1980).

1.27 L.H. Kjäldman, J. Kurkijärvi and D. Rainer, J. Low Temp. Phys. **33**, 577 (1978).

1.28 A.L. Fetter and S. Ullah, *ibid.* **70**, 515 (1988).

1.29 Y.-H. Li and T.-L. Ho, preprint.

1.30 E.V. Thuneberg, Phys. Rev. **B33**, 5124 (1986).

1.31 E.V. Thuneberg, *ibid.* **B36**, 3583 (1987).

1.32 W. Zhang, J. Kurkijärvi and E.V. Thuneberg, *ibid.* **B36**, 1987 (1987).

1.33 L.J. Buchholtz, *ibid.* **B33**, 1579 (1986).

1.34 J. Hara and K. Nagai, submitted to J. Low Temp. Phys.

1.35 M.T. Manninen and J.P. Pekola, Phys. Rev. Lett. **48**, 812 (1982).

1.36 V. Kotsubo, K.D. Hahn and J.M. Parpia, Phys. Rev. Lett. **58**, 804 (1987).

1.37 J.P. Pekola, J.C. Davis and R.E. Packard, Jap. J. Appl. Phys. **26-3**, 113 (1987).

1.38 J.G. Daunt *et al.*, J. Low Temp. Phys. **70**, 547 (1988).

1.39 J.C. Davis, A. Amar, J.P. Pekola and R.E. Packard, Phys. Rev. Lett. **60**, 302 (1988).

1.40 J. Harrison, private communication.

1.41 K. Ichikawa *et al.*, Phys. Rev. Lett. **58**, 1949 (1987).

1.42 V. Kotsubo *et al.*, Jap. J. Appl. Phys. **26-3**, 143 (1987).

1.43 A.J. Leggett, Ann. Phys (NY) **85**, 11 (1974).

1.44 A.I. Ahonen, M.T. Haikala and M. Krusius, Phys. Lett. **47A**, 215 (1974).

1.45 Z. Tešanović and O.T. Valls, Phys. Rev. **B31**, 1374 (1985).

1.46 D.L. Stein and M.C. Cross, Phys. Rev. Lett **42**, 504 (1979).

1.47 P.N. Brusov and V.N. Popov, Sov. Phys. JETP **53**, 804 (1981).

1.48 Z. Tešanović and O.T. Valls, Phys. Rev. **B33**, 3139 (1986).

1.49 G.E. Volovik, preprint (submitted to Phys. Lett. A).

1.50 S. Kurihara, J. Phys. Soc. Jap. **52**, 1311 (1983).

1.51 E.P. Bashkin, Sov. Phys. JETP **51**, 181 (1980).

1.52 P.W. Anderson, J. Phys. Chem. Solids **11**, 26 (1959).

1.53 U. Gradmann, in *Magnetic Properties of Low Dimensional Systems*, L. M. Falicov and J.L. Móran-López, ed.s, Springer-Verlag, Berlin (1986).

Chapter 2

Simultaneous NMR and Superfluid Density Measurements for a Superfluid ^{3}He Film System

At this stage one might say generally that a plane parallel geometry is preferred as a means to define carefully and simply the conditions of measurement.

J.C. Wheatley

2.1 Introduction

In this Chapter we present the results of our investigations of superfluid ^{3}He in a narrow parallel plate, or thin film, geometry. We have examined both pure ^{3}He samples and dilute mixtures of ^{4}He in ^{3}He. We obtain very good agreement of our pure ^{3}He results with the Ginzburg Landau theory. This theory is straightforward and well-accepted, but experiments to verify it in quantitative detail are in fact rather difficult to perform. The present results represent the most convincing demonstration of Ginzburg-Landau behaviour to date. Some uncertainties remain, not the least of which derive from the *bulk* measurements. We have greatly reduced the uncertainty in geometry which has affected earlier superfluid density measurements. We have also used NMR to probe the order parameter structure, in order to answer questions about the phase diagram. The principal result of the dilute mixture studies is an unexpected and exciting control over the boundary condition using surface ^{4}He. Two preliminary reports of the work have been published[1].

2.2 Experimental Details

These experiments are performed on a copper nuclear demagnetization cryostat, as described in detail in Appendix A. The static field for nuclear magnetic resonance is provided by a large bore persistent-mode superconducting solenoid[2] residing in the helium bath. The field homogeneity achieved with this arrangement is modest, about $1{:}10^4$ for a 1 cm diameter spherical volume, limited by stray and remanent fields of the demagnetization solenoid. This enables us to measure fractional frequency shifts of 10^{-6} when the lineshape remains constant. The cell and thermometers are thermally linked at the nuclear stage by a half-inch thick plate. This plate is of silver for its small Schottky heat capacity in the field of the NMR solenoid. This field bathes the platinum NMR thermometer, which conveniently resonates at 280 kHz when the ^{3}He signal is at 1 MHz, and can function as a field marker as its resonant frequency is essentially temperature independent. Smaller coils inside the cryostat are used to vary independently the Pt and ^{3}He static fields as required. The large volume of the NMR solenoid necessitates a reentrant design for the tin heat switch, placing it above the mixing chamber. The performance of the apparatus is not affected noticeably by the NMR field. We are able to cool below 300 μK and the residual heat leak is less than 1 nW.

Our thermometry is based upon the ^{3}He melting curve. We use the most recent temperature scale of Greywall[3]. Since the Greywall scale and the older temperature scale of Halperin[4] are not simply proportional at low temperatures, the Pt thermometer provides us with some means of selecting between the two. The Pt should have a strictly Curie susceptibility in this range, but when calibrated against the Halperin melting curve it appears Curie-Weiss like, with a divergence at 250 μK. This anomaly does not arise with the new Greywall scale (see Appendix B).

We are able to measure a small thermal disequilibrium between the sample helium and the thermometers. The bulk ^{3}He superfluid transition is marked by a sharp

increase in the dissipation of the torsion pendulum (see Chapter 3). As an example, when the liquid pressure is 8 bar and the oscillator is running at a typical amplitude (chosen such that self-heating is negligible), the bulk transition in the cell occurs with the melting curve thermometer about 10 μK below the expected temperature on the Greywall scale. This temperature offset increases to only 40 μK when the 'anomalous' Kapitza conductance channel (magnetic) is cut off by ^{4}He multilayers coating the sintered silver heat exchanger. In analyzing our data we always scale the temperature to the bulk transition as determined by the oscillator. [A point of notation: I use T_c exclusively to indicate bulk transition temperatures, and refer to transitions in the restricted geometry by T_c^{film}.]

The design of our cell capitalizes on a symbiosis of nuclear magnetic resonance and torsional oscillator methods in this application. † We do pulse NMR in a crossed-coil configuration, in order to thermally anchor the transmitter coil to the mixing chamber. Since there is no physical contact between the transmitter coil form and the ^{3}He capsule, it easily doubles as the electrode structure for an electrostatically driven torsional oscillator[5]. This structure cannot be made of metal, as is normally done, because of rf screening and eddy current heating problems. We find that an all epoxy construction, assembled with nylon screws and grease to ensure rigidity, performs adequately, with no anomalous shifts of oscillator period or dissipation. Stycast 1269A epoxy[6] is used throughout. The 1269A epoxy has less than 25% of the dielectric loss of Stycast 1266 at 1 MHz, and in addition is somewhat stronger.

† The word 'symbiosis' reflects a certain philosophical bent. Part of the satisfaction that I derive from experimentation comes from regarding the work as an art. The apparatus is an interactive sculpture which the user may coax into revealing some small truth about Nature.

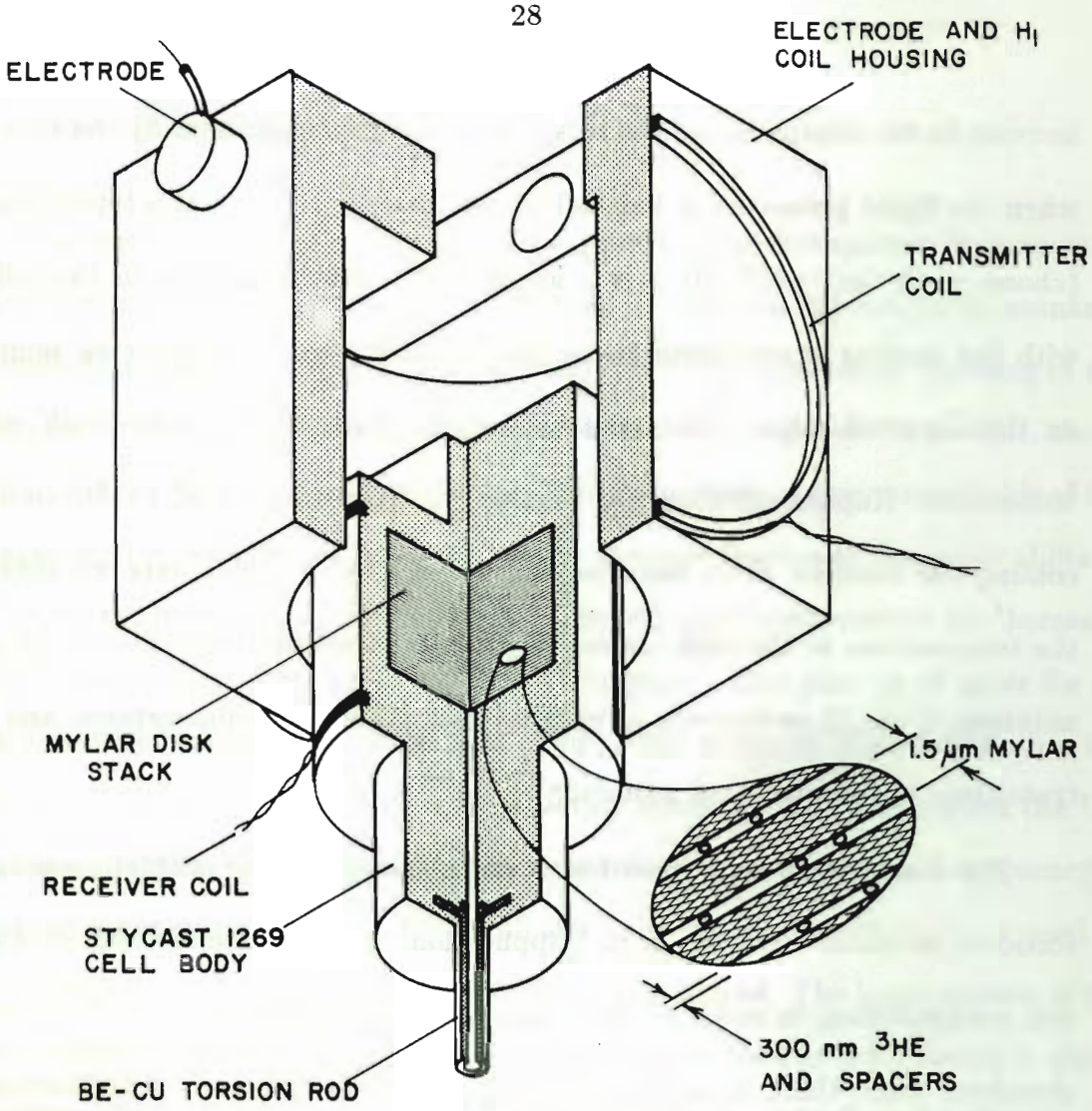

Figure 2.1

The combined torsion pendulum/NMR probe. The ^{3}He in the head of the oscillator fills and cools through the hole in the torsion rod, which terminates in a small heat exchanger linked to the nuclear refrigerant. The electrode structure is thermally sunk to the mixing chamber. Drawing by Eric Smith.

A cut-away view of the pendulum bob, or head, of the cell is shown in Figure 1. Three # 40 copper wires (two in a twisted pair for the NMR coil, and a third for connection to the common plate of the drive and detection capacitors) make contact to the head of the oscillator, without seriously impairing its performance. The torsional resonance of the pendulum is at 1750 Hz, well above the frequency of most of the (potentially parasitic) resonances of the rest of the cryostat. The torsion rod is 1.4

mm diameter beryllium-copper with a 0.9 mm diameter hole for thermal conduction through the ^{3}He.

The heart of the cell is the stack of mylar sheets which creates the helium films by confinement. To optimize the helium fill fraction we use Mylar 6C, which at 1.5 μm is the thinnest currently available[7]. The mylar surfaces are sparsely populated with 0.5 μm diameter polystyrene microspheres[8] to establish the spacing. An electron micrograph of mylar so decorated is shown in Figure 2.2 .

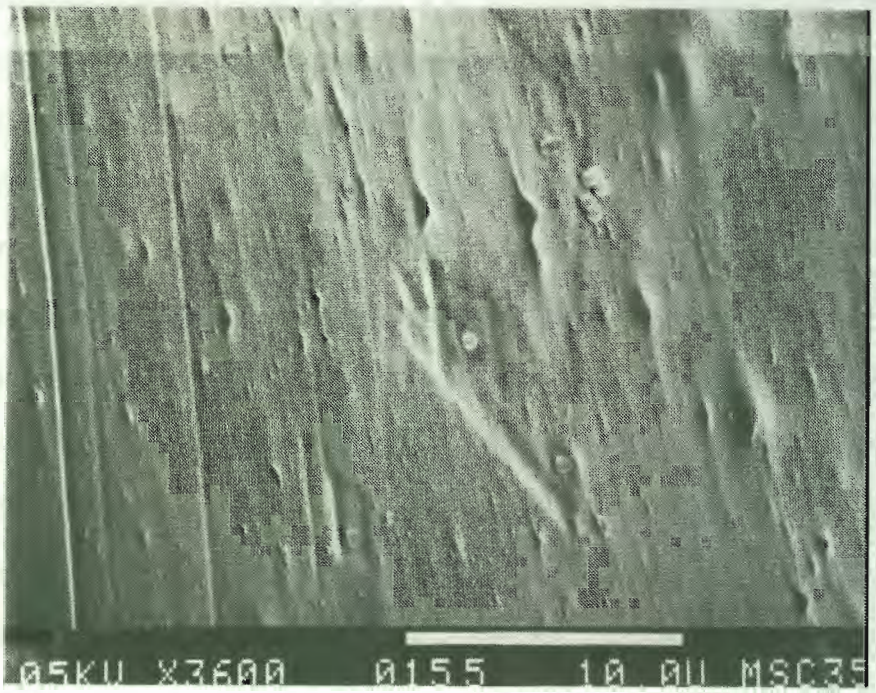

Figure 2.2

An electron micrograph of the surface of Mylar 6C sprinkled with 0.5 μm polystyrene microspheres. The beads are manufactured for electron microscope calibration. The surface detail is emphasized by tilting the sample and by reducing the beam energy to 5 keV. Carbon deposits from scans at higher magnification are also visible. The micrograph was made by John Hunt.

The beads are deposited on the surface by misting a suspension of spheres in isopropanol onto the mylar and allowing the alcohol to evaporate. Methanol does not

seem to wet the surface, and upon drying leaves patterns of beads reminiscent of stone circles. The misting operation is done in a dust-free area, and the mylar surface is itself sufficiently flat and clean that the polystyrene particles determine the spacing. In a similar cell for studies of ^{4}He superfluid films, Adams and Glaberson[9] stacked up mylar sheets directly and found an open volume corresponding to an average sheet separation of 120 nm. The choice of surface density for these particles is based on a trade-off between i.) maintaining a uniform sheet spacing, and ii.) preserving the superfluid order parameter structure of a geometry with closely spaced walls and no intervening beads. A razor-sharp hardened steel punch is used to cut discs from larger sheets, and a 0.5 mm hole is punched in the center of each disc to ensure thermal equilibrium within the cell. The final stack of discs is packed tightly into an epoxy capsule. All of the sheets must be firmly entrained to obtain stable operation of the torsional oscillator. The interior of the epoxy capsule is thinly coated with silicon grease in an attempt (not entirely successful) to fill any voids which may occur at the edge of the stack, and to help anchor the individual sheets. The mean sheet spacing, which we deduce from the shift in oscillator period upon filling with liquid helium, is 280 ± 20 nm. The uncertainty arises in our determination of the moment of inertia of the empty oscillator. Presumably the spheres compress and indent the mylar during the packing step. This primitive fabrication method works surprisingly well, as the results on the following pages will testify. It requires the mylar surfaces to be flat and clean. Under the electron microscope, the main surface features are 100 nm-scale pimples, and occasional larger specks of dirt.

The data are acquired under computer control. The magnets are left in persistent mode following a demagnetization and the temperature is stepped using pulses of heat, between each of which is allowed time for equilibration. The NMR frequencies are determined by Fourier transformation of digitized free induction decays. No corrections for decay of the magnet currents are required on the time scale of these

experiments. Some heating of the cell occurs as a result of each NMR pulse. The return to equilibrium is monitored by the response of the torsional oscillator, which is very sensitive to the ^{3}He temperature below the superfluid transition. A typical thermal time constant is 5 minutes, limited by conduction through the fill column. We estimate the time constants for equilibration within the head of the oscillator to be much shorter.

2.3 Experiments on Pure ^{3}He

In this section we discuss our data for pure ^{3}He. Both the NMR and torsional oscillator results in this case are very well described by the Ginzburg-Landau theory, assuming diffusive boundaries. We explain in some detail the corrections which must be applied to the NMR data in order to separate the liquid behaviour from effects of the surface monolayer of ^{3}He. This surface 'solid' can be displaced by ^{4}He in order to make the NMR experiment more straightforward, which as it turns out also causes unexpected changes in the boundary condition for ^{3}He quasiparticle scattering. The results of our measurements for dilute mixtures of ^{4}He in ^{3}He are presented in the next section.

2.3.1 Pure ^{3}He NMR

As NMR is our probe of the order parameter structure, we preface this subsection with comments about the phase diagram. Our measurements span temperatures down to $T_c/4$ at pressures between 1.5 bar and 22 bar, with additional observations close to the transition temperature, T_c, at 0 bar and 29 bar. In 280 nm films we see monotonic, continuous change below the normal fluid–A phase transition. It is interesting to learn that the A phase is stabilized by the walls over the entire phase space, even at low pressures, where the planar phase would occur if strong-coupling effects were

negligible. Despite the fact that the correlation length changes by a factor of five when we vary the pressure, we do not observe a 'B' transition (a transition to a distorted version of the bulk B phase). This is, in part, because the dimensionless thickness at which this transition takes place increases with the pressure[10]. However, our films are thicker than the critical thicknesses for formation of a B state at $T = 0$ calculated by Li and Ho for pressures above about 3 bar, and by Hara and Nagai above 12 bar (see the references to Chapter 1). The transition is first order, so perhaps in the experiments we supercool over it.

A lowering in temperature of the A–B phase boundary at high pressures has been observed in 4 μm thick films by Ahonen *et al.*[11] (AKP). That experiment is similar in spirit to ours. It is a study of the superfluid confined on the scale of the dipole bending length, whereas our focus is on the correlation length (typically two orders of magnitude shorter). Two features of the AKP experiment are of particular interest here: i.) the NMR response of the dipole-unlocked A phase, and ii.) the Curie-Weiss paramagnetism of the surface layer of ^{3}He. The NMR response is discussed later, in relation to Figure 2.7 . The excess magnetization arises because surface atoms, bound by van der Waals attraction to the substrate, do not participate in the Fermi degeneracy of the liquid. This 'localized' or 'solid' layer has by now been studied extensively[12], but was first demonstrated to exist by Ahonen *et al.*[13], who found that the addition of a small quantity of ^{4}He was sufficient to make the Curie-Weiss component disappear.

The helium magnetization measured by pulse NMR is shown in Figure 2.3 for the liquid pressure of 9 bar. Extensive use of this data is made later, during analysis of the frequency shifts. To illustrate the Curie-Weiss nature of the surface layer, the data are plotted as the inverse of the magnetization with the high temperature, or Fermi liquid, component subtracted off. The linear extrapolation of the high temperature data intersects the abscissa at the Weiss temperature, $\Theta = 0.5$ mK. This value is

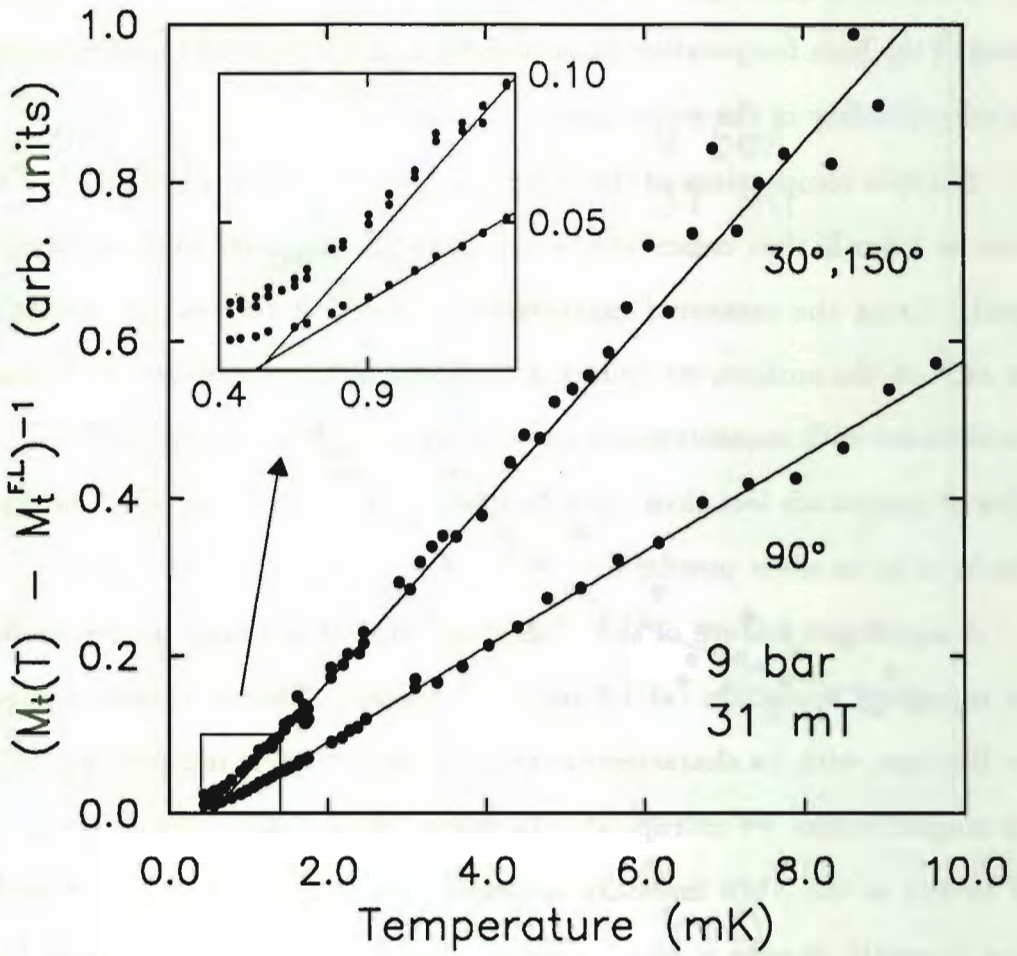

Figure 2.3

The inverse localized layer transverse magnetization following a tipping pulse. The localized layer magnetization is the temperature-dependent excess above the Fermi liquid component, $M_t^{F.L.}$. The solid lines are linear fits which reflect the Curie-Weiss nature of the surface layer susceptibility.

consistent with earlier measurements[13,14]. The Curie-Weiss function, $\chi = C/(T - \Theta)$ is a high temperature approximation for systems with a ferromagnetic tendency ($\Theta > 0$). The measurements deviate from this form at low enough temperatures, as emphasized by the inset of the Figure, where the polarization becomes too large for this approximation to hold. We have not endeavored to fit our data using, for example, additional terms from the expansion of the Brillouin function. Godfrin *et*

al.[15] have recently analyzed the susceptibility of ^{3}He multilayers on Grafoil using 10 terms of the high temperature expansion for a 2D Heisenberg ferromagnet to describe the susceptibility of the second layer.

The spin temperature of the ^{3}He Fermi liquid at 9 bar is 256 mK[16]. Each surface atom at 1.5 mK thus contributes as much to the magnetization as 256 atoms in the liquid. Using the measured magnetization, and 8×10^{14} as the number of atoms per cm^2 on the surface, we deduce a thickness of 1.1 monolayers for the solid. This is consistent with measurements for a number of other substrates[14,17,18], but is one order of magnitude less than the 5 to 10 monolayers found by AKP on mylar and by Okuda *et al.* on silver powder[19].

A significant feature of the magnetization data is that it shows no signature of the superfluid transition (at 1.8 mK in this case). This establishes right away that the B phase, with its characteristic susceptibility drop, is not present. To determine the magnetization we extrapolate the free induction decays back to the end of the RF pulses, as the NMR linewidth increases by a factor of two in the superfluid state. This linewidth change is larger than was found in bulk measurements by Bozler *et al.*[20], suggesting an additional factor due to inhomogeneity in the geometry or in the tipping pulses.

We now begin the discussion of NMR frequency shifts. In Figure 2.3 , we plot the transverse magnetization for different pulses, to demonstrate that the tipping angles are well controlled even in the presence of the substantial frequency shifts (see below) which occur in the superfluid. We minimize the RF heating by using pulses of the smallest spectral width, or longest duration, that irradiate the frequency range of interest with adequate uniformity. It is essential to measure the resonant frequency for different tipping angles in these confined geometries, in order to differentiate among sources of frequency shift which are intrinsic to or external from the helium. We assume that any tipping angle dependence of the shift represents an intrinsic effect,

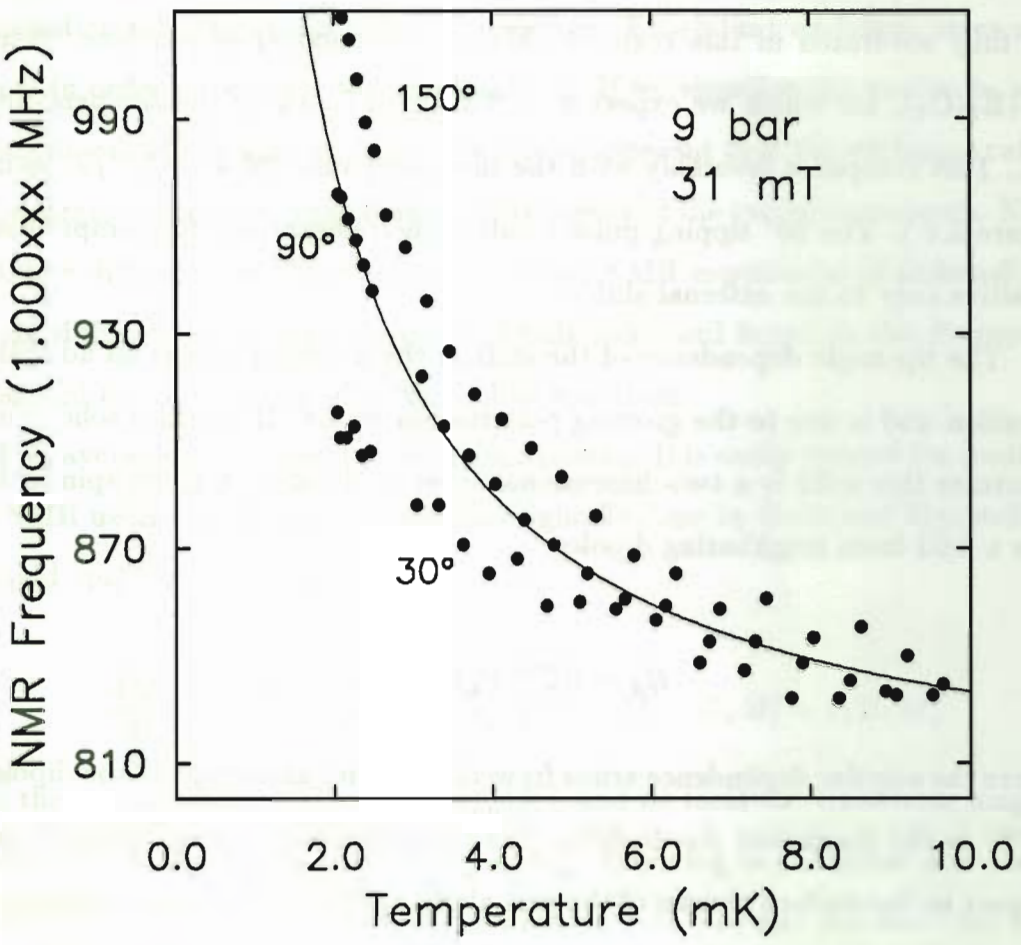

Figure 2.4

The tipping angle dependent NMR frequency in the normal phase. The solid line shows a shift proportional to inverse temperature, which we ascribe to increasing polarization in the mylar. The asymptotic high temperature limit is 1.000793 MHz.

as the measurement is resonant and the helium spins alone are perturbed. Angle-independent effects may or may not be intrinsic. Figure 2.4 shows the temperature dependence of the frequency in the normal phase. The dominant behaviour is pulse independent and proportional to inverse temperature. No effect of this kind is expected for helium, and we attribute it to the protons in the mylar. The mylar stack acts as an effective medium in which the helium is placed. It has a small volume

susceptibility, κ, proportional to the number density of protons (any electronic spins are fully saturated in this regime). Mylar is a polymer of ethylene teraphthalate ($C_{10}H_{10}O_4$), for which we expect $\kappa = 6 \times 10^{-4}/T$, where the temperature T is in mK. This compares favorably with the measured value of $4 \times 10^{-4}/T$ (solid line in Figure 2.4). The 90° tipping pulse result is the relevant one for comparison, as it is sensitive only to the external shifts.

The tip-angle dependence of the shift in the normal phase is an additional complication and is due to the growing polarization of the ^{3}He surface solid. On our flat substrate this solid is a two-dimensional sheet of dipoles. A given spin in this sheet sees a field from neighboring dipoles

$$H_d = H_d^{max} P(1 - 3cos^2\phi)/2, \tag{2.1}$$

where the angular dependence arises from the familiar anisotropy of the dipolar field[21]. H_d^{max} is the maximum dipole field, P is the polarization, and ϕ the tilt angle with respect to the surface normal of the axis along which the dipoles are polarized. In our experiment an external field $H_0 \gg H_d^{max} P$ is applied along the surface normal, and following a ϕ degree RF pulse the spins precess in the resultant $H \approx H_0 + H_d cos\phi$ (on time scales $\ll T_1$, which covers the entire free induction decay in this case). The observed shifts are in reasonable agreement with expectation. From the solid layer density, H_d^{max} is estimated to be 0.3 mT[22], and the solid layer polarization at 2 mK is 1.6 %. Taking into account mixing with the liquid magnetization (see below), the predicted shift at 2 mK is 45 Hz, while the measurement yields 60 ± 10 Hz.

Although the helium polarization is large enough to produce observable frequency shifts only in the solid layer, in practice the entire signal is affected, as may be seen from the lineshapes in Figure 2.5 . What we observe is in fact an average of the spin precession rates on the surface and in the liquid caused by rapid atomic exchange between the surface and the liquid. The spins experience both environments

equally. The effect also relies on spin diffusion in the liquid sufficiently fast for uniform dissemination of information about the surface. Exorbitant exchange rates are not required in order to produce this phenomenon. If we visualize the motion in a frame rotating at one of the Larmor frequencies, it is apparent that the exchange rate need only be large on the scale of the difference frequency of the two environments. Note the qualitative difference with the original A phase NMR experiment of Osheroff, where the spin diffusion times across regions of bulk solid and liquid in the Pomeranchuk cell assured the observation of a double line spectrum.

This averaging is a type of motional narrowing. It is easily treated for continuous-wave NMR using the Bloch equations, as originally done by Hahn and Maxwell[23]. For the liquid spin population we write

$$\frac{dM_t^l}{dt} = (-\frac{1}{T_2} + i\Delta\omega + i\frac{\delta\omega}{2})M_t^l - C_l M_t^l + C_s M_t^s + i\gamma H_1 M_z^l \qquad (2.2)$$

where the magnetization $\vec{M}_l = (M_x^l, M_y^l, M_z^l)$, and we treat the transverse magnetization as the complex quantity $M_t^l = M_x^l + iM_y^l$. Referring to the liquid and solid precession rates as ω_l and ω_s, we use the notation $\delta\omega = \omega_s - \omega_l$ and $\Delta\omega = \omega - (\omega_l + \omega_s)/2$, where ω is the frequency of the H_1 field. T_2 is the transverse relaxation time of the lines (inhomogeneously broadened, in our case). C_l and C_s are transition rates for the exchange between the liquid and solid spin populations. They are related by $C_l = (M_z^s/M_z^l)C_s$, as there is no *net* transfer of magnetization between the two. A similar expression holds for M_t^s. In the steady state, the time derivatives vanish and we solve for the total transverse magnetization,

$$M_t^l + M_t^s = i\gamma H_1 \left(\frac{M_z^l \alpha_s + M_z^s \alpha_l + (M_z^l + M_z^s)(C_l + C_s)}{(\alpha_l + C_l)(\alpha_s + C_s) - C_l C_s} \right), \qquad (2.3)$$

where

$$\alpha_{l,s} = \frac{1}{T_2} - i(\Delta\omega \pm \frac{\delta\omega}{2}).$$

The imaginary component of this gives the NMR absorption.

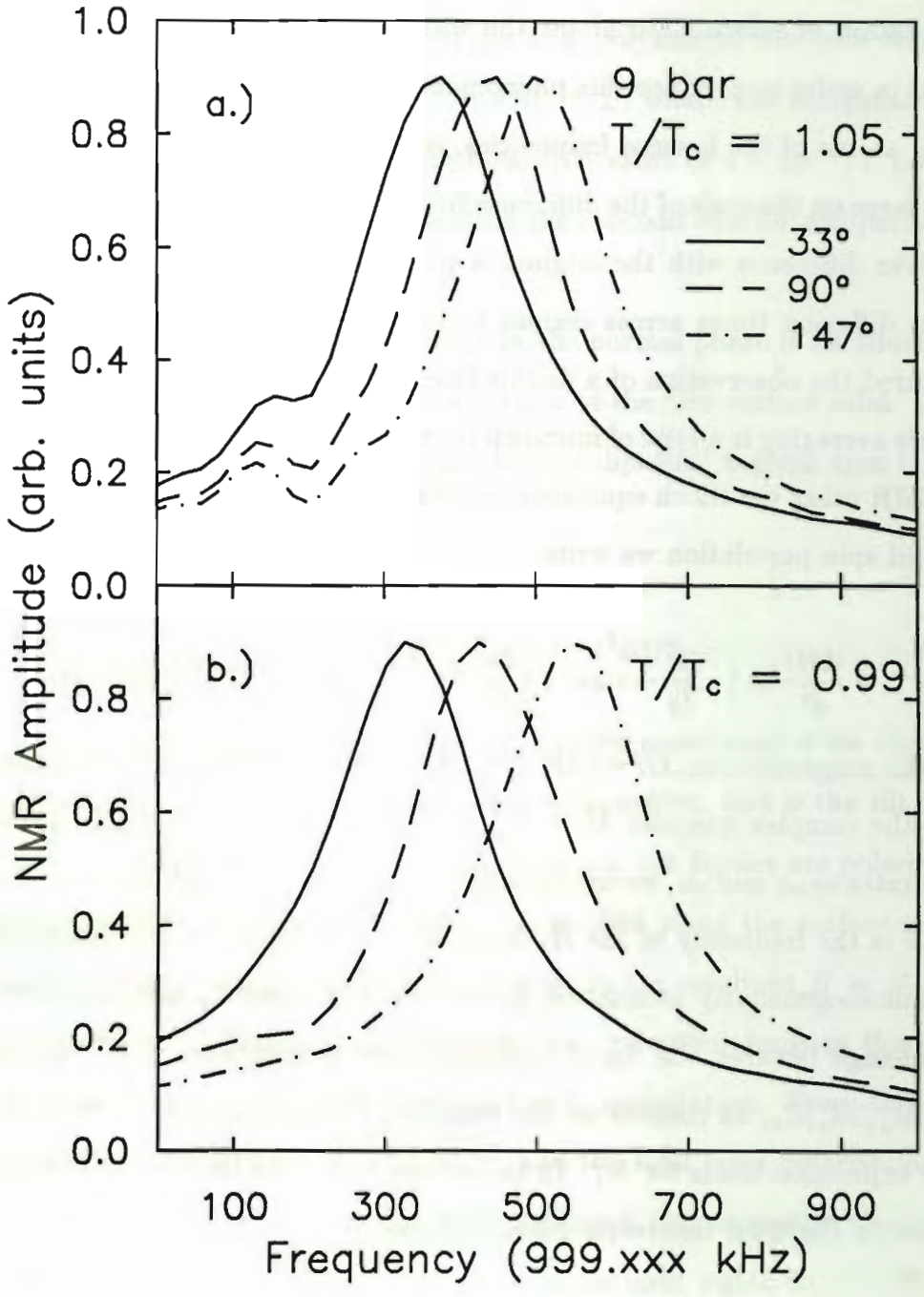

Figure 2.5

^{3}He lineshapes obtained by Fourier transformation. All the heights have been normalized. The liquid magnetization is slightly greater than that of the solid under these conditions. The frequency shift causing the tipping angle dependence occurs in the surface layer, but the *entire resonance* moves due to exchange. See the text for an explanation of the small side lobe.

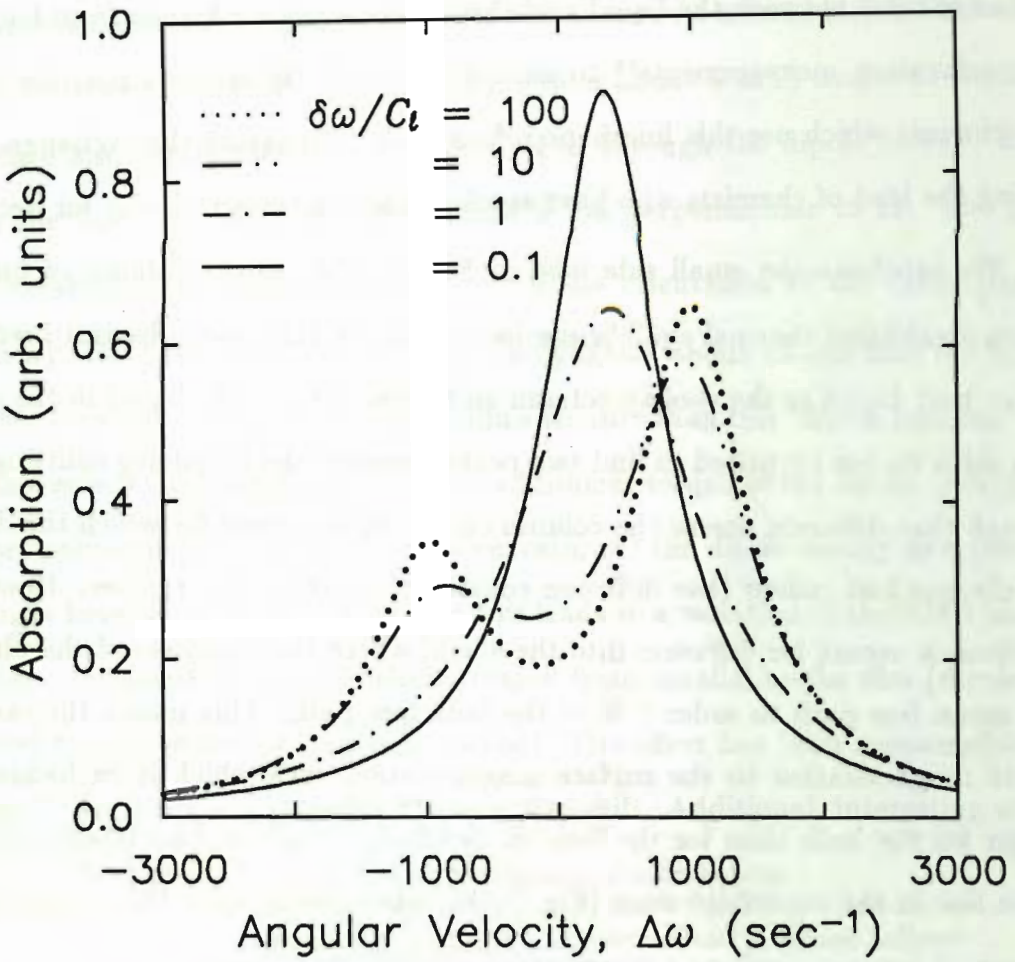

Figure 2.6

The NMR absorption of two spin populations for different rates of magnetization transfer between them, as found using the Bloch equations. The frequency splitting is 2000 $\sec^{-1}$, and the right line has twice the magnetization of the left. Both lines have $T_2 = 2 \times 10^{-3}$ sec.

In Figure 2.6 we plot the result for various exchange rates, using linewidths and relative magnetizations typical of our experiments. The double-peaked structure is eradicated when $\delta\omega/C_l \sim 1$. Only minor variations in lineshape result from extending on in either direction beyond the three decades in exchange rate shown. For the largest frequency shifts which we encounter in the superfluid, exchange rates of order $10^5 \sec^{-1}$ are sufficient to motionally average the lines. In comparison, spin transport

across the films is ballistic in this regime with a characteristic time of 10^{-8} sec, and exchange rates between the liquid and the surface solid are known from longitudinal spin relaxation measurements[18] to exceed 10^{8}sec^{-1}. It appears possible to design experiments which use this lineshape information to measure the exchange rate, following the lead of chemists who have studied reaction rates this way for decades.

We attribute the small side lobe in Figure 2.5a to the column of bulk liquid which establishes thermal equilibrium in the cell. In this case subscript l would refer to the bulk liquid in the cooling column and subscript s to the liquid in the stack. At first sight we are surprised to find two peaks, because the frequency splitting is small enough that diffusion across the column can occur in a time for which the dephasing is only one-half radian (the diffusion constant[16] is about 10 cm^2/sec. However, the bottleneck occurs for diffusion into the stack, where the thickness of the films limits the mean free path to order 1 % of the bulk free path. This makes the ratio of the liquid magnetization to the surface magnetization with which it exchanges grossly larger for the bulk than for the fluid in the films. The side lobe is absorbed by the main line in the superfluid state (Fig. 2.5b), where we imagine that some faster spin transport process, perhaps a supercurrent, facilitates the averaging.

Armed with this knowledge of background shifts and exchange-averaged lineshapes, we are prepared to isolate the response of the superfluid. The anisotropy of the A phase order parameter is characterized by two unit vectors, $\vec{\mathbf{d}}$ and $\vec{\mathbf{l}}$, which respectively determine the directions of the spin quantization axis and the orbital symmetry axis of the Cooper pairs. The anisotropic terms of the free energy density are[24]

$$F = \frac{1}{2}\alpha\chi(\vec{\mathbf{d}}\cdot\vec{\mathbf{H}})^2 - \frac{3}{5}g_D(T)(\vec{\mathbf{d}}\cdot\vec{\mathbf{l}})^2 + F_{grad} \qquad (2.4)$$

where H is the static field, χ is the bulk susceptibility and α is a measure of the susceptibility anisotropy. The second, or dipole, term is minimized when $\vec{\mathbf{d}}$ and $\vec{\mathbf{l}}$ are

collinear, an arrangement which therefore obtains in sufficiently large systems. $g_D(T)$ is proportional to the square of the order parameter. At a boundary, $\vec{l}$ will be aligned along the surface normal[25]. In small (less than about 5 mT) magnetic fields, then, a surface also determines the orientation of $\vec{d}$, through the dipole energy. In larger fields the Zeeman energy dominates, and $\vec{d}$ lies perpendicular to $\vec{H}$. The gradient term establishes the length scale on which the orientation of the order parameter may vary. Here the effect of a wall on $\vec{l}$ propagates about 10 μm into the liquid. A uniform $\vec{l}$ texture is therefore found in films thinner than this 'dipole bending' length. A transverse NMR shift is caused by an additional torque of the dipole energy on the Cooper pair spins, proportional to the curvature of the dipole energy as a function of the angle between $\vec{d}$ and $\vec{l}$[24]. For films, this leads to a variation of the NMR shift from positive to negative when the field is rotated from parallel to the film (dipole-locked texture) to perpendicular (dipole-unlocked). The effect has been measured by AKP. Takagi [26] was the first to predict the negative shift. Additional, interesting structure in the low field regime still awaits experimental confirmation.

The transverse resonance frequency in the superfluid A phase follows

$$\nu^2 = \nu_L^2 + \frac{c}{4\pi^2}\Omega^2(T) \tag{2.5}$$

where ν_L is the unshifted Larmor frequency and $\Omega(T)$ is the (field independent) rate of the longitudinal resonance predicted by Leggett[27], which grows with the order parameter. The factor c is dependent both upon the texture and the tipping angle, ϕ, in pulse NMR. For the bulk or dipole-locked case[28], $c = \frac{1}{4} + \frac{3}{4}cos\phi$. The frequency shift is symmetric about $\phi = 90°$ in the dipole-unlocked texture[29], with $c = -cos\phi$. Figure 2.8 shows the spin precession frequency for several tip angles as a function of inverse temperature, to linearize the background shift and to emphasize the low temperature behaviour. Note that it is essential to take the background into account

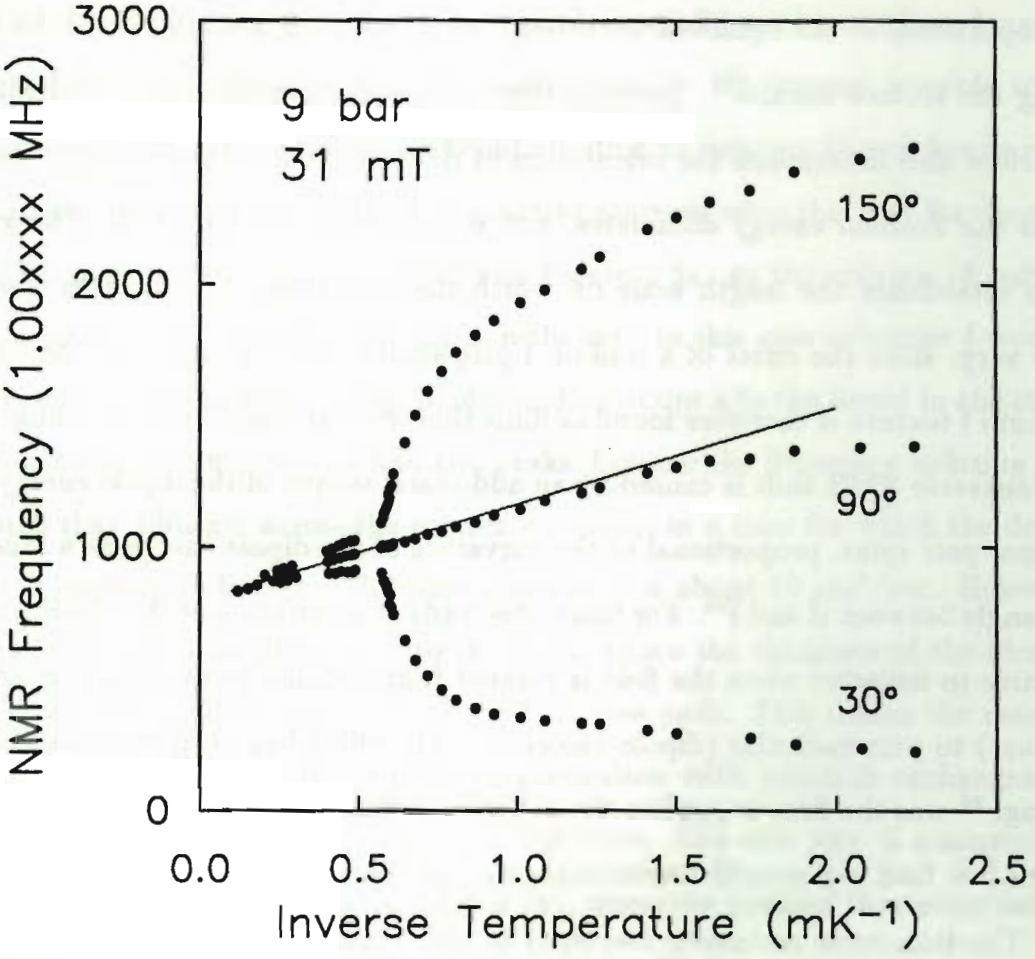

Figure 2.7

The NMR frequency for several tipping angles, versus inverse temperature to emphasize the superfluid region. The line is the fit to the normal phase data from Figure 2.4. The bulk transition at this pressure occurs at $T^{-1} = 0.56\text{mK}^{-1}$. The behaviour is characteristic of the A phase in the dipole-unlocked texture.

in order to see the symmetry about 90°. We have confirmed the cosine dependence with additional tip angles[1].

The data of Figure 2.4 occupy the region below 0.5 mK^{-1} in Figure 2.7 . The line accompanying the 90° data is the $1/T$ fit from the earlier figure. The deviation of the data from the line at low temperatures can be attributed to increasing thermal time constants for the protons in the mylar.

Eliminating the mylar proton and solid ^{3}He layer shifts, and correcting for motional averaging, we can extract the unadulterated NMR frequency shift of the liquid in the superfluid phase. This is shown for the transition region at 9 bar in Figure 2.8. We show the absolute value of the shift to emphasize the symmetry of the 30° and 150° pulse angle results. The straight line is a fit to determine the slope of the shift at the transition, which is a measure of the strength of the order parameter in the films. The Ginzburg-Landau theory predicts the ratio of this slope to the same quantity for bulk. The initial slope is conventionally referred to as $f^2(P) = d\Omega^2/d(\frac{T}{T_c})$. The Ginzburg-Landau prediction for the initial slope of the frequency shift at T_c^{film} for a film with rough (diffusely scattering) surfaces is simply $\frac{2}{3}f^2_{bulk}(P)$. This assumes only that the temperature dependences of Ω^2_{bulk} and of the correlation length ξ are, respectively, $(1-\frac{T}{T_c})$ and $(1-\frac{T}{T_c})^{-\frac{1}{2}}$. The result is independent of the actual thickness, d, of the film because the dimensionless thickness, $w = \frac{d}{\xi}$, is a constant (π) at the transition. Of course, the temperature window over which w remains small shrinks into invisibility for large d. The actual expression for the NMR shift near T_c is

$$\frac{\Omega^2}{\Omega^2_{bulk}} = \frac{2}{3}(1-(\frac{\pi}{w})^2). \tag{2.6}$$

For the data as plotted in Figure 2.8 , the slope can be written

$$\frac{d\delta\nu}{d(\frac{1}{T})} = \frac{T_c^{film} f^2_{bulk}(P) cos\phi}{3\nu_L}. \tag{2.7}$$

Using bulk data (see below), we find 6.9×10^3Hz · mK, in fair agreement with the fit to our data, 5.7×10^3Hz · mK.

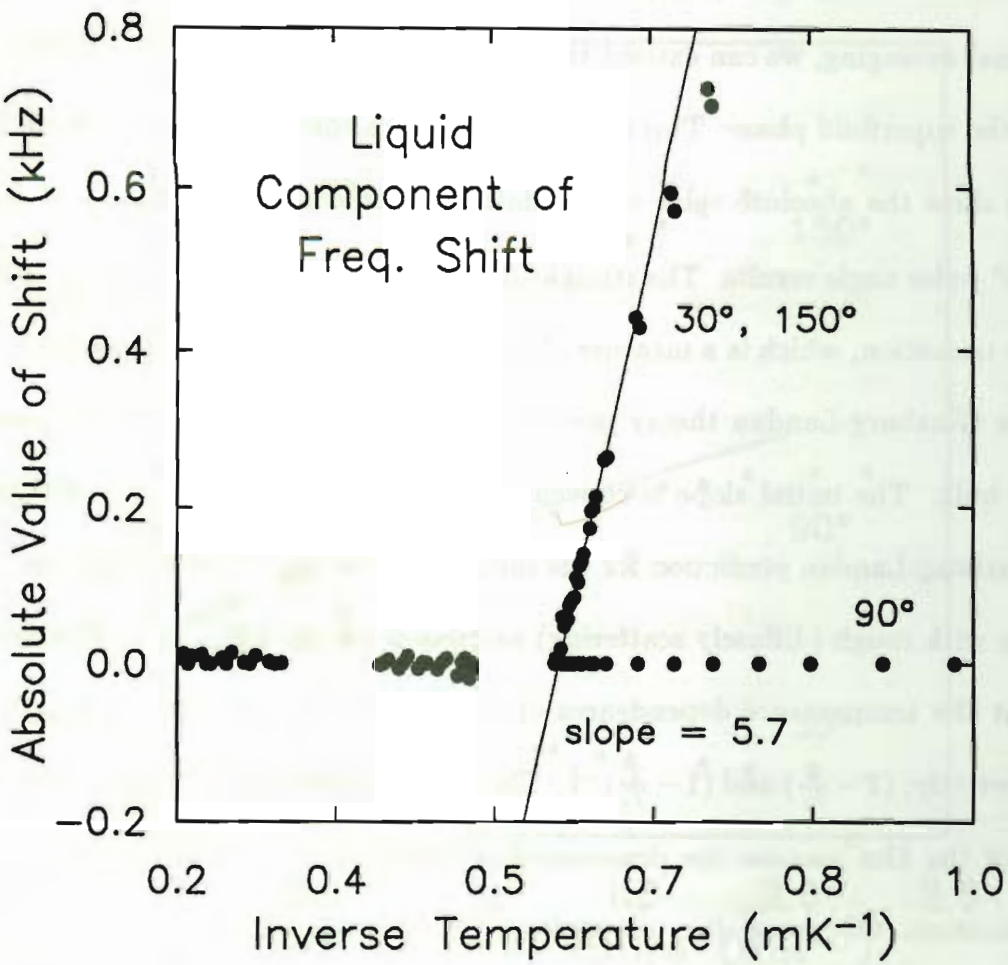

Figure 2.8

The NMR frequency shift of the ^{3}He liquid, liberated from the many burdens which encumber it in the raw data.

At present, the low pressure half of the bulk phase diagram (where the B phase alone occurs normally) is essentially a no-man's land as far as the A phase is concerned. It is possible to stabilize the A phase with a magnetic field[30], and there exists one measurement for the 6 μK sliver of A phase in 28 mT at 2 bar[31]. To our knowledge this is the only data point. We use this result, and the numbers for intermediate pressures obtained by interpolation. We are encouraged that estimates of the A phase frequency shifts based upon the B phase measurements of Hakonen *et al.* (private comm.) seem to agree rather well with the interpolation. The ratio of these shifts is determined by

$$\frac{\Omega_A^2}{\Omega_B^2} = \frac{2}{15}\frac{\chi_B}{\chi_A}\frac{3\beta_{12}+\beta_{345}}{\beta_{245}} \tag{2.8}$$

where the ξ's are the experimental susceptibilities, and $\beta_{ijk} = \beta_i + \beta_j + \beta_k$ (see eq. 1.9). The B phase susceptibility has been measured by Scholz (Ph.D. thesis, Ohio State 1981), and the A phase value is very nearly the same as that of the normal liquid. The strong coupling corrections are given in Ref. 43. $\beta_{245}/(3\beta_{12}+\beta_{345})$ is sometimes written $\bar{\beta}_{245}$ (Ref. 2.10).

Figure 2.9 displays a comparison of our experimental frequency shift slopes, $-A(P)f^2(P)$, and the Ginzburg-Landau prediction for a range of pressures. The factor $A(P)$ represents the backgrounds and effects of exchange averaging with the solid magnetization, which in this case are folded into the Ginzburg-Landau estimate (the line in the figure) rather than removed from the data. From the measurements at 9 bar, we extend the ratio of liquid and solid magnetizations to other pressures using the known pressure dependences of the liquid molar volume and magnetic Fermi temperature[32,16]. We assume that pressure dependence of the number of atoms in the solid ^{3}He layer is negligible, as has been found in some other experiments[33]. Schuhl et al.[10] have evidence of the number of atoms in the solid ^{3}He layer increasing by 40% from 0 to 25 bar on a fluorocarbon substrate. This effect decreases the slope of the solid line in Figure 2.9 by a small amount (the solid layer affects the liquid signal less at higher pressures because of the increase in the superfluid transition temperature). The evolution of the surface ^{3}He layer with pressure on a variety of substrates is an interesting topic for further study. The continuous solidification model of Ref. 18 (based on the pressure gradient at the wall due to the van der Waals interaction) is unrealistic in assuming that the solid/liquid phase boundary near the wall occurs at the solidification pressure of the bulk. The amorphous nature of the surface tends to inhibit the growth of the solid (see Chapter 3).

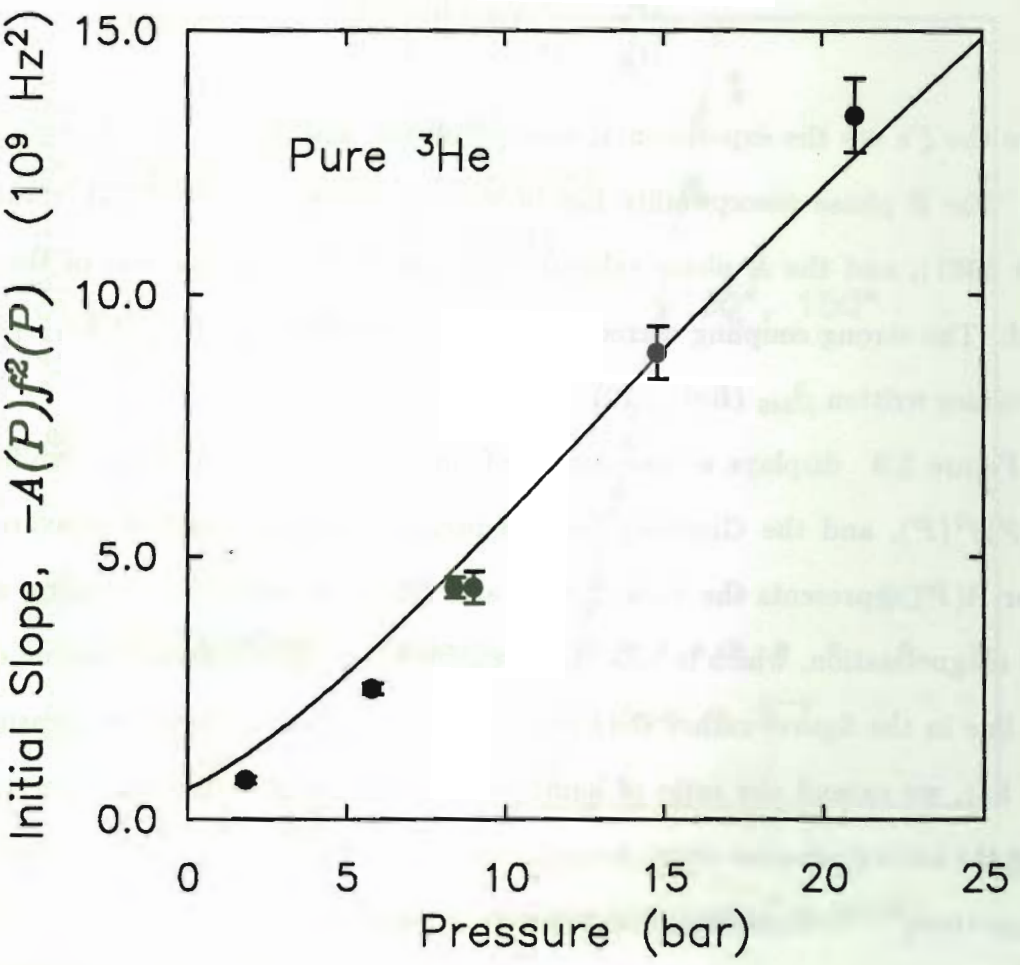

Figure 2.9

The symbols are our measured initial slopes of the NMR frequency shift for pure ^{3}He at a variety of pressures, using 30° tipping pulses. The solid line represents the slopes that we expect within the Ginzburg-Landau theory, based on our knowledge of the magnetization in the system (see text).

We are able to tilt the static magnetic field on the cell using large room temperature Helmholtz coils to apply a horizontal field. Note that this field is able to penetrate the superconducting solenoids in persistent mode, as these (vertical) coils cannot screen fields in the horizontal plane. This enables us to confirm our identification of the A phase by observing the expected variation of texture with field direction. In Figure 2.10a we show results for a 7.7 mT field in two different orientations. The

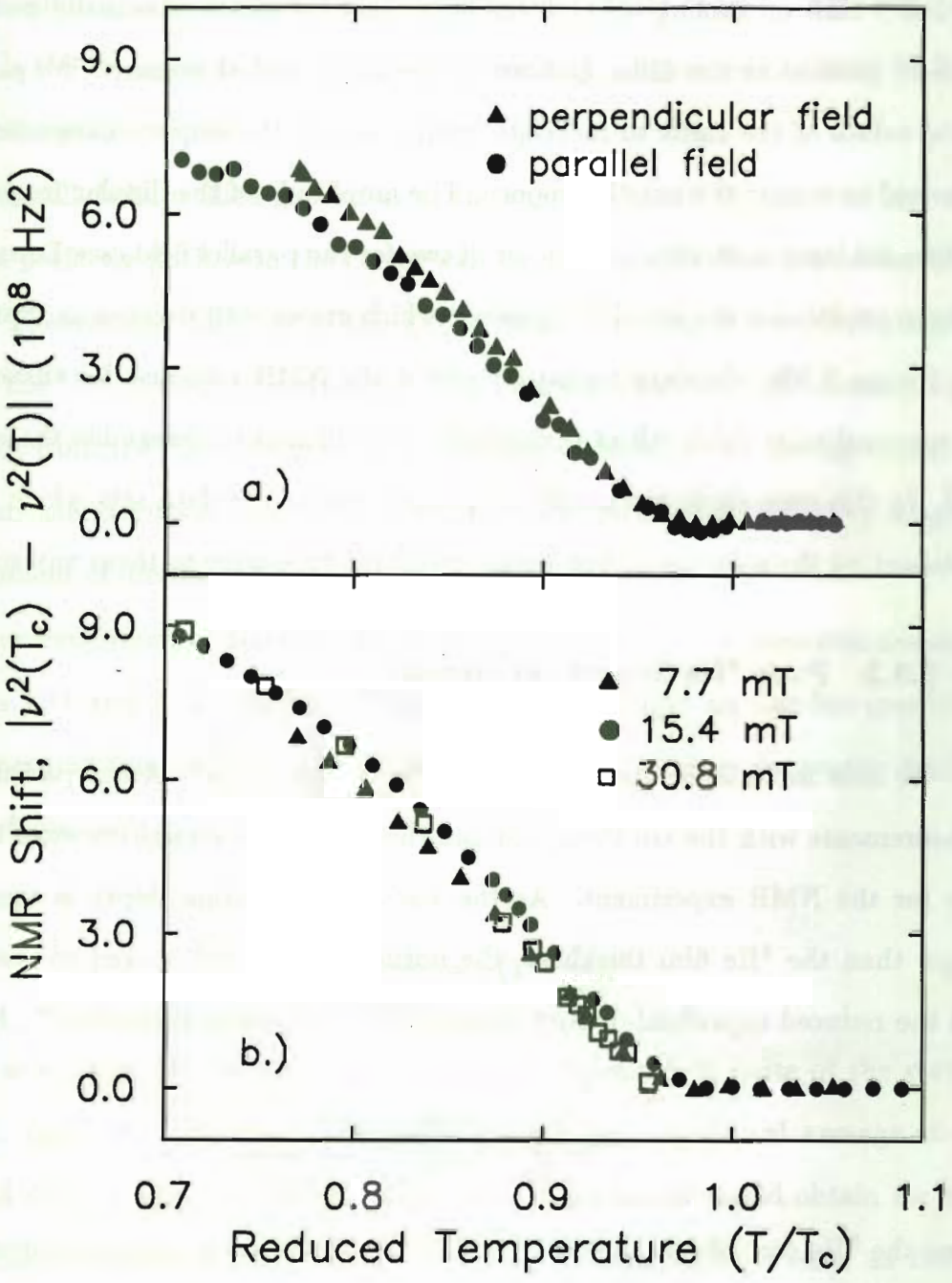

Figure 2.10

The field independence of the Leggett frequency (here $\Omega^2/4\pi^2$), defined in Equation 2.5. The results in a.) are measured in a 7.7 mT field at a liquid pressure of 9 bar. The field direction indicated is with respect to the plane of the films. The parallel field stabilizes the 'dipole-locked' texture and changes the sign of the frequency shift. The difference which grows with decreasing temperature is an effect of the solid layer (these are raw data). Part b.) shows results for three magnitudes of the perpendicular field. The texture is field independent in this range.

frequency shift on cooling through the superfluid transition is actually positive with the field parallel to the films, indicating the dipole-locked texture. We plot the absolute values of the shifts to facilitate comparison of the slopes. These data are not corrected to isolate the liquid response. The amplitude of the dipolar frequency shift in the solid layer is smaller by a factor of two for the parallel field (see Equation 2.1), perhaps explaining the small discrepancy which grows with decreasing temperature.

Figure 2.10b displays measurements of the NMR response for three values of the perpendicular field. All of these fields are sufficient to determine the orientation of $\vec{\mathbf{d}}$. In this case there are small variations between the data sets which cannot be explained by the solid layer, but we are reluctant to ascribe to them any significance.

2.3.2 Pure ^{3}He Superfluid Density

We now move on to discuss the superfluid density, ρ_s . A comparison of these measurements with the Ginzburg-Landau theory is more straightforward than is the case for the NMR experiment. As the viscous penetration depth is tremendously longer than the ^{3}He film thickness, the normal fluid is well-locked to the substrate and the reduced superfluid density is related to the oscillator period ,$\mathcal{P}$, by

$$\frac{\rho_s}{\rho} = \frac{\mathcal{P}(T_c) - \mathcal{P}(T)}{(1-\chi)(\mathcal{P}_{full} - \mathcal{P}_{empty})}, \tag{2.9}$$

when the ^{3}He contributes only a small fraction of the total moment of inertia of the oscillator. The complete ^{3}He component of the moment of inertia is responsible for a period shift $\mathcal{P}_{full} - \mathcal{P}_{empty}$, but imperfections in the flow paths keep a fraction, χ, of this coupled to the oscillator when the liquid is completely superfluid. We find $\chi = 0.27$ in a calibration with pure ^{4}He. ^{4}He develops its bulk superfluid density in a geometry of this size. We expected χ to be approximately half this size, based on Glenn Agnolet's experience with mylar[34] and the calculated momentum transfer

from oscillating superflow around the polystyrene spacer beads[35]. This substantial χ factor is the strongest indicator that the geometry falls somewhat short of the ideal of parallel plates.

A small, helium filled gap exists at the edge of the cell because the mylar sheets are not perfectly flush with the epoxy wall, and the grease does not perfectly fill the voids. The average thickness of this gap is 10 μm (see Chapter 3). It corresponds to 6 % of the ^{3}He moment of inertia and contributes a bulk superfluid density, which we subtract from the data. Note that the fractional effect of this helium excess on the NMR measurements is smaller by a factor of two, because of the heavy weighting of the moment of inertia at large radii.

Our experimental determinations of ρ_s/ρ at a variety of pressures are shown as Figures 2.11 and 2.12. In the transition region, the Ginzburg-Landau prediction for the superfluid fraction of a ^{4}He film (assuming that the order parameter vanishes at the surfaces) is[36]

$$\frac{\langle \rho_s \rangle}{\rho_{s,bulk}} = \frac{4}{3}(1 - \frac{\pi}{w}), \tag{2.10}$$

where w is again the dimensionless thickness, measured in units of the correlation length. $\langle \rho_s \rangle$ is the experimentally relevant quantity, the spatial average of the superfluid density across the width of the film. This result would obtain for the ^{3}He superfluid were it isotropic. We quote it for cultural purposes only, as the actual superfluid transition in ^{4}He films turns out to be of the Kosterlitz-Thouless variety and the applicability of a healing length picture to superfluid ^{4}He is questionable[37]. In the ^{3}He A phase, Equation 2.10 becomes[29]

$$\frac{\langle \rho_s^A \rangle}{\rho_{s,bulk}^A} = 0.6209(1 - (\frac{\pi}{w})^2). \tag{2.11}$$

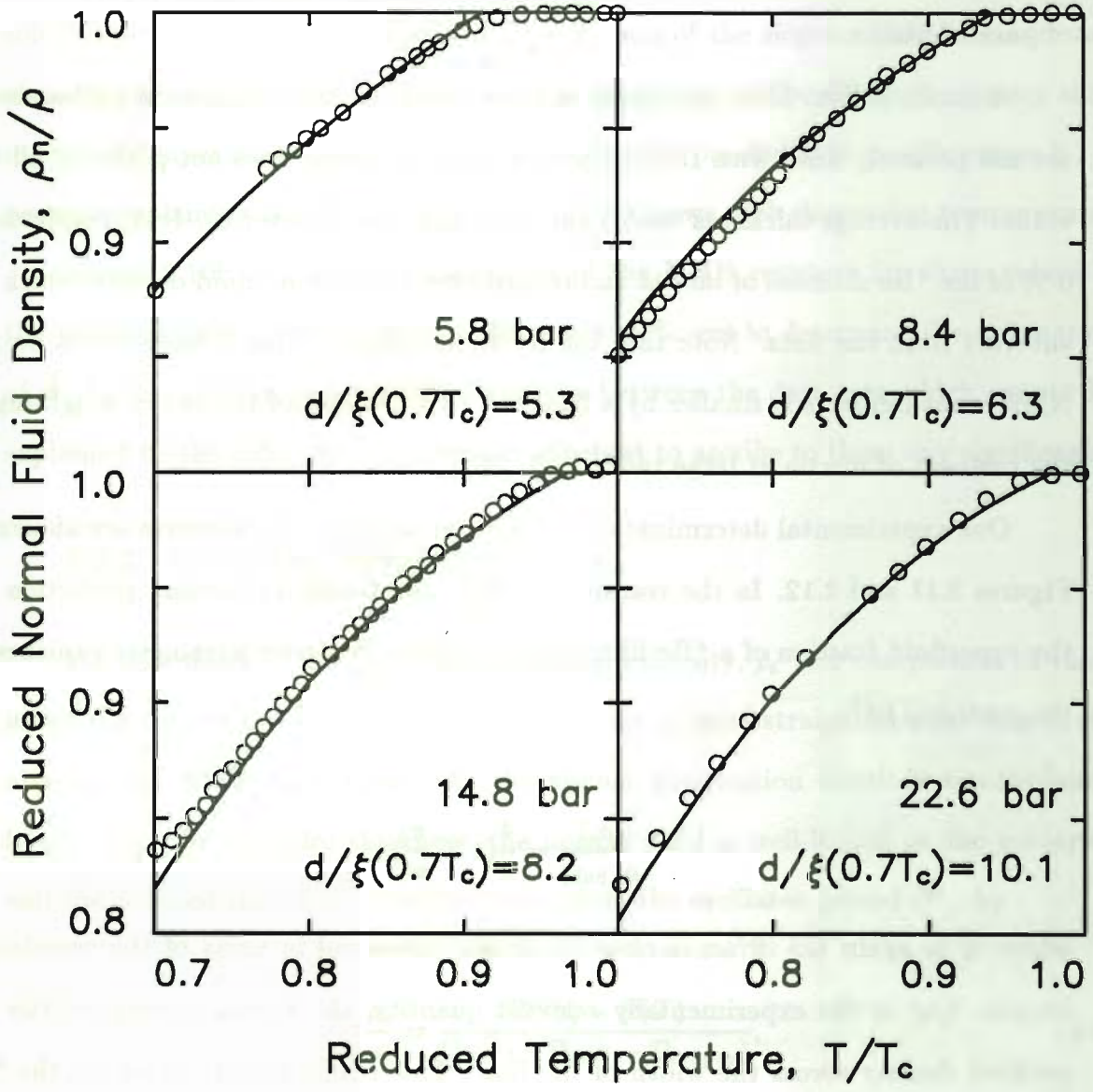

Figure 2.11

The normal fluid density of pure ^{3}He as measured by the torsional oscillator. The solid lines are the Ginzburg-Landau predictions based on Cornell data for the bulk B phase superfluid density, with *no* free parameters (see text for further discussion).

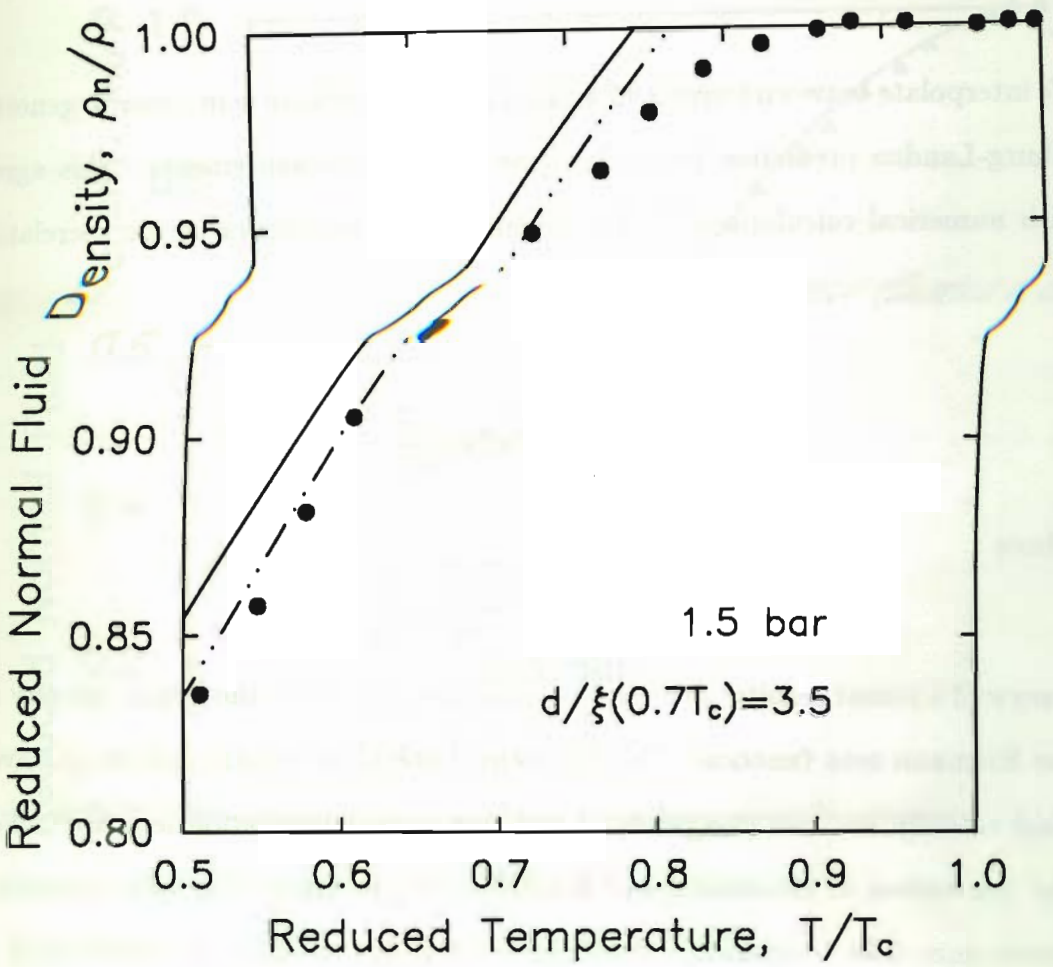

Figure 2.12

A lower pressure data set. The rounding near the film transition is more apparent, as the correlation length is a less strong function of temperature in the vicinity of the transition. The solid and dash-dot-dot Ginzburg-Landau lines take $d = 280$ nm and $d = 290$ nm, respectively.

This expression differs from Equation 2.10 by 7% near the transition ($w = \pi$); the prefactor is affected by an off-diagonal component of the order parameter that becomes non-zero during flow. For large thicknesses, the superfluid fraction is determined by the proportion of liquid within a distance of order $\xi(T)$ from the wall:

$$\frac{\langle \rho_s \rangle}{\rho} = 1 - \frac{k(w)}{w}. \tag{2.12}$$

When $w \gg \pi$, $k = \pi$ in the Kiknadze-Mamaladze calculation[36], whereas $k = 3.2$ for ^{3}He-A.

We interpolate between forms 2.11 and 2.12 at intermediate w in order to generate a Ginzburg-Landau prediction for comparison with our measurements. This agrees well with numerical calculations[38]. The temperature dependence of the correlation length is normally written

$$\xi(T) = \xi(0)(1 - \frac{T}{T_c})^{-\frac{1}{2}}, \tag{2.13}$$

where

$$\xi(0) = \sqrt{\frac{7\zeta(3)}{80}} \frac{\hbar v_F}{\pi k_B T_c}.$$

Greywall's recent results[3] are used to compute $\xi(0)$. v_F is the Fermi velocity and ζ is the Riemann zeta function. The Ginzburg-Landau description of the p-wave superfluid actually has two (longitudinal and transverse) correlation lengths[25]. Following the convention of Buchholtz and Fetter[39], $\xi(T)$ is taken to be the shortest (transverse) one. The temperature dependence in Equation 2.13 is correct only close to the transition ($\xi(0)$ is *not* the zero temperature correlation length). Einzel[40] gives a form, which we use, that interpolates between this and and the low temperature behaviour appropriate to the BCS gap. In fact it makes little difference which form is used over the temperature range of Figure 2.11 , and a numerical calculation is required to determine the correct dependence for the confined geometry at low T/T_c.

In Figure 2.13 we show the full temperature range. The Ginzburg-Landau result seems to overestimate the superfluid density at low T/T_c. This is opposite to the effect that I would expect on account of the temperature dependence of the boundary condition on the transverse component of the order parameter. A single qualitative argument apparently is an unreliable guide in these cases[29]. This matter awaits further investigation.

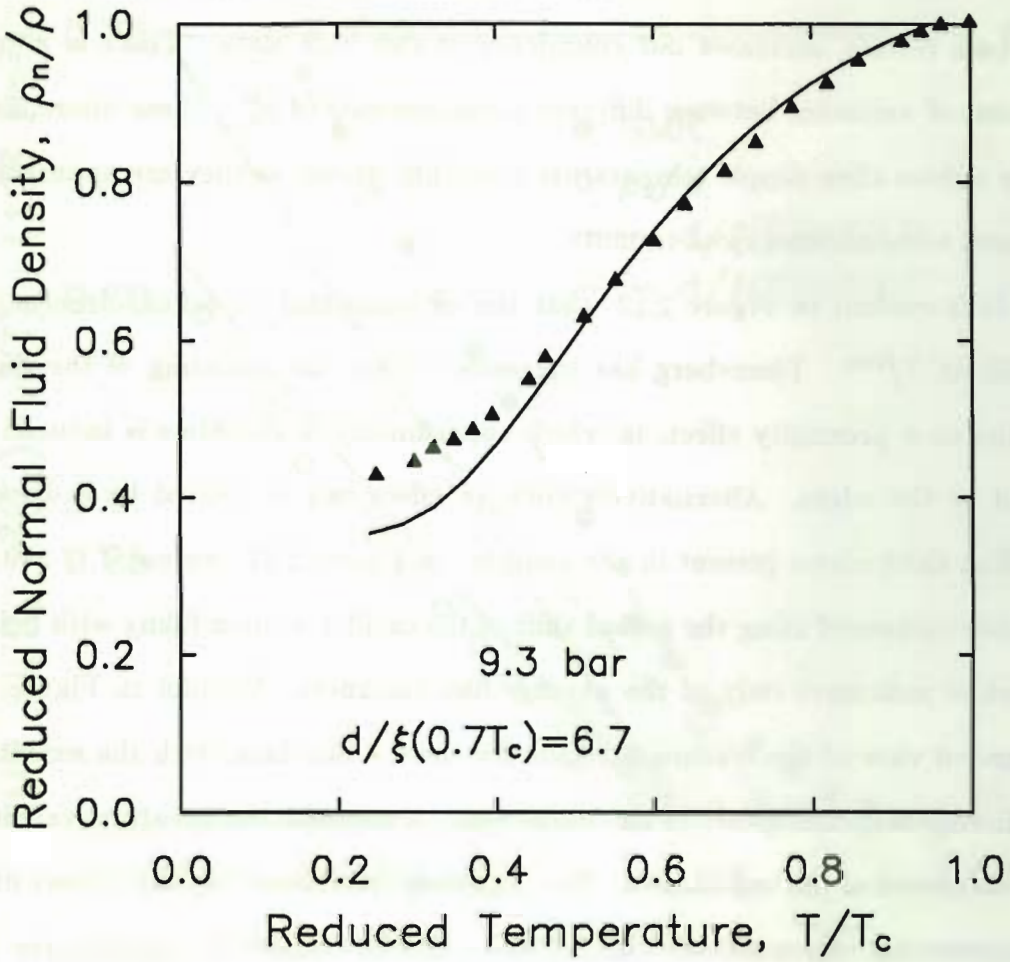

Figure 2.13

Comparison with Ginzburg-Landau theory over the full temperature range. The solid line is the prediction for d=300 nm.

It is necessary to elaborate a bit about the bulk data that we are using. The A phase superfluid density is anisotropic, and to our knowledge there exists only one measurement of the component, $\rho_s^{A,\perp}$ for flow perpendicular to $\vec{l}$. This was reported by Berthold *et al.*[41] for a 27 bar liquid pressure. The appropriate $\vec{l}$ texture was stabilized by a magnetic field. At other pressures we obtain the A phase superfluid density from B phase measurements, through $\rho_s^{A,\perp} = 2\rho_s^B/5\bar{\beta}_{245}$. We use the most recent Cornell data[42] for the B phase superfluid density, and find close agreement

with the Berthold result at 27 bar. This, as well as the apparent consistency with our own results, increases our confidence in this bulk data. There is a surprising amount of variation between different measurements of ρ_s^B. These discrepancies are more serious than simple temperature scale differences, as they are apparent even at reduced temperatures close to unity.

It is evident in Figure 2.12 that the experimental superfluid density does not vanish at T_c^{film}. Thuneberg has suggested[29] that the rounding of the data could be due to a proximity effect, in which superfluidity in the films is induced by bulk liquid at the edges. Alternatively such an effect can be caused by a dispersion in the film thicknesses present in the sample. In Figure 2.11 we use $d = 280$ nm, our number *measured* using the period shift of the oscillator upon filling with helium, but therefore indicative only of the *average* film thickness. We plot in Figure 2.14 an expanded view of the transition region for the 8.4 bar data, with the simultaneously acquired NMR shift included for comparison. A common temperature scale is assured by the nature of the experiment. The Ginzburg-Landau curves which best fit the two measurements extrapolate to slightly different film transition temperatures. The two solid lines show the expected torsional oscillator and NMR responses for $d = 300$ nm. A superior fit to the NMR data is obtained with the dash-dot lines, corresponding to $d = 350$ nm. Note that these fits assume that whatever causes the rounding has no consequences at lower temperatures.

It is interesting to plot the NMR frequency shift against the normal fluid density. Inspecting equations 2.6 and 2.10, we see that the result should be a straight line with slope equal to 1.07 times the slope of the same line for bulk ^{3}He-A. In Figure 2.15 the deviation of our data from this behaviour is apparent. One possibility is to explain this as a consequence of inhomogeneity in the sample, and the fact that the torsional oscillator response is sensitive to how regions of superfluid are connected while NMR is a local probe. Considering the construction of the mylar stack, we expect that

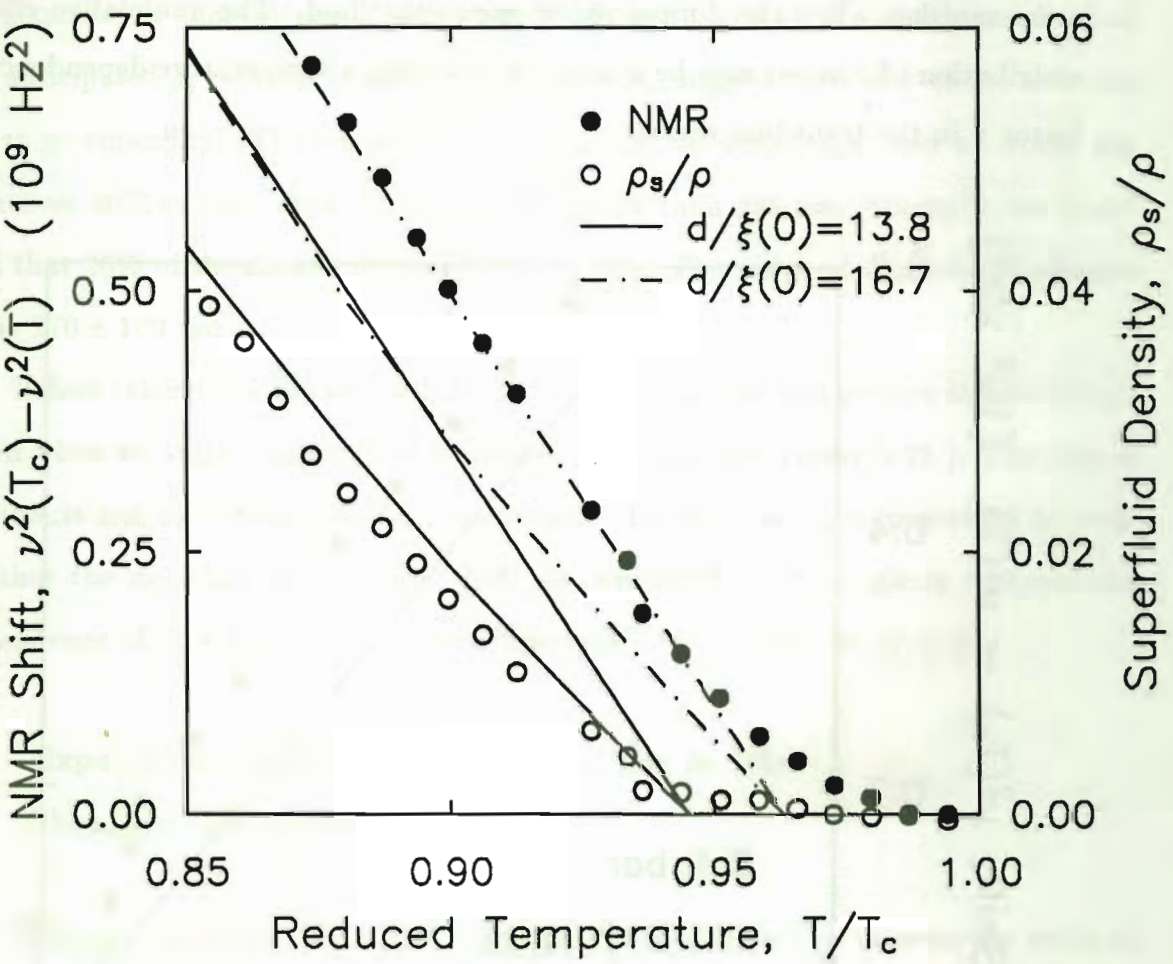

Figure 2.14

Detail of the Ginzburg-Landau fits to the 8.4 bar data set. The NMR and torsional oscillator measurements extrapolate to slightly different T_c^{film}'s, corresponding to $d = 350$ and 290 nm, respectively. This suggests that the geometry is not perfectly characterized. The parallel, straight solid and dash-dot lines are the NMR predictions for the two thickness. The slightly curved lines show the expected superfluid density.

the thickness variations can be approximated by 'dimples' with some distribution of heights. The dimple radii are unknown, but assumed to be much smaller than the lateral extent of the films. There is then a distribution of superfluid transition temperatures for the liquid under the dimples. In oscillating superflow around an isolated normal-phase dimple, an additional 'virtual mass' is coupled to the substrate,

equal to half of the mass of the superfluid displaced by the dimple[35]. This virtual mass vanishes when the dimple region goes superfluid. The cumulative effect of a distribution of dimples may be described by adding a temperature dependence to the factor χ in the transition region.

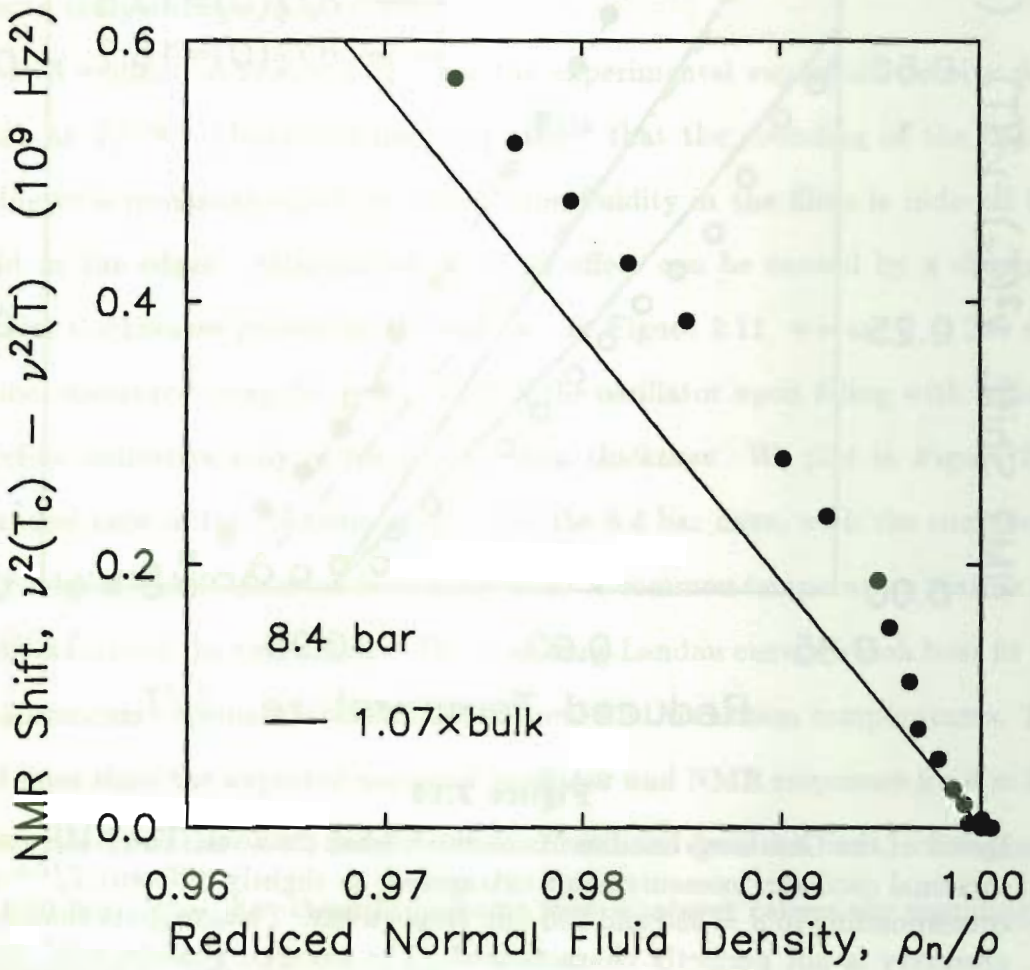

Figure 2.15

The frequency shift and normal fluid density plotted one against the other. The solid line shows Ginzburg-Landau behaviour. The deviation is suggestive of dimpling of the films, as described in the text. This result is very sensitive to the corrections required to isolate the liquid NMR signal.

This picture is very arbitrary and neglects the possibly significant proximity effects. Nevertheless, there is simple procedure by which we can estimate the distri-

bution of thicknesses from the data of Figure 2.15, to gain some feeling for how well the geometry is characterized. When the NMR shift is $3 \times 10^8 \mathrm{Hz}^2$, for example, $\frac{1}{3}$ of the anticipated ρ_s remains coupled as virtual mass, suggesting that $\frac{2}{5}$ of the area has yet to go superfluid. The temperature at that point is $0.93T_{c,\mathrm{bulk}}$, and we would say that over 40% of their area, the films are thinner than 245 nm. Similarly we would find that 20% of the area is thinner than 190 nm. The range of thicknesses appears to be 270 ± 100 nm.

Before taking this too seriously, however, we note that this picture in fact breaks down when we start changing the boundary condition (see Figure 2.21). The reason for this is not understood at the present time. In any case, it is important to realize that the modeling procedure of Ref. 44, which effectively neglects temperature dependence of χ, will always reproduce the bulk line in a $\Delta\nu^2$ vs. ρ_n/ρ plot.

2.4 Experiments on Dilute Mixtures of ^{4}He in ^{3}He: Changing the Boundary Condition

When a container is filled with a binary liquid mixture, one expects the walls to be coated preferentially by the component having a stronger attraction to the surface. In the case of isotopic mixtures of helium, the van der Waals interaction is the same for both components and it is the zero point energy that makes the difference. By virtue of its greater mass, the zero point motion of a ^{4}He atom is less than that of a ^{3}He atom. That is, the ^{4}He species is effectively smaller, and both covers the surface with a greater number density and sits slightly deeper in the van der Waals potential well.

The first experimental consequence of this was found by Laheurte and Keyston[45], who observed a ^{4}He superfluid film at a temperature above phase separation for a dilute mixture of ^{4}He in ^{3}He. The surface ^{4}He film can have a large effect on the boundary condition for scattering of ^{3}He quasiparticles, which seriously complicates

attempts to measure the effective viscosity of mixtures. This effect, once believed to be well characterized[46], has recently proven to have more subtleties.[47] In addition to altering the momentum scattering, the presence of small amounts of ^{4}He in ^{3}He has an enormous influence on energy transport across boundaries. When the ^{3}He next to a surface is promoted into the liquid, the important magnetic channel coupling to spins in the solid is cut off[48] and the Curie-Weiss magnetization of the localized atoms disappears[13]. In this section we present results which demonstrate these sorts of effects in a dramatic way, exploiting the surface sensitivity of superfluid ^{3}He films. The mixtures that we deal with are sufficiently dilute that they phase separate at the surfaces, leaving most of the helium as essentially pure ^{3}He. Typically the ^{4}He is admitted to the cell before the ^{3}He, rather than together as a mixture. The surface area of the silver sinter acts as ballast which makes the total quantity of ^{4}He large enough to be easily controlled. It also helps us to overcome solution effects in the higher temperature work discussed in Chapter 3. The ^{4}He concentration profile at the surface in these systems has been discussed by Peshkov (Proc. LT-14, p. 356).

2.4.1 Calibration and Characterization of Surface ^{4}He Films

The high sensitivity of the torsional oscillator technique enables us to calibrate the ^{4}He surface coverage using the Kosterlitz-Thouless transition[49]. The first monolayer of ^{4}He is densest, at about 18 μmole/m^2. The density drops rapidly with distance from the surface, to about 13 μmole/m^2 for liquid layers at saturated vapor pressure. An inert layer of 28 μmole/m^2 must be completed before any superfluid appears. The Kosterlitz-Thouless transition temperature rises, linearly at first, with additional coverage beyond this critical value. A typical transition in this cell is shown in Figure 2.16.

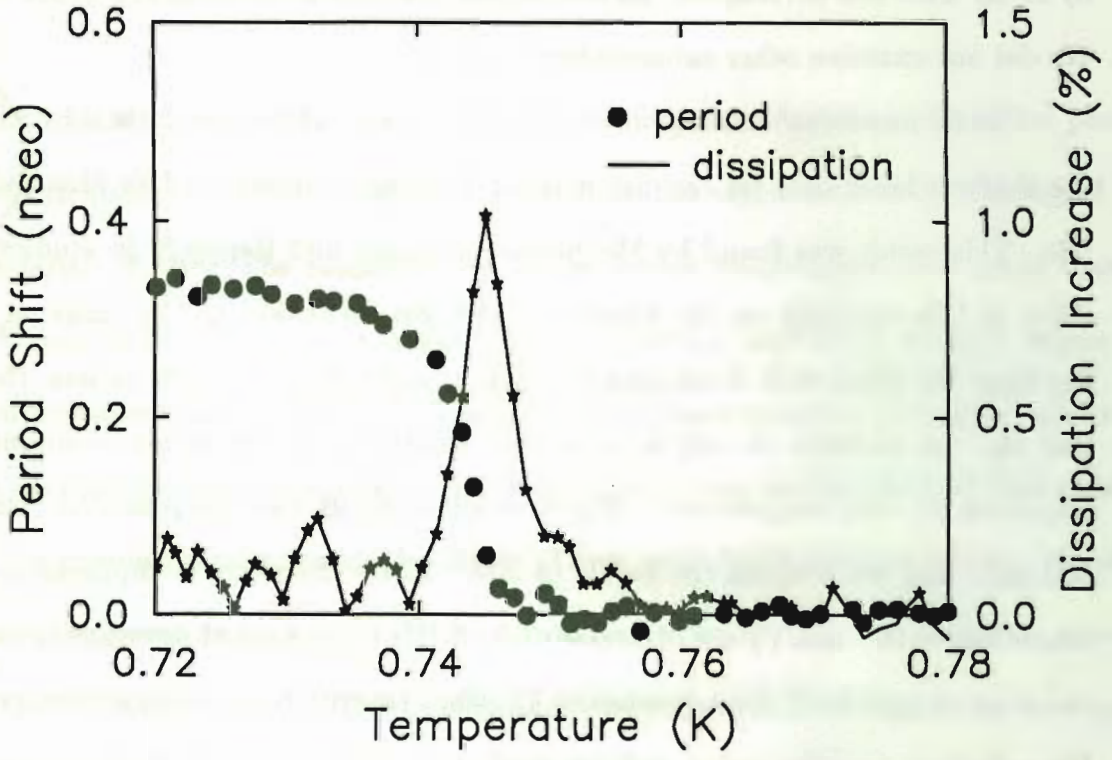

Figure 2.16

The signature of a Kosterlitz-Thouless transition in a ^{4}He film in this cell. The transition temperature is used to calibrate the ^{4}He coverage, using the results of Ref. 34.

We introduce the ^{4}He into the empty cell at 8K in an effort to obtain uniform submonolayer coverages. The refrigerator is relatively slow to start from this temperature, giving the film a few hours to anneal. The anneal was unsuccessful for our first dose. We admitted enough atoms to complete a monolayer, but achieved a coverage on the mylar of only $\frac{1}{4}$ monolayer. We are able to measure submonolayer coverages using the low temperature magnetization or the spin-lattice relaxation time, T_1, of the ^{3}He. T_1 is surface dominated[50] and is increased a factor of 50 by multilayer ^{4}He coverages in our experiment. Our pure ^{3}He T_1 is 30 msec at 5 mK and 31 mT, in close agreement with the results of Hammel[14]. The T_1 increased by a factor of three with $\frac{1}{4}$ monolayer of ^{4}He, while the Curie-Weiss component of the magnetization decreased

by 25 %. This low coverage of ^{4}He had no discernible effect on the superfluid density. We did not examine other submonolayer coatings.

The 32 μmole/m^2 coverage in Figure 2.20 is special because it is approximately the thickest layer that we can use without forming a superfluid ^{4}He film under the ^{3}He. This result was found by McQueeney, Agnolet and Reppy [55] in studies of the effect of ^{3}He coverage on the Kosterlitz-Thouless transition in ^{4}He films on mylar. For bare ^{4}He films with Kosterlitz-Thouless transitions at 500 mK or less, they find that the the addition of only a couple of monolayers of ^{4}He seems to suppress the transition to zero temperature. The transition of our bare 32 μmole/m^2 film is at 300 mK, and we confirm the result of Ref. 55 by observing a suppression of the transition to 200 mK by an 18 μmole dose of ^{3}He. The quoted coverage is based on the data of Agnolet[34] for a Kosterlitz-Thouless transition at the same temperature. His substrate was also mylar, and the temperature is low enough that vapor pressure effects are negligible (important because the result is then independent of the ratio of surface area to open volume in the cell). We can estimate the total surface area in the cell from the metered quantities of helium. The ^{4}He dose leading to the Kosterlitz-Thouless transition yields 8 m^2, while the ^{3}He dose produces 7 m^2. These numbers roughly correspond to a silver sinter surface area of 2 m^2/gm, in good agreement with most BET measurements of other groups. The geometric surface area of the mylar in our cell, 0.2 m^2, is only a small fraction of this total area, so our determination rests heavily on the assumption that the helium coverages are the same on mylar and on silver sinter.

For coverages thick enough to exhibit superfluidity when submerged in ^{3}He, we find some drift of the ^{4}He transition temperature with time (on the scale of days). This is probably due to ^{4}He going into solution in the warmer sections of the fill capillary. Future work of this type would best be performed with a valve on the mixing chamber.

2.4.2 NMR Results with Surface ^{4}He

In Figure 2.17 we show the low temperature magnetization and normal phase NMR frequency of a ^{3}He sample separated from the mylar surface by a lining of 70 μmole/m^2 of ^{4}He. The magnetization of the lowest temperature data point shown in Figure 2.17a is four times larger before pre-plating, indicating the high degree of accuracy to which the Curie-Weiss component has been removed. Frequency shifts in the normal phase are also gone (Figure 2.17b), including the background shift caused by the proton polarization in the mylar. These spins loose thermal contact at some higher temperature because of the vast increase in spin-lattice relaxation time caused by the ^{4}He buffer layer[50]. The tipping angle dependent shift of Figure 2.4 of course goes the way of the Curie-Weiss magnetization.

Some normal phase lineshapes for the 70 μmole/m^2 surface ^{4}He sample are displayed in Figure 2.18 . The side-lobe left behind by the growing mylar polarization is gone (compare Figure 2.5 , but be aware that the static field is not exactly the same for both). We have not traced the origin of the slight skew of the line at large tipping angles. Spin waves ought to appear on opposite sides of the line for pulses on opposite sides of 90°.[51] See Appendix B for large tipping angle spin waves in the superfluid. We have not pursued this issue by varying the field gradient.

Raw NMR frequency shifts from the Larmor resonance at 1 MHz are plotted in Figure 2.19 . The background effects in pure ^{3}He are so large at low temperatures and low pressures that there is no precise indication of the superfluid transition in the NMR data. The liquid behaviour is dramatically resolved by the addition of ^{4}He, indicated by the solid symbols in the Figure.

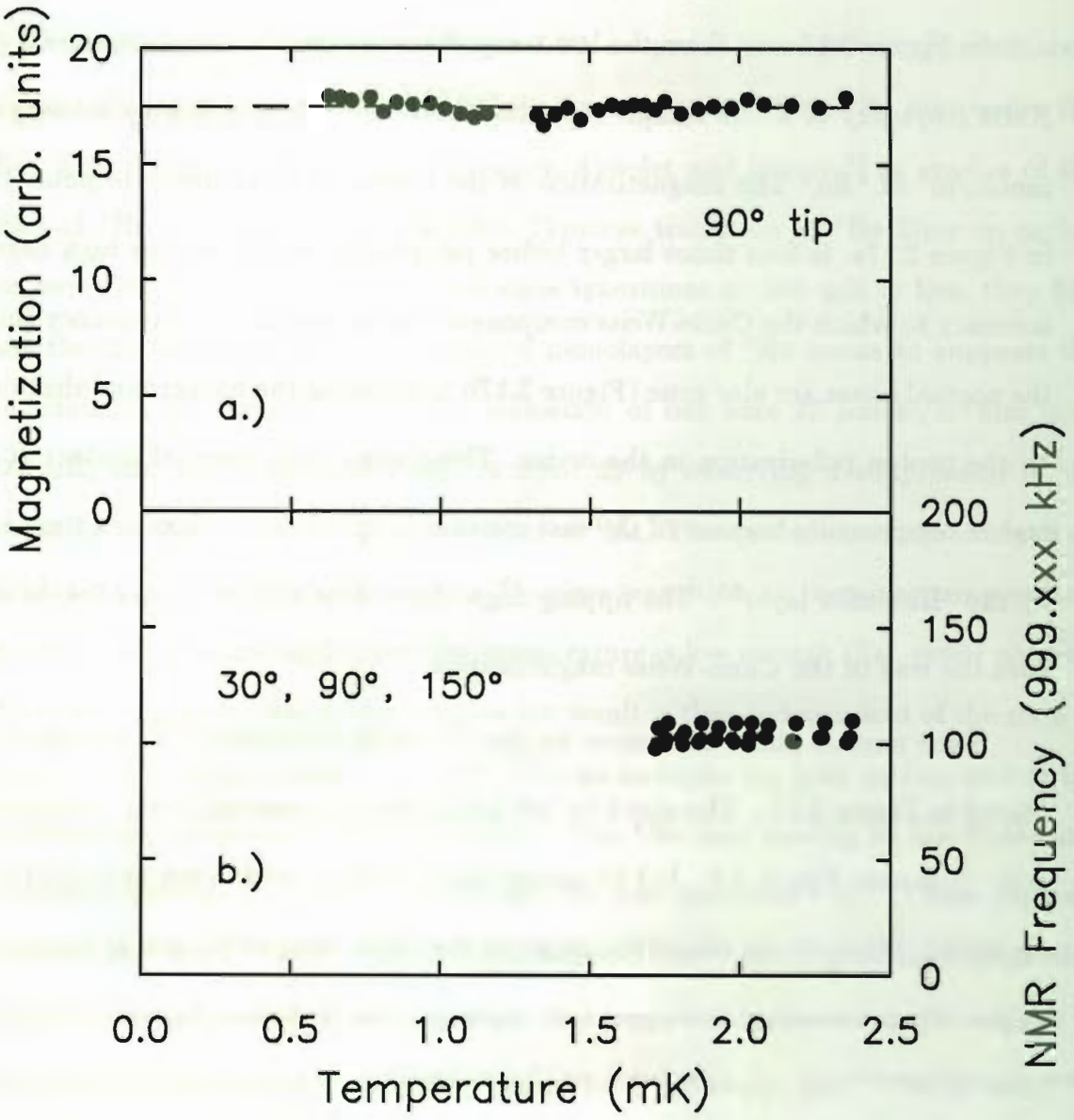

Figure 2.17

The NMR response of the ^{3}He sample with a 70 μmole/m^2 coverage of ^{4}He on the mylar surfaces. This is a 9 bar data set, and the superfluid transition is at 1.7 mK. The Curie-Weiss component of the magnetization has been eliminated, and there is no longer a significant frequency shift in the normal phase (compare Figures 2.4 and 2.5).

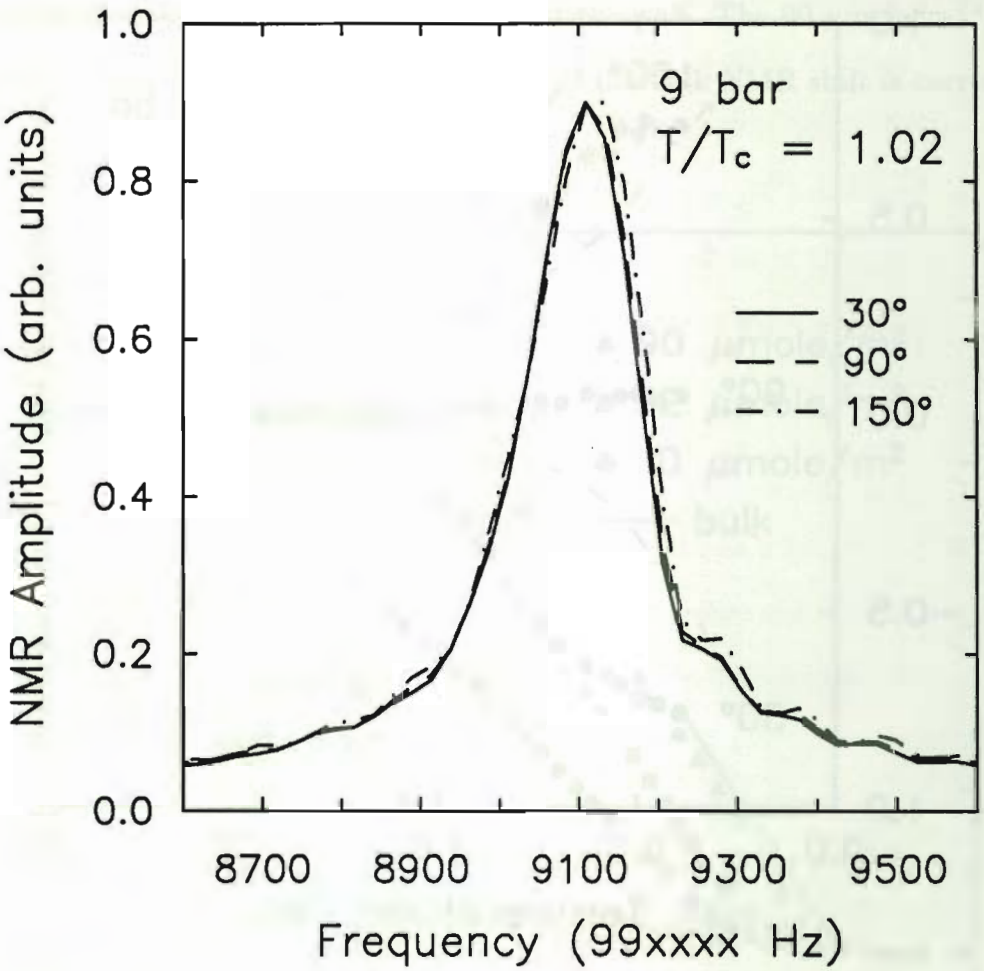

Figure 2.18

Normal phase lineshapes with ^{4}He coated surfaces. The tipping angle dependence is negligible.

It is most interesting to compare the dilute mixture NMR shifts with the liquid behaviour which we determine from the pure ^{3}He data. Some results at 8.5 bar are shown in Figure 2.20 .† The 0 μmole/m^2 (i.e., pure) data has been purged of

† Many of the results reported here were measured in the environment of 9 bar. Why? It is important to keep the correlation length fixed as other parameters are varied, and not all of the measurements were repeated at a number of pressures. We would prefer to operate at the lowest possible pressure in order to minimize the dimensionless thickness of the films, but two practical considerations prevent us from going all the way down to zero bar. One is the strong temperature dependence of the

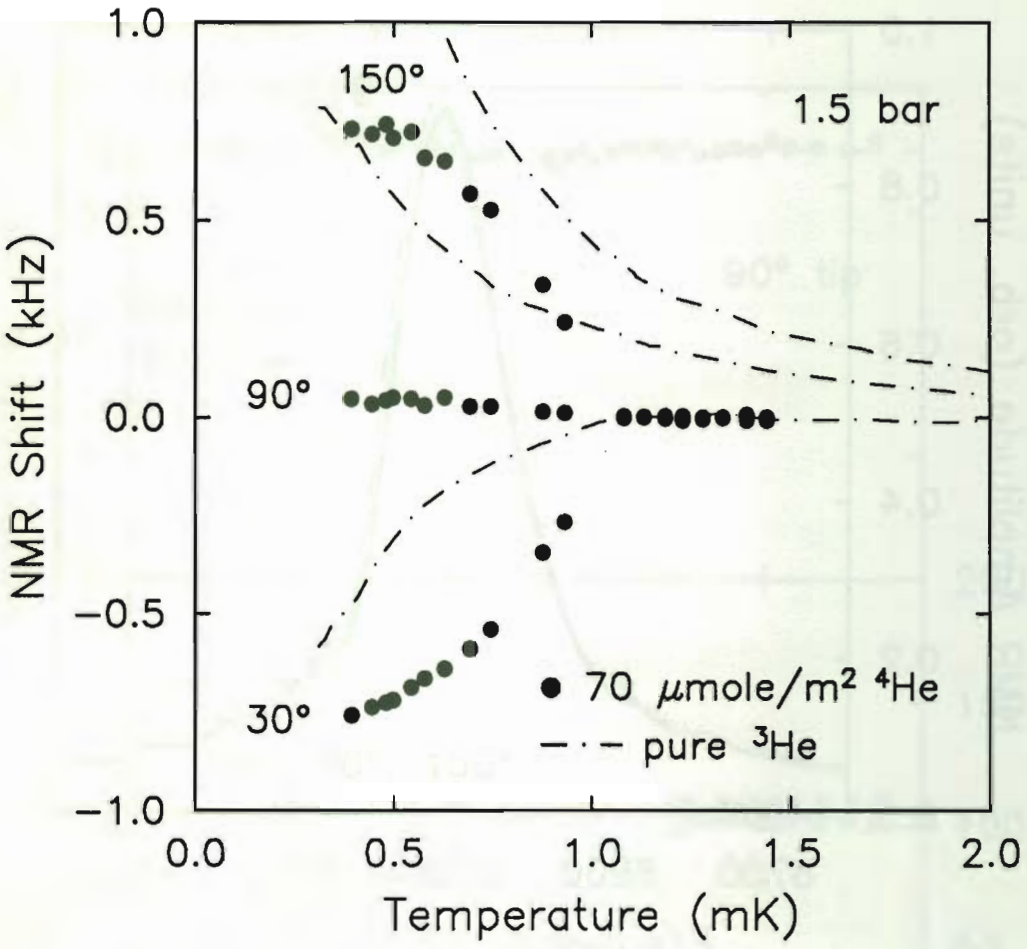

Figure 2.19

^{4}He surface coverage dependence of the raw NMR shift for different tipping angles. The Larmor resonance is at 1 MHz.

non-liquid effects. We are very surprised to discover that removal of the Curie-Weiss magnetization is not the only consequence of ^{4}He pre-plating. In addition, the superfluid order parameter is substantially enhanced, as though the surfaces become more specular for scattering of ^{3}He quasiparticles. This phenomenon, first seen through its

---

magnetic background effects. This makes corrections to pure NMR data more difficult at lower temperatures. The second factor is the apparent geometrical variation in the sample. As the zero temperature correlation length grows, the effect of these variations is felt over a wider range of temperatures below the bulk transition.

effect on measurements of the viscosity of dilute mixtures, is here vividly manifest as a reduction of the pair-breaking efficiency of the wall. The 90 μmole/m^2 ^{4}He coated surface is almost fully specular, if the slope of the bulk NMR shift is correct.

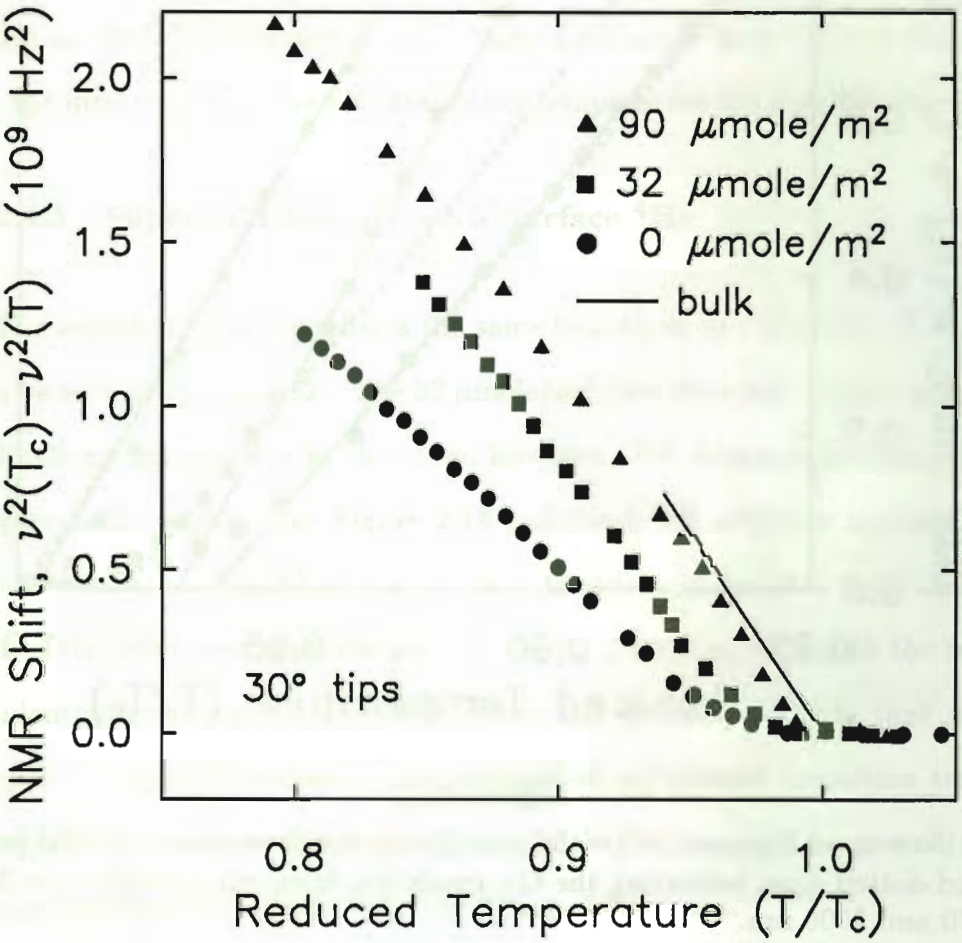

Figure 2.20

The NMR shift for three different boundary conditions, corresponding to 0, 32 and 90 μmole/m^2 ^{4}He coverages. The ^{3}He pressure is 8.5 bar. The ordinate represents the squared Leggett frequency, in the measurement spatially averaged across the width of the film.

From Figure 2.20 it is clear that two monolayers of surface ^{4}He (with no superfluid component) have a large effect on the boundary condition for ^{3}He quasiparticle

effect on measurements of the viscosity of dilute mixtures, is here vividly manifest as a reduction of the pair-breaking efficiency of the wall. The 90 μmole/m^2 ^{4}He coated surface is almost fully specular, if the slope of the bulk NMR shift is correct.

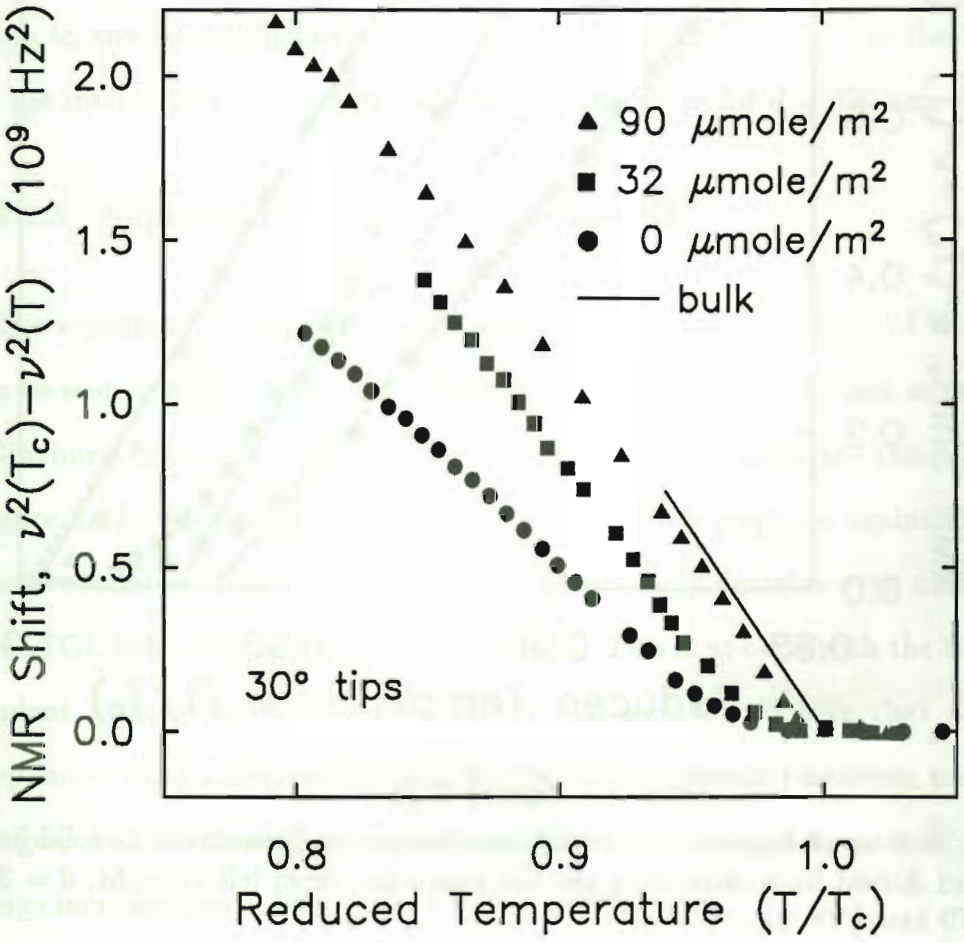

Figure 2.20

The NMR shift for three different boundary conditions, corresponding to 0, 32 and 90 μmole/m^2 ^{4}He coverages. The ^{3}He pressure is 8.5 bar. The ordinate represents the squared Leggett frequency, in the measurement spatially averaged across the width of the film.

From Figure 2.20 it is clear that two monolayers of surface ^{4}He (with no superfluid component) have a large effect on the boundary condition for ^{3}He quasiparticle

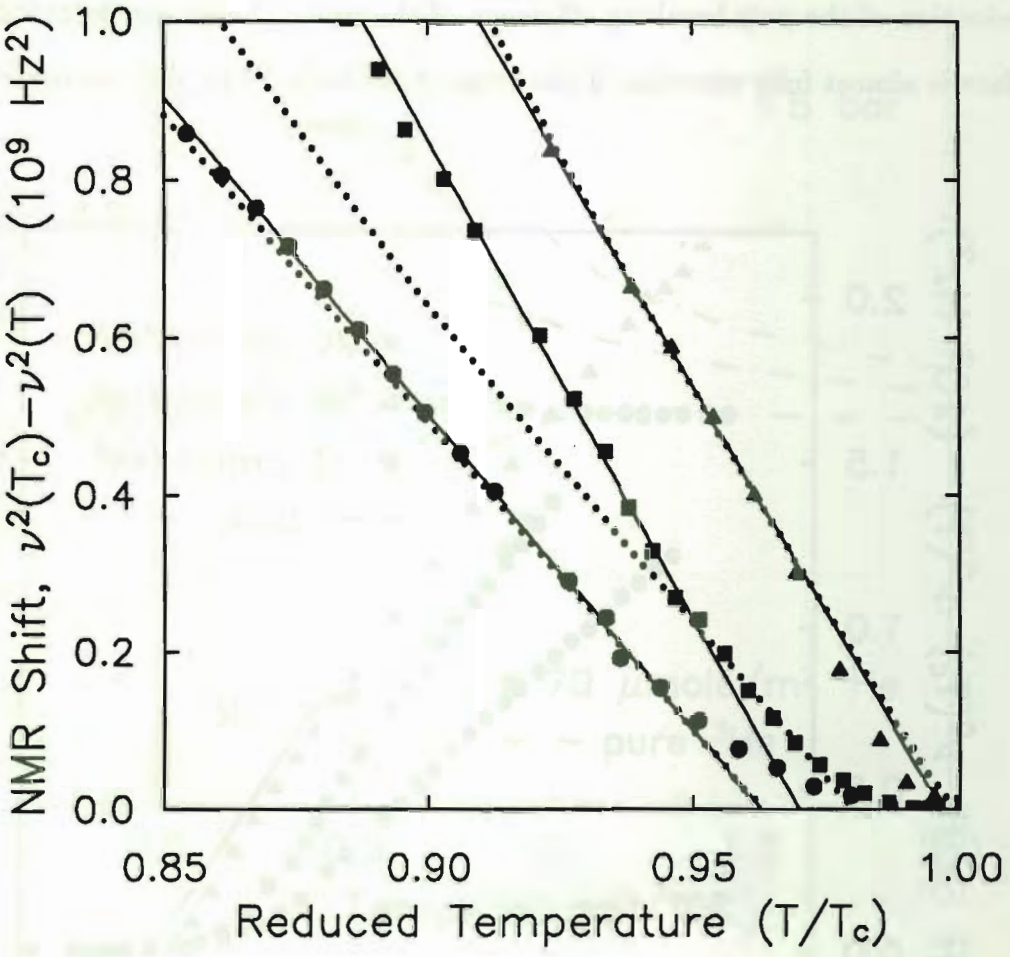

Figure 2.21

A blow-up of Figure 2.20 , with linear fits to the data shown as solid lines, and dotted lines indicating the GL result for, from left to right, $d = 350$, 470 and 2500 nm.

scattering. What is *not* clear is how to describe this effect, even phenomenologically in the context of Ginzburg-Landau theory. We do not expect any temperature dependence of the boundary condition at these low temperatures ($T \ll T_F$). The superfluid density has not yet been calculated within the numerical models which allow the surface roughness to vary[52,56]. We do have a free parameter, the dimensionless thickness in the GL model. Qualitatively, the spatial average of the order parameter in a film with partly specular walls is like that of a thicker, completely diffuse walled film.

Figure 2.21 is a blow-up of Figure 2.20 , showing linear fits to the data as solid lines and the Ginzburg-Landau result for three different film thicknesses as dotted lines. From left to right, the dotted lines correspond to d = 350, 470 and 2500 nm. The 90 μmole/m^2 surface is indeed highly specular, responding like a diffuse walled film an order of magnitude thicker than it actually is. The 32 μmole/m^2 data does not conform to any single thickness. The slope of its linear fit is close to the bulk slope, while the intercept is at the film transition temperature for d = 390 nm.

2.4.3 Superfluid Density with Surface ^{4}He

The superfluid density reflects the same behaviour as a function of ^{4}He coverage, as can be seen in Figure 2.22 . The 32 μmole/m^2 data does not deviate as rapidly from the Ginzburg-Landau line in this case, however. We demonstrate this more clearly in Figure 2.23 , a plot, like Figure 2.15 , of the NMR response against that of the torsional oscillator. The 32 μmole/m^2 data surprisingly deviates even more from the expected GL behaviour than the pure ^{3}He data. This is at odds with the temperature dependent χ-factor model proposed in the last section. Within that picture, the discrepancies should decrease as the interval of suppressed transition temperatures converges, with increasing specularity, on T_c. This trend is recovered as the ^{4}He coverage increases, as indicated by the 90 μmole/m^2 data.

2.4.4 Discussion of the Boundary Condition

What is the nature of the mechanism causing diffusivity, and how is it affected by ^{4}He coverage? The Ginzburg-Landau model treats the order parameter reduction at the wall phenomenologically. It doesn't care by what mechanism that boundary condition is established. It's a fragile characteristic of anisotropic superfluids that this can be done by elastic scattering. The usual assumption for ^{3}He is that the pair

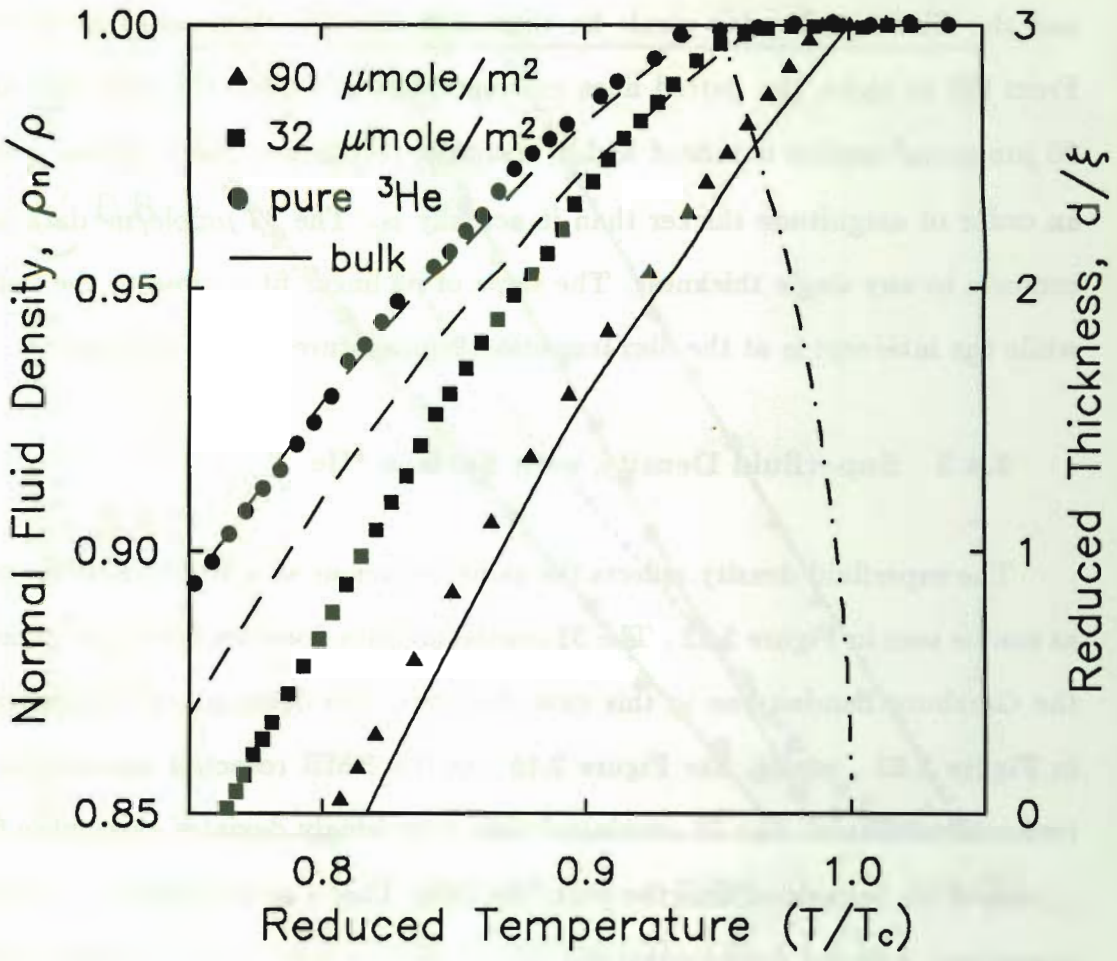

Figure 2.22

The ^{3}He normal fluid density at 8.5 bar, for three different surface coverages of ^{4}He. The two dashed lines are the Ginzburg-Landau results for $d =$ 290 and 360 nm. The dot-dashed line indicates the temperature variation of the dimensionless thickness. Here we have broken the $w = \pi$, but not the $w = 1$, barrier.

breaking is due to elastic quasiparticle scattering from geometrical surface roughness. This assumption seems reasonable, as no experiments have yet been performed on carefully prepared surfaces of known morphology. Roughness on the scale of the quasiparticle wavelength (1 nm) dominates; variations on longer length scales are less efficient at depairing.[52] The correlation length is not special in this regard. The

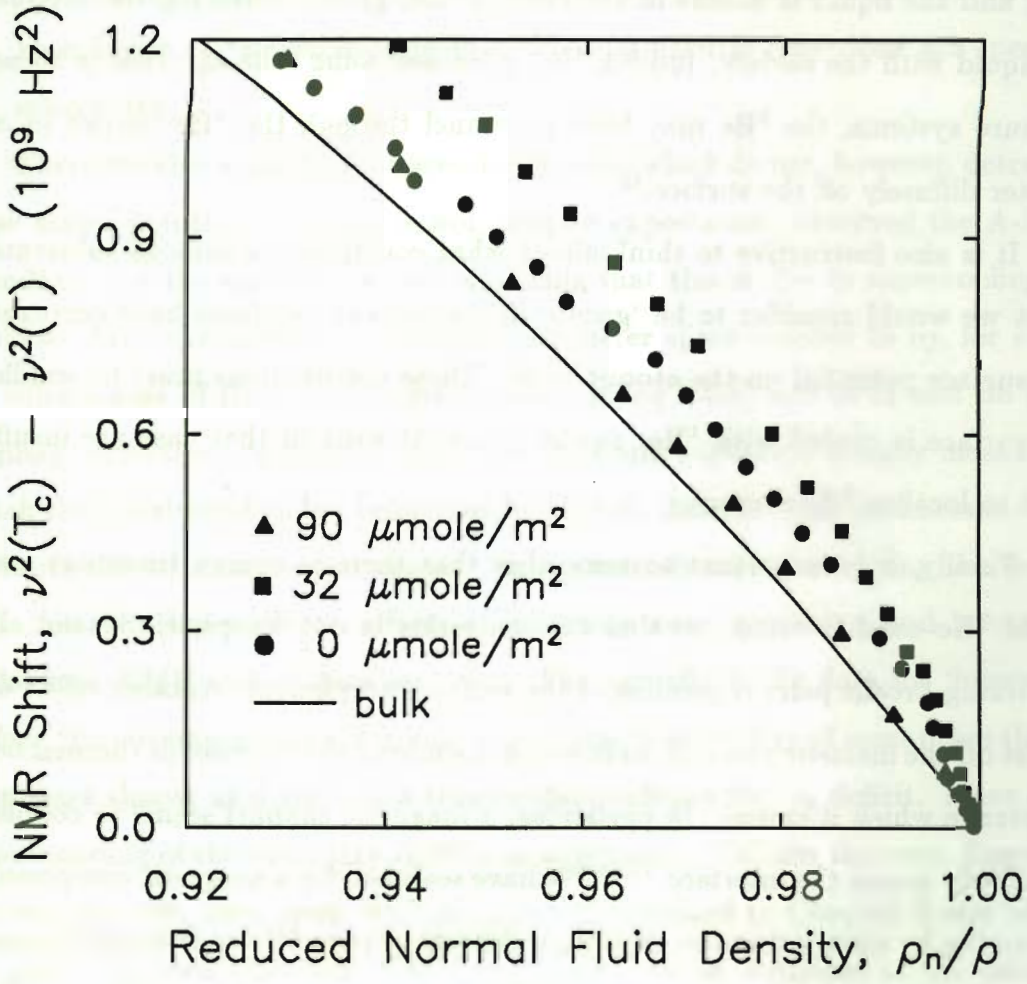

Figure 2.23

The NMR and torsional oscillator responses from Figures 2.20 and 2.22, plotted one against the other as in Figure 2.14 . The 32 μmole/m^2 data shows a surprising increased deviation from the bulk behaviour.

superfluid state is constructed in a self-consistent manner which takes into account how quasiparticles scatter from the wall.

It seems suggestive that the thicknesses of the ^{4}He films which we put down are comparable to the quasiparticle wavelength, and might therefore smooth out roughness on the appropriate scale, especially in the case of multilayer coverages. When coated by solid ^{4}He, however, the surface must be geometrically similar to when it is coated with solid ^{3}He. The key difference is that the exchange process between the

solid and the liquid is absent in the case of ^{4}He, greatly reducing the interaction of the liquid with the surface. Indeed, Hall proposed some time ago that in these dilute mixture systems, the ^{3}He may have to tunnel through the ^{4}He barrier in order to scatter diffusely off the surface.[46]

It is also instructive to think about what constitutes a smooth substrate. Even what we would consider to be 'geometrically smooth' surfaces have corrugations in the surface potential on the atomic scale. These corrugations must be smaller when the surface is coated with ^{4}He, as the potential wells in that case are insufficiently deep to localize ^{3}He atoms.

Finally, it is important to remember that there is energy transport across the liquid ^{3}He–solid interface, so that the scattering is not completely elastic. Inelastic scattering breaks pairs regardless of the surface morphology. Another effect of ^{4}He is to cut off the inelastic channel, as is well-known from the increase in thermal boundary resistance which it causes. In particular, a magnetic channel seems to couple energy effectively across the interface.[50,14] We have searched for a magnetic component of the scattering by monitoring the superfluid density of pure ^{3}He at constant temperature, while changing the surface polarization by sweeping the magnetic field. The result was null (as Emil Polturak points out, saying 'searched for' means you didn't find it).

The complete answer must explain both momentum and energy transfer at the interface. We consider this problem further in Chapter 3.

2.5 Conclusions

We have carried out a quantitative examination of the behaviour of superfluid ^{3}He when confined to a film of thickness comparable to the correlation length of the order parameter. The central conclusions are as follows:

I. Our results for pure ^{3}He exhibit generally good agreement with the Ginzburg-Landau theory, assuming that the order parameter vanishes at the surfaces.

II. The superfluid response is nearly bulk-like when the surfaces are coated with five monolayers of ^{4}He, indicating that the quasiparticle reflections are specular, or mirror-like.

There are also a number of unresolved issues, which do not, however, detract from these major points. i.) We have not, despite expectation, observed the A-B phase boundary. For the moment, we are assuming that this is due to supercooling of the A phase. We have overlapped parts of parameter space pointed to by, for example, the calculations of Hara and Nagai (weak-coupling limit) and of Li and Ho (strong-coupling corrections of Bedell). ii.) The NMR and superfluid density measurements match the Ginzburg-Landau behaviour for slightly different film thicknesses. We may attribute this to a number of causes – errors introduced in correcting the frequency shifts for solid layer effects; effects of inhomogeneous geometry; and inconsistency of the bulk NMR and ρ_s data sets. iii.) The superfluid ^{3}He data for 'intermediate' surface ^{4}He coverages does not mimic a Ginzburg-Landau film of some other thickness. It appears almost as if there is a temperature-independent ρ_s deficit. More detailed understanding of the boundary conditions is needed to explain this one. Experiments can lead the way here, with work of the type described in Chapter 3 also playing a big part. We need more information before we can be confident of the microscopic origin of the diffusive boundary condition.

The experiments are not yet at the level of being able to resolve the small quantitative corrections to the superfluid density introduced by Thuneberg. Two (comparable) impediments are the geometry characterization and the bulk data in the transition region. A more likely next step is a comparison with numerical results (using the quasiclassical boundary condition) in the low T/T_c regime. The work could also proceed naturally to cylindrical channels, to nail down the polar phase with NMR, and to look for the various other phases predicted by Barton and Moore.

In my opinion the most interesting path to follow from here goes off in the direction of two-dimensional superfluidity, and the possibilities for Kosterlitz-Thouless transitions in ^{3}He films. The present results have not probed the $d < \xi$ regime, but have demonstrated great promise for accessing it.

References for Chapter 2

2.1 M.R. Freeman, R.S. Germain, E.V. Thuneberg and R.C. Richardson, Phys. Rev. Lett. **60**, 596 (1988); M.R. Freeman, R.S. Germain, L. Opsahl, E. Houseman and R.C. Richardson, Jpn. J. Appl. Phys. Supplement **26-3**, 121 (1987).

2.2 American Magnetics Corp., Oak Ridge, TN.

2.3 D.S. Greywall, Phys. Rev. **B33**, 7520 (1986).

2.4 W.P. Halperin, F.B. Rasmussen, C.N. Archie and R.C. Richardson, J. Low Temp. Phys. **31**, 617 (1978).

2.5 J.D. Reppy, in *Proc. ULT Hakoné Symposium 1977*, p. 89.

2.6 Emerson and Cumming Corp., Canton MA.

2.7 Dupont Polymer Products Division, Wilmington, Delaware.

2.8 Duke Scientific Corp., Palo Alto CA.

2.9 P.W. Adams and W.I. Glaberson, Phys. Rev. **B35**, 4633 (1987).

2.10 A.L. Fetter and S. Ullah, J. Low Temp. Phys. **70**, 515 (1988).

2.11 A.I. Ahonen, M. Krusius and M.A. Paalanen, ibid. **25**, 421 (1976).

2.12 T.J. Gramila, Ph.D. Thesis, Cornell University (forthcoming).

2.13 A.I. Ahonen, T. Kodama, M. Krusius, M.A. Paalanen, R.C. Richardson, W. Schoepe and Y. Takano, J. Phys C. **9**, 1665 (1976).

2.14 P.C. Hammel, Ph.D. Thesis, Cornell University (1983).

2.15 H. Godfrin, R.R. Ruel and D.D. Osheroff, Phys. Rev. Lett. **60**, 305 (1988).

2.16 H. Ramm, P. Pedroni, J.R. Thompson and H. Meyer, J. Low Temp. Phys. **2**, 539 (1970).

2.17 H. Godfrin, G. Frossati, D. Thoulouze, M. Chapellier and W.G. Clark, J. Phys. (Paris) Colloq. **39**, C6-287 (1978).

2.18 A. Schuhl, S. Maegawa, M.W. Meisel and M. Chapellier, Phys. Rev. **B36**, 6811 (1987).

2.19 Y. Okuda, A.J. Ikushima and H. Kojima, Phys. Rev. Lett. **54**, 130 (1985).

2.20 H.M. Bozler, M.E.R. Bernier, W.J. Gully, R.C. Richardson and D.M. Lee, Phys. Rev. Lett. **32**, 875 (1974).

2.21 J.D. Jackson, *Classical Electromagnetism,* Wiley and Sons, New York (1975).

2.22 H.M. Bozler, D.M. Bate and A.L. Thomson, Phys. Rev. **B27**, 6992 (1983).

2.23 E.L. Hahn and D.E. Maxwell, Phys. Rev. **88**, 1070 (1952).

2.24 A.J. Leggett, Rev. Mod. Phys. **47**, 331 (1975).

2.25 V. Ambegaokar, P.G. de Gennes and D. Rainer, Phys. Rev **A9**, 2676 (1974).

2.26 S. Takagi, J. Phys C **8**, 1507 (1975).

2.27 A.J. Leggett, Ann. Phys. (N.Y.) **85**, 11 (1974).

2.28 D.D. Osheroff and L.R. Corruccini, Phys. Lett. **51A**, 447 (1975); W.F. Brinkman and H. Smith, *ibid.*, p. 449.

2.29 E.V. Thuneberg, private communication.

2.30 D.N. Paulson, H. Kojima and J.C. Wheatley, Phys. Rev. Lett. **32**, 1098 (1974).

2.31 R.F. Berg, B.N. Engel and G.G. Ihas, in *LT-17 Proceedings,* p. 1171 (1984).

2.32 J. Wilks, *The Properties of Liquid and Solid Helium,* Oxford U.P., Oxford (1967).

2.33 T.J. Gramila, private communication.

2.34 G. Agnolet, Ph.D. Thesis, Cornell University (1983).

2.35 L.D. Landau and E.M. Lifshitz, *Fluid Mechanics,* Pergamon, Oxford (1984).

2.36 L.V. Kiknadze and Yu. G. Mamaladze, Sov. J. Low Temp. Phys. **1**, 106 (1975).

2.37 T.C. Padmore and J.D. Reppy, Phys. Rev. Lett **33**, 1410 (1974).

2.38 A.L. Fetter, private communication; Y.-H. Li and T.-L. Ho, preprint.

2.39 L.J. Buchholtz and A.L. Fetter, Phys. Rev. **B15**, 5225 (1977).

2.40 D. Einzel, J. Low Temp. Phys. **54**, 427 (1984).

2.41 J.E. Berthold, R.W. Giannetta, E.N. Smith and J.D. Reppy, Phys. Rev. Lett. **37**, 1138 (1976).

2.42 J.M. Parpia, D.G. Wildes, J. Saunders, E.K. Zeise, J.D. Reppy and R.C. Richardson, J. Low Temp. Phys. **61**, 337 (1985).

2.43 J.A. Sauls and J.W. Serene, Phys. Rev. **B24**, 183 (1981). Strong coupling coefficients calculated more recently by Bedell are tabulated in Li and Ho, preprint (1988).

2.44 K. Ichikawa, S. Yamasaki, H. Akimoto, T. Kodama, T. Shigi and H. Kojima, Phys. Rev. Lett **58**, 1949 (1987).

2.45 J.R.G. Keyston and J.P. Laheurte, Phys. Lett. **24A**, 132 (1967).

2.46 H.E. Hall, in *Liquid and Solid Helium*, C.G. Kuper *et al.*, ed.s, Wiley, New York (1975).

2.47 D.A. Ritchie, J. Saunders and D.F. Brewer, Phys. Rev. Lett. **59**, 465 (1987).

2.48 W.C. Black, A.C. Mota, J.C. Wheatley, J.H. Bishop and P.M. Brewster, J. Low Temp. Phys. **4**, 391 (1971).

2.49 D.J. Bishop and J.D. Reppy, Phys. Rev. **B22**, 5171 (1980).

2.50 L.J. Friedman, Ph.D. Thesis, Cornell University (1982).

2.51 B.R. Johnson, Ph.D. Thesis, Cornell University (1984).

2.52 L.J. Buchholtz, Phys. Rev. **B33**, 1579 (1985).

2.53 D.S. Betts, D.F. Brewer and R. Lucking, in *LT-13 Proceedings*, p. 559 (1972).

2.54 J.P. Harrison, private communication.

2.55 D.F. McQueeney, G. Agnolet and J.D. Reppy, Phys. Rev. Lett. **52**, 1325 (1984).

2.56 W. Zhang, J. Kurkijärvi and E.V. Thuneberg, Phys. Rev. **B36**, 1987 (1987).

Chapter 3

Higher Temperature Results

From now on ... I'm runnin' this place.

Rudy Ray Moore

In the preceding Chapter, we found that a ^{4}He boundary layer substantially increases the probability for specular scattering of ^{3}He quasiparticles at a mylar surface. The conclusion is based on measurements of the spatially averaged amplitude of the superfluid order parameter. In retrospect, this surprising effect might have been predicted based upon rather extensive work[1-3] on the effective viscosity of dilute mixtures of ^{4}He in ^{3}He. A qualitative interpretation of the latter results points to a specularity of order 99 % for scattering of ^{3}He quasiparticles at superfluid ^{4}He film covered surfaces. Somehow this fact had never arisen in the context of superfluid ^{3}He boundary conditions, for which the prevailing assumption had been that only through the most careful surface preparation would pair breaking at a wall ever be reduced. We shall now discuss our preliminary investigations of this other measure of the boundary condition, the friction between the substrate and the fluid in the normal phase.

The prospect of correlating the superfluid amplitude near a wall with the boundary condition for hydrodynamic flow of the normal liquid has a strong appeal. Two interesting new features have been observed and are described in this Chapter – a sudden change of the boundary condition at a transition (probably superfluid) of the ^{4}He film, and the persistence of this transition above the bulk solidification pressure. Our cell was not designed to be sensitive to normal phase slip effects, but through an

accident of imperfect construction we have been able to glean qualitative information. It turns out that we can measure the slip of fluid in the roughly 10 μm gap between the mylar stack and the wall of the epoxy capsule.

The normal phase measurements begin in conjunction with the Kosterlitz-Thouless calibrations of the ^{4}He coverage. We find to our surprise that when the ^{4}He layer is completely submerged by ^{3}He, an abrupt change in the boundary condition seems to swamp the familiar KT signature (a peak in the dissipation and period drop) with effects of ^{3}He slip. John Reppy and Dave McQueeney pointed out that it would be interesting to follow the evolution of the ^{4}He film under pressure. With the ^{3}He slip technique we accept an indirect probe of the ^{4}He film in exchange for an amplified response. In this cell the actual Kosterlitz-Thouless signal at 200 mK is at our limit of resolution, as the mylar surface area (0.2 m^2) and the oscillator Q (50,000) both are relatively low. In comparison, the geometric area probed by slip in this case is only 2.5 cm^2.

As the $T \rightarrow 0$ melting curve of ^{3}He lies 9 bar above that of ^{4}He, this system has unique possibilities for the study of surface freezing. The results complement other measurements, such as those of the surface tension of bulk solid ^{4}He[4], of the melting curve in porous materials[5], and of fourth sound in a Grafoil superleak[6].

3.1 Characterization of the Geometry

The viscosity, $\eta = \frac{1}{5} n p_F l$, of the normal ^{3}He Fermi liquid (NFL) varies as the inverse square of the temperature. n is the number density of particles, p_F is the Fermi momentum and l is the mean free path. In hydrodynamics, the viscous penetration depth, $\delta = \sqrt{2\eta/\rho\omega}$, characterizes the response of a fluid to transverse oscillatory motion of a surface on which it lies. ρ is the density of the fluid and ω the angular velocity of the motion. δ for the Fermi liquid is sensibly the distance a quasiparticle diffuses in the time $1/\omega$. If the thickness, d, of the fluid layer is small in comparison

to δ, then the motion if the liquid is nearly uniform and in concert with that of the substrate. In this limit, the damping of a torsional oscillator is given by[7]

$$Q^{-1} = Q_o^{-1} + \frac{1}{6}\frac{I_f}{I_b}\left(\frac{d}{\delta}\right)^2, \tag{3.1}$$

where I_f, I_b respectively are the moments of inertia of the fluid and of the complete pendulum bob, and Q_o^{-1} represents the dissipation of the unloaded oscillator. $Q^{-1} - Q_o^{-1}$ is proportional to the square of the temperature in the NFL regime.

In Figure 3.1 , we plot Q^{-1} of the oscillator below 250 mK. At each point the temperature of the mixing chamber is regulated and the cell allowed to equilibrate. The maximum thermal time constant for cooling the helium through the torsion rod is 2 hours, at 100 mK. At that temperature, the time constant for equilibration within the head of the oscillator is 90 seconds. The extra damping due to the ^{3}He varies approximately as T^2 below 60 mK. To our knowledge the bulk viscosity of ^{3}He at elevated pressures has not been measured. At saturated vapor pressure, η drops much more slowly than $1/T^2$ above 100 mK. The temperature demarcating the limit of NFL behaviour should fall with increasing pressure. In later data analysis we use values of the viscosity (and hence of the penetration depth and the mean free path) at high temperatures determined by calculating a 60 mK point[8] and extrapolating on the basis of the measured dissipation. Note the crossover of the empty and full cell dissipations, indicating that thermal contact to the empty cell is lost below 10 mK.

The measured slope dQ^{-1}/dT^2 establishes that the dissipation is not occurring in the ^{3}He confined between the mylar sheets. Taking $\delta = 535/T^2$ μm·mK^2 (the oscillator frequency is 1750 Hz) and $d = 300$ nm we calculate a slope equal to one-sixtieth of what is observed. Because the energy loss depends on the square of the thickness, a small amount of helium in a wider opening can easily dominate the dissipation. As already mentioned, the explanation in this case is a peripheral void between the mylar and the epoxy. The experimental slope suggests that a fraction f

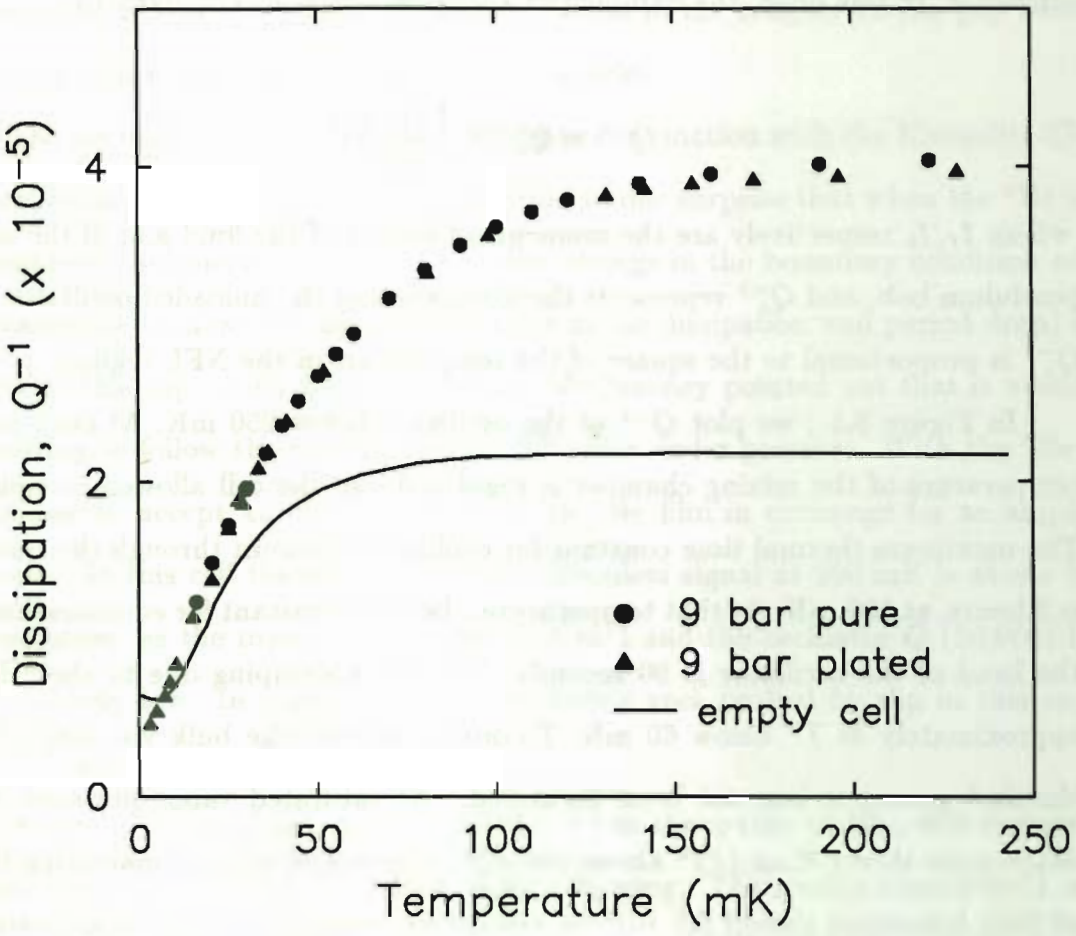

Figure 3.1

The dissipation of the oscillator. The excess damping due to the helium arises from the slight decoupling of fluid as the viscous penetration depth drops with increasing temperature. The two 9 bar data sets are from different cool-downs, and 'plated' of course refers to a surface layer of ^{4}He.

of the fluid moment of inertia occupies a region of approximate thickness $\sqrt{60/f} \cdot 300$ nm. Our estimate of f is guided by the period shift of the oscillator in the normal phase.

The standard analysis[7] of the hydrodynamic response of a torsional oscillator (for a fluid sample of uniform thickness and neglecting edge effects – that is, the liquid is assumed thin in comparison to its lateral extent) yields for Q^{-1} and the resonant

period, P,

$$Q^{-1} = \frac{I_f}{I_b}\frac{1}{x}\frac{\sin x - \sinh x}{\cos x + \cosh x} \tag{3.2}$$

and

$$P = (P_f - P_o)\frac{1}{x}\frac{\sin x + \sinh x}{\cos x + \cosh x}. \tag{3.3}$$

Here $x = d/\delta$, P_f is the period with the fluid completely entrained, P_o corresponds to full fluid decoupling, and we have assumed that $P_f - P_o \ll P_o$. $I_f/I_b = 2(P_f - P_o)/P_o$. At large x, most of the liquid is decoupled so the dissipation is small and $P \approx P_o$. As $x \to 0$, the fluid locks up and $P \to P_l, Q^{-1} \propto x^2$. The dissipation peaks when the greatest mass of fluid is moving out of phase with the substrate, at $x \approx 2$. The haystack-shaped plot of Q^{-1} vs. P for the entire range of x can be used to determine the total period shift, $P_f - P_o$ and, if the viscosity is known, the thickness, d.

Figure 3.2 shows the dissipation change plotted against the period shift after subtraction of the empty cell backgrounds. The pure ^{3}He data should be viewed as less reliable, as they were taken during a separate cooldown for which we do not have an independent background. The shapes of the experimental curves are affected by the nonuniformity of the geometry. The two small circles near the origin span the entire range of variation between 0 and 250 mK due to all of the 300 nm films. The solid line is the hydrodynamic result over the range $x = (0, 5)$ for a slab having a fraction $f = 0.06$ of the helium moment of inertia, or 16 nsec out of a total shift of 256 nsec on filling to this pressure. Referring back to the temperature dependence of the dissipation, this corresponds to a thickness of 9.5 μ. At the same time, we estimate the penetration depth at 250 mK to be $\delta \sim 6.5\mu$m. The open square on the haystack in Figure 3.2 marks the position at which $x = 1.5$, and hence $d \sim 9.8\mu$m. The analysis therefore appears to be self-consistent. Note that a 10 μm thick cylindrical shell around the *entire* mylar stack would contribute a 21 nsec period shift.

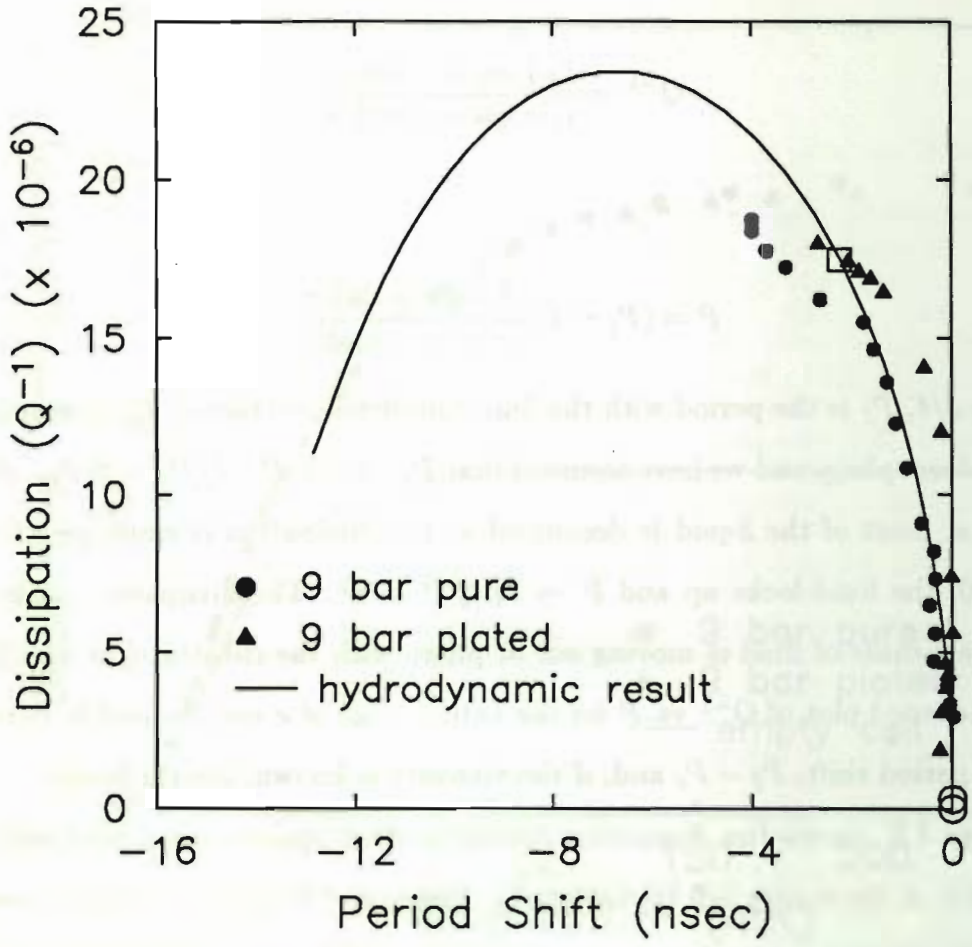

Figure 3.2

The solid symbols are the dissipation data of Figure 3.1, plotted against the oscillator period shift. The origin here corresponds to complete locking of the fluid at low temperatures. The data are compared with the hydrodynamic response of a thin slab, for an approximate identification of the roguish moment of inertia. The solid line represents an amount of ^{3}He contributing a 16 nsec period shift. The open square marks the position on that curve for $d = 10$ μm at 200 mK. The open circles near the origin span the range $T = 0 \rightarrow 250$ mK for the *entire stack* of 300 nm films.

3.2 Slip Effects at the ^{4}He Film Transition

Now that we have an idea of the identity of the helium sample to which the oscillator is sensitive in the normal phase, we can discuss the consequences of changing

the boundary condition with ^{4}He. For the degenerate ^{3}He Fermi fluid, the mean free path and collision time, respectively, have typical values $l = (50/T^2)\mu\text{m} \cdot \text{mK}^2, \tau = (1/T^2)\mu\text{sec} \cdot \text{mK}^2$. It is easy to violate, in an experiment, either of the assumptions of hydrodynamics, $\omega\tau \ll 1$ and $l \ll d$, where ω is the frequency and d is a characteristic size of the system. 'Slip theory' extends the range of applicability of the hydrodynamic description by correcting the boundary conditions to first order in l/d. The usual boundary condition has the relative velocity of the fluid and the boundary vanishing at the surface. Hydrodynamics does not describe the flow at distances less than l from a wall, however, just as Ginzburg-Landau theory cannot describe an order parameter over distances less than ξ. For fluid flow next to a wall the velocity profile extrapolates to zero at a distance ζ behind the wall, known as the slip length. This idea first arose in the study of rarefied gas flow in 1875[9]. In the Fermi liquid, $\zeta \sim 0.6l$. Qualitatively the effect of slip may be pictured as moving the boundaries back a distance ζ and retaining the hydrodynamic boundary condition. Beyond the slip regime, the transport is typically found starting from a Boltzmann equation. These effects are discussed in detail for quantum fluids by Jensen *et al.* [10] and by Einzel *et al.* [11]. Introductory discussions are given by Smith[12] and by Jaffe[13].

The slip correction may be incorporated into the hydrodynamic result by replacing the viscosity by an effective value[9]

$$\frac{1}{\eta_{\text{eff}}} = \frac{1}{\eta_{\text{bulk}}}\left(1 + 6\frac{\zeta}{d}\right). \tag{3.4}$$

In the calculation of the dissipation in the well-locked regime, it is convenient to retain the bulk penetration depth and replace the thickness by the effective value, $d_{\text{eff}} = d + 3\zeta$.

To this point we have implicitly assumed that particles are diffusively scattered at the surface. Non-specular reflection underlies the conventional hydrodynamic boundary condition. For flow next to a fully specular surface, the velocity profile approaches

the wall with zero slope (no transverse momentum is exchanged). In that case, if one were to define a slip length it would be infinite. Partial specularity is included by multiplying the diffuse slip length by the factor[10] $(1+s)/(1-s)$, where s is the probability that a single scattering event is specular. The slip model with a temperature independent specularity factor is known to inadequately describe the low temperature effective viscosity of dilute mixtures[3], but we nevertheless couch our analysis in these terms, for lack of a better framework.

The importance of the boundary condition is vividly demonstrated by Figure 3.3 . Here we compare the signature of the transition in a 90 μmole/m^2 ^{4}He film completely submerged by ^{3}He with that of a (much thinner) 32 μmole/m^2 bare ^{4}He film at a similar temperature. The temperature dependent backgrounds of the oscillator (and of pure ^{3}He for the mixture data) have been subtracted off. From the Kosterlitz-Thouless theory (and the experimental results of McQueeney, Agnolet and Reppy[14]) we expect the ^{4}He signal to scale approximately with the temperature. The large response when the ^{3}He is present can be understood as a sudden decrease (on cooling) of the *effective* viscosity of the ^{3}He. The solubility of ^{4}He drops exponentially in this regime and is negligible below approximately 200 mK, so the actual viscosity of the fluid may be changing as the ^{4}He comes out of solution. We rule this out as a substantial effect because we find similar transitions at temperatures as low as 75 mK. Solution effects are considered further in Sec. 3.3. We conclude that it is the frictional force between the ^{3}He and the surface which changes.

When the dissipation change and period shift of Figure 3.3 are plotted against one another, the slope matches the hydrodynamic curve at the point corresponding $x = 1.7$, or an 11 μm thickness. Our crude approximation of the geometry again appears to be reasonable. From the amplitude of the period and dissipation shift we can produce a number which describes the specularity of the superfluid ^{4}He surface for temperatures near 200 mK. When $\zeta(1+s)/(1-s) \ll d$ we have

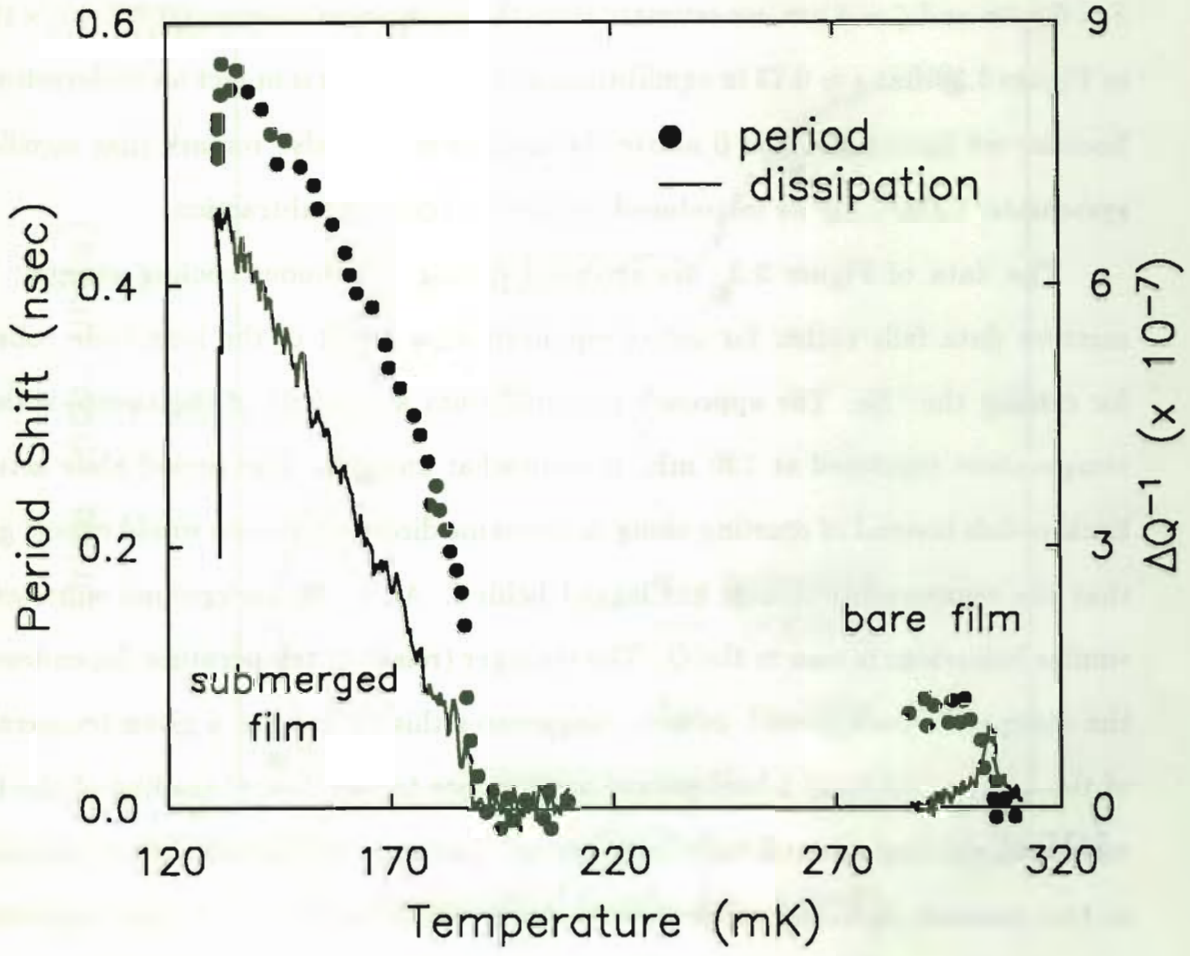

Figure 3.3

The excess dissipation and period change of the cell resulting from a transition in the 90 μmole/m^2 ^{4}He film. The dominance of ^{3}He slip is apparent by comparison with the Kosterlitz-Thouless transition of a bare 32 μmole/m^2 ^{4}He film, shown on the same scale.

$$Q^{-1} = \frac{1}{3}\frac{P_l - P_0}{P_0}\frac{1}{\delta^2}\left(d + 3\zeta\left(\frac{1+s}{1-s}\right)\right)^2. \tag{3.5}$$

The component due to specularity is therefore

$$\Delta Q^{-1}(s) \equiv Q^{-1}(s) - Q^{-1}(s=0) = \frac{P_l - P_0}{P_0}\frac{\zeta}{d}\left(\frac{d}{\delta}\right)^2\left(\frac{4s}{1-s}\right). \tag{3.6}$$

$\delta \propto \sqrt{\zeta}$ in the Fermi liquid, so this quantity is temperature independent. Taking $\delta = 6.5\mu$m and $\zeta = 4$ nm, we estimate from the dissipation change ($\Delta Q^{-1} \approx 3 \times 10^{-7}$) in Figure 3.3 that $s \approx 0.73$ in equilibrium at 130 mK. This is in fact an underestimate, because we have taken $s = 0$ above the transition. We also remark that significant systematic errors may be introduced by the background subtraction.

The data of Figure 3.3 are recorded during continuous cooling sweeps. The mixture data falls rather far out of equilibrium, a result of the long time constant for cooling the ^{3}He. The approach to equilibrium at the end of the sweep, with the temperature regulated at 130 mK, is somewhat unusual. The period shift actually back-pedals instead of coasting along in the same direction, as one would expect given that the temperature change has lagged behind. After the background subtraction, similar behaviour is seen in the Q. The stronger (relative) temperature dependence of the dissipation background, in fact, exaggerates this effect. For a given temperature of the cell, we subtract a background appropriate to the (lower) reading of the thermometer, yielding an artificially large excess. The apparent period shift is diminished in this manner, however, so there is no danger of the entire effect being an artifact. We propose that this unusual relaxation is a thermomechanical effect, a consequence of the superfluid film thickness in the pendulum bob changing in response to a temperature gradient. It is well known that a superfluid ^{4}He boundary layer will flow away to a free surface at a higher temperature[15]. It would be interesting to design into a future cell the capability of controlling this flow.

Since the temperature remains nearly uniform within the pendulum bob, we obtain some measure of non-equilibrium effects *other* than thermometry problems from hysteresis in the dissipation vs. period plot. An example is shown in Figure 3.4. The symbols are measured during one of the sweeps in which the temperature is regulated at discrete values. The line is from a subsequent continuous cooling trace (of 15,000 sec duration). The temperature span is 130 mK to 280 mK; backgrounds

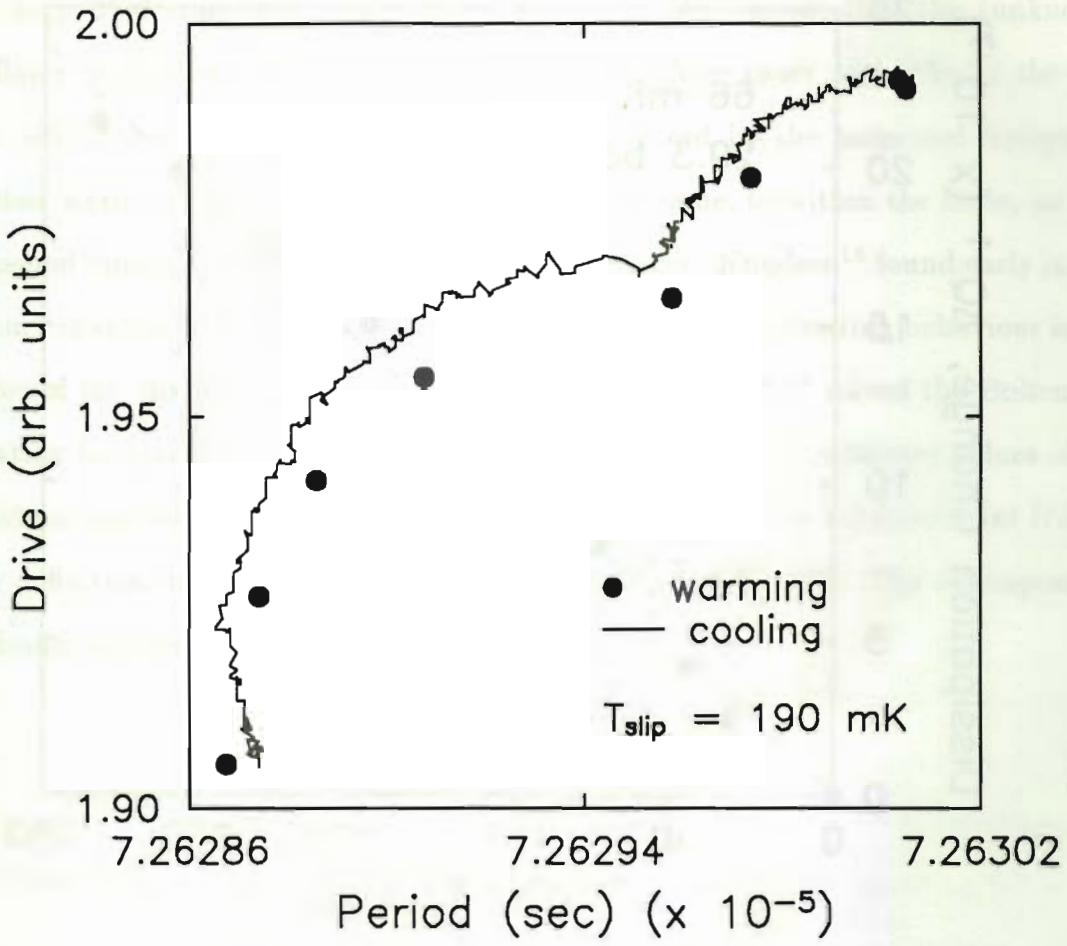

Figure 3.4

Raw oscillator drive vs. period between 130 mK and 280 mK, with a transition at 190 mK. The warming points are taken after equilibration with the thermometers on the stage. The cooling sweep is continuous, but the drive and period should nonetheless remain in equilibrium with each other. The hysteresis reflects thermal gradients to the stage and possibly film flow effects.

have not been subtracted. The transition appears as a cusp. The hysteresis is small compared to what we would call the 'equilibrium' effect. That the dissipation is larger during cooling could again be interpreted as evidence for the film thickness changing in response to a thermal gradient.

At lower temperatures, the search for equilibrium becomes a more tenuous propo-

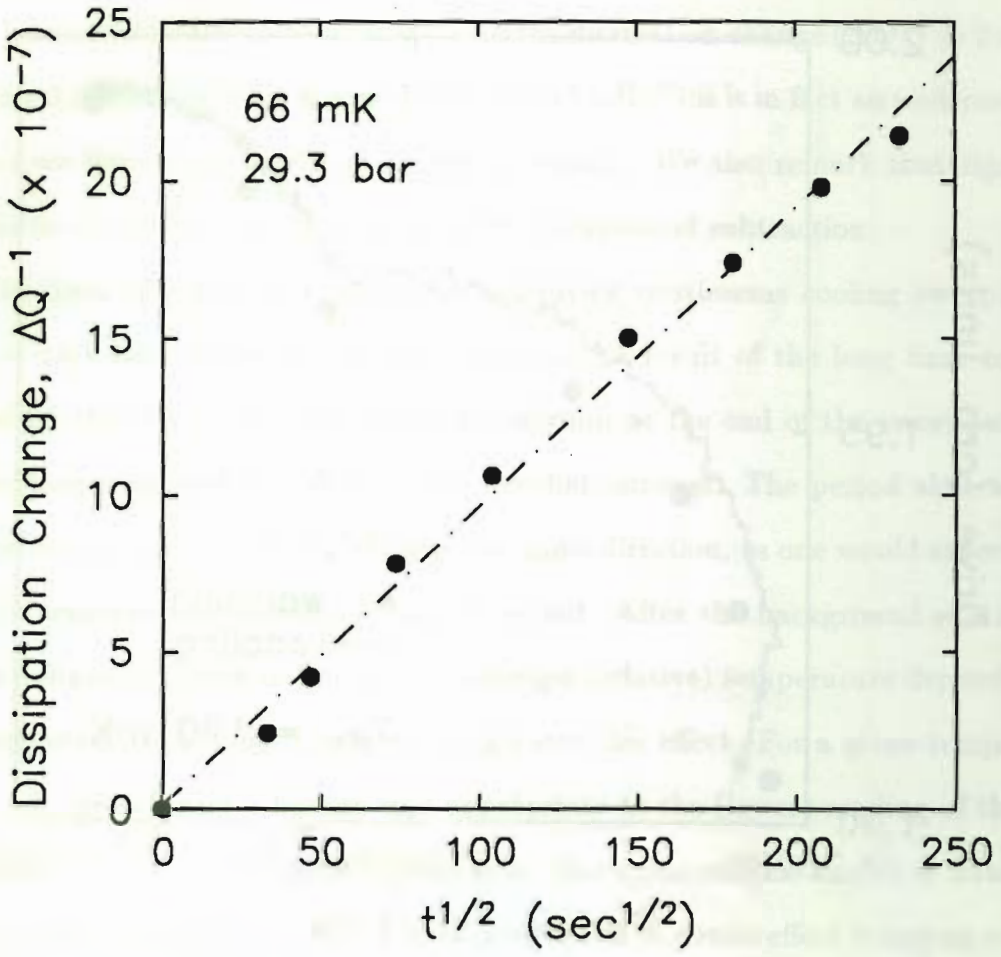

Figure 3.5

Slowly decreasing friction between the ^{3}He and the substrate observed just below a low temperature transition. The temperature equilibrates in a time much shorter than spanned here.

sition. The result of cooling just below the transition, regulating the stage temperature and simply waiting, is shown in Figure 3.5 . The dissipation change onsets abruptly, at which point we define the zero of time. The figure spans 17 hours, a time much greater than required for thermal equilibration. The temperature dependence is suggestive of diffusion, but more measurements are required before this behaviour can be understood.

We can estimate the specularity also from the boundary-dependent Q near the ^{3}He superfluid transition, shown in Figure 3.6 . We assume that the (unknown) oscillator background is the same in each of the three cases with ^{3}He in the cell. The oscillator is in thermal equilibrium, as evidenced by the measured dissipation on slow warming through the transition being the same, to within the noise, as that measured during the demagnetization two days earlier. Knudsen[16] found early in this century that the slip theory breaks down for $d \sim l$, when the limiting behaviour in the center of the channel is no longer hydrodynamic flow. Jaffe[13] solved the Boltzmann equation for plane Poiseuille flow of a normal Fermi liquid at arbitrary values of the Knudsen number, l/d. In the theory, the effective viscosity has a minimum at $l/d = 2$ (the definition of the Knudsen number is inverted in Ref. 13). The corresponding minimum dissipation yields, for diffuse surfaces,

$$Q_{min}^{-1} \approx 3.5 \frac{P_l - P_0}{P_0} \left(\frac{d}{\delta}\right)^2, \tag{3.7}$$

and the change with specularity may be written

$$\Delta Q^{-1}(s) \approx 1.2 \frac{s}{1-s} Q_{min}^{-1}. \tag{3.8}$$

Experiment[17] finds the minimum at a slightly smaller Knudsen number, but the minimum dissipation agrees more closely with theory. With $l = 45/T^2$ μm $\cdot$ mK^2 at 9 bar, the theoretical Knudsen minimum would occur at 1.5 mK. As we are unable to cool the empty cell this far to measure the background dissipation, we must calculate Q_{min}^{-1}, and find 9×10^{-8}. From the damping with 90 μmole/m^2 of ^{4}He on the surface, then, s is estimated to equal 0.91. This is substantially larger than the high temperature estimate. Unfortunately, we do not yet have a theory with which to predict the specularity from the strength of the superfluid ^{3}He order parameter (which in this cell probes a different set of surfaces anyway). The approximately constant

offset of the curves in Figure 3.6 is consistent with the slip description, for which the excess damping is independent of the mean free path (if the specularity does not change). It should be noted, however, that we do not obtain a sensible estimate of Q_{min}^{-1} from the increased dissipation in the superfluid state for pure ^{3}He. Based upon the results of Jaffe and the calculated mean free path, we expect a 30 % increase in the *helium* dissipation due to the precipitous drop by a factor of 5 of the viscosity below the superfluid transition. We observe a 50 % increase of the *total* dissipation. Evidently, the Q below T_c does not admit of such a simple description. Additionally it displays some structure that implies further complication. Note that the abrupt increase onsets at the *bulk* transition temperature in the 10 μm geometry. This is an invaluable asset to thermometry for the work of Chapter 2.

The observation of a sharp transition in the normal phase prompts us to speculate anew about the microscopic details which may determine the boundary condition. Kennard's statement of 50 years ago still applies in this context: "If we knew more about the interaction of gas molecules with solid and liquid surfaces, it might be logical to begin with a study of the laws of this interaction."[9]. In ^{3}He, quasiparticle scattering characteristics determine both the amplitude of the superfluid order parameter and the flow resistance of the normal fluid in these confined systems. In practice the boundary conditions are phenomenological, requiring (at least for pure ^{3}He) a vanishing order parameter in the superfluid and a vanishing flow velocity in the normal liquid. This implies *diffusely* scattered quasiparticles. The assumption is made that the scattering is *elastic* at low temperatures, forcing the diffusivity to arise from geometrical roughness of the surface. In the superfluid, the roughness must be on the scale of the quasiparticle wavelength (1 nm). More gradual variations leave the surface locally smooth and allow the order parameter to regain its strength. Roughness on all scales much less than the viscous penetration depth (assuming that the height and breadth of the variations are comparable) should be equally effective in establishing the flow boundary condition.

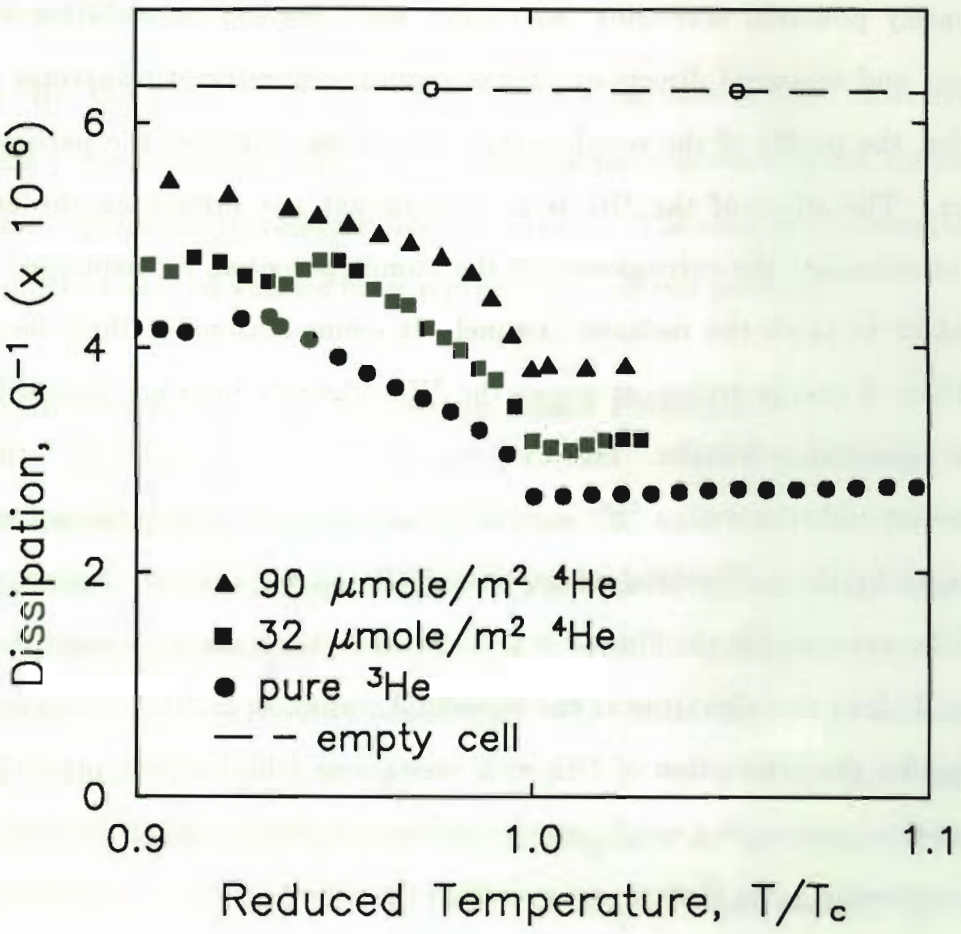

Figure 3.6

The constant offsets in the Q due to the changing boundary condition with ^{4}He coverage, seen here around the ^{3}He superfluid transition. In the slip theory, the excess dissipation is temperature-independent for a constant specularity parameter.

However, in the experiment of Ritchie *et al.*,[3] nanometer thick ^{4}He layers have a dramatic effect on the hydrodynamic boundary condition at a surface (machined epoxy) known to be rough on the micrometer scale, while the penetration depth is almost a millimeter. Since their results for *pure* ^{3}He conform well to the diffusive boundary interpretation, we propose that this boundary condition holds *even at a geometrically smooth surface.* That is, the profile of a machined epoxy surface is

probably not convoluted enough fully to establish the no-slip boundary condition. For purely potential scattering, we expect some degree of correlation between the incident and scattered directions. For maximum efficiency of transverse momentum transfer, the profile of the rough surface should be such that the particles multiply scatter. The effect of the ^{4}He is to smooth out the surface on the atomic scale (*i.e.* to attenuate the corrugations in the atomic potential, as mentioned in Chapter 2) and/or to block the inelastic channel. It seems reasonable that the well-known inhibition of energy transport across the ^{3}He-substrate interface should be reflected in the momentum transfer. This idea ties in with Hall's suggestion[18] that in order to interact with the wall, a ^{3}He excitation must tunnel through the potential barrier presented by the preferential adsorption of ^{4}He on the surface. Reppy points out[19] that ^{3}He states within the film, such as traps on vortex cores, may assist the tunneling, and could lead to a signature at the superfluid transition in ^{4}He. It may be important to consider the interaction of ^{3}He with excitations (third sound quanta) in the ^{4}He film, as this is something which changes abruptly at the Kosterlitz-Thouless transition. (We emphasize again that we are *assuming* that the ^{4}He film goes superfluid – we do not have direct evidence without observing the Kosterlitz-Thouless signature. Other possibilities include surface roughening, but seem rather unlikely.)

In summary, although geometrical roughness can certainly lead to the diffusive boundary condition, its importance has been overemphasized in recent thinking about ^{3}He. It is interesting to note that molecular dynamics simulations have found the usual hydrodynamic boundary condition for classical fluids flowing next to plane boundaries with which they interact only through the van der Waals potential[20]. Qualitatively, the atoms are temporarily localized at the surface. Another quote from Kennard[9] demonstrates that little progress has been made in half a century:

> Maxwell suggested that diffuse reflection might result from free penetration of the gas molecules into interstices in the surface, where they would strike a number of times before escaping. An approach to such reflection would result from roughness of the surface.... Another possibility is that the molecules

might condense on the surface and then re-evaporate after coming into thermal equilibrium with it; in some cases there is, in fact, definite experimental evidence for such an occurrence.

For ^{3}He, the magnetic interaction at surfaces has been studied most extensively and is not yet understood. The correct model of momentum transfer should, at the same time, explain the thermal boundary resistance. The coupling between the Fermi liquid and the localized surface layer represents a difficult problem.

3.3 Evolution of the ^{4}He Transition under Pressure

The Kosterlitz-Thouless transitions of pure ^{4}He and ^{4}He-^{3}He mixture films on mylar have been very well characterized[21]. The results may be summarized as follows. A substantial coverage of ^{4}He (the 'inert' layer, 28 μmole/m^2 for pure films) is required before any superfluidity is observed. The initial rise of the transition temperature is linear in coverage as 'active' helium is added atop the inert layer. Two effects characterize the addition of multilayer quantities of ^{3}He to the system. First, the inert coverage seemingly increases to 34 μmole/m^2, and, second, the temperature dependence of the period shift changes to reflect ^{4}He dissolving into ^{3}He as the temperature increases. It appears that mixing of the ^{3}He into superfluid ^{4}He film is a negligible effect. (microscopic picture of ^{3}He -^{4}He interface – Edwards?)

The effect of increasing pressure on the layered ^{3}He-^{4}He system should be to gradually solidify the ^{4}He layer. The Kosterlitz-Thouless transition temperature will fall as 'active' helium is driven into the 'inert' layer. These measurements are best performed in cells having a large surface-to-volume ratio and at temperatures below about 100 mK in order to assure that a negligible amount of the ^{4}He is in solution. This is in analogy to the avoidance of vapor pressure effects in bare film measurements, which typically requires temperatures below 1 K. Because ^{4}He 'evaporates' more easily into ^{3}He than into vacuum, the equivalent temperature here is about 200 mK. The

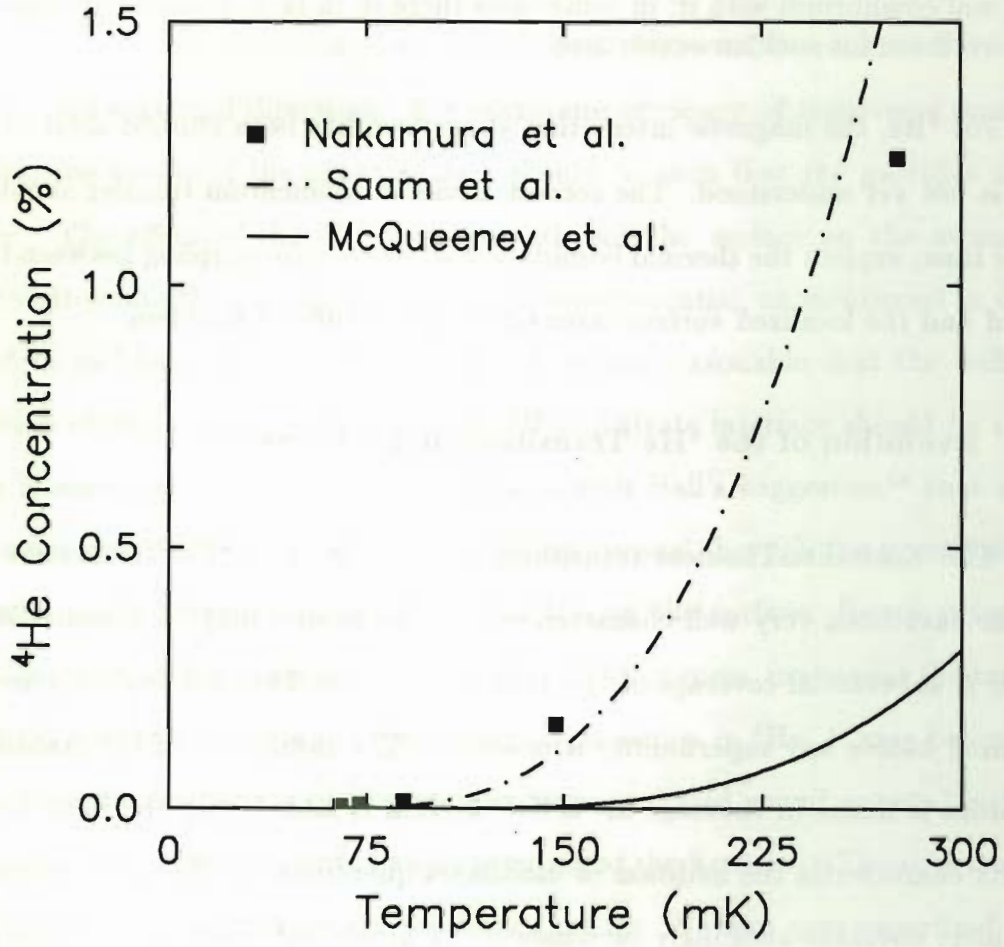

Figure 3.7

^{4}He concentration in the ^{3}He-rich side of phase separated mixtures. The symbols and dash-dot line, respectively, are measurements and theory for the bulk case. The concentration in the thin film system (solid line) is diminished by the preferential plating of the surface.

solubility of ^{4}He in ^{3}He as the temperature approaches zero is a matter of current interest. Recent experiments find values substantially greater than expected, by an order of magnitude at 70 mK, for example[22]. It is overly pessimistic of us to consider the bulk phase separation curve, however. In confined geometries, the concentration of ^{4}He in the ^{3}He rich phase is reduced by the preferential adsorption of ^{4}He on the surfaces. Some results are shown in Figure 3.7 . The prediction of Saam and

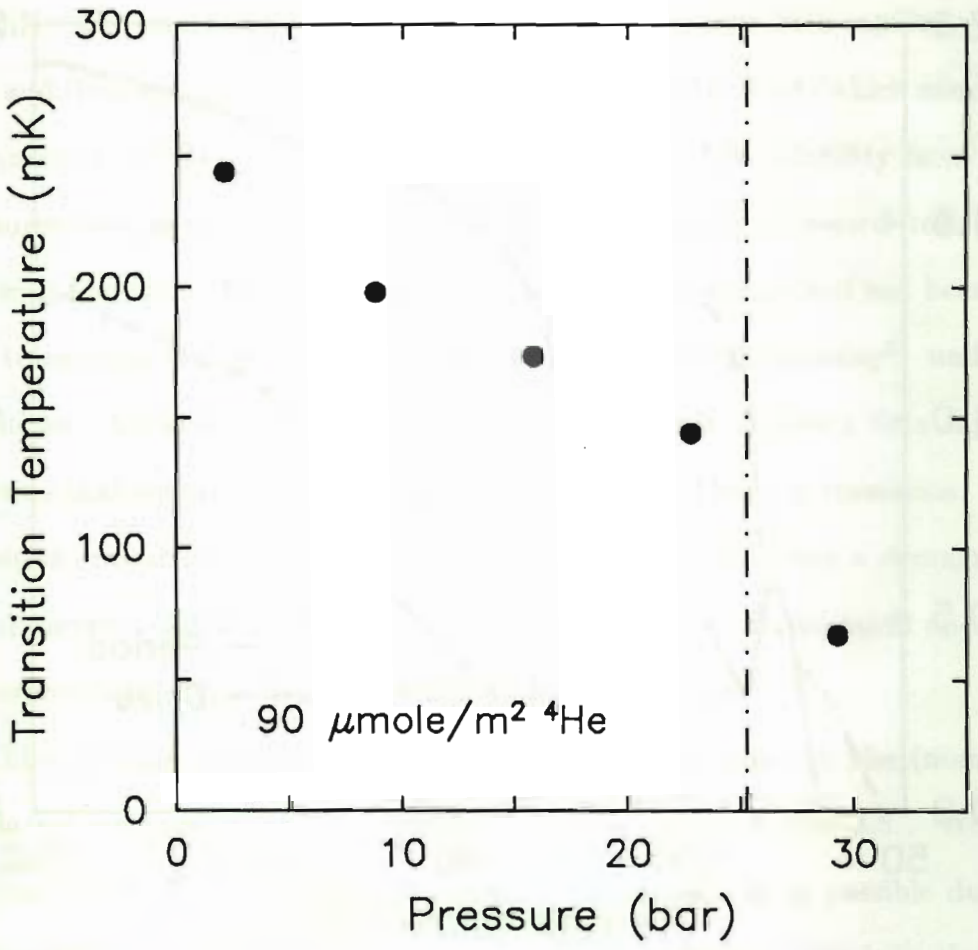

Figure 3.8

The slip transition temperature as a function of ^{3}He pressure. The measurements were made by depressurization, with the ^{4}He coverage remaining quite constant. The dash-dot line is the phase boundary between bulk liquid and solid ^{4}He.

Laheurte (see Ref. 22) is shown as a dash-dot line. The low temperature deviations of the Nakamura measurements (the solid squares) would be more apparent on a log scale. The solid line shows the concentration of ^{4}He in ^{3}He multilayers atop a 42.5 μmole/m^2 ^{4}He film on mylar, estimated from the data of McQueeney *et al.*[14]. Roughly five monolayers (70 μmole/m^2, say) of nearly pure ^{4}He can be maintained near the surface by the van der Waals potential[18]. At higher coverages the bulk phase

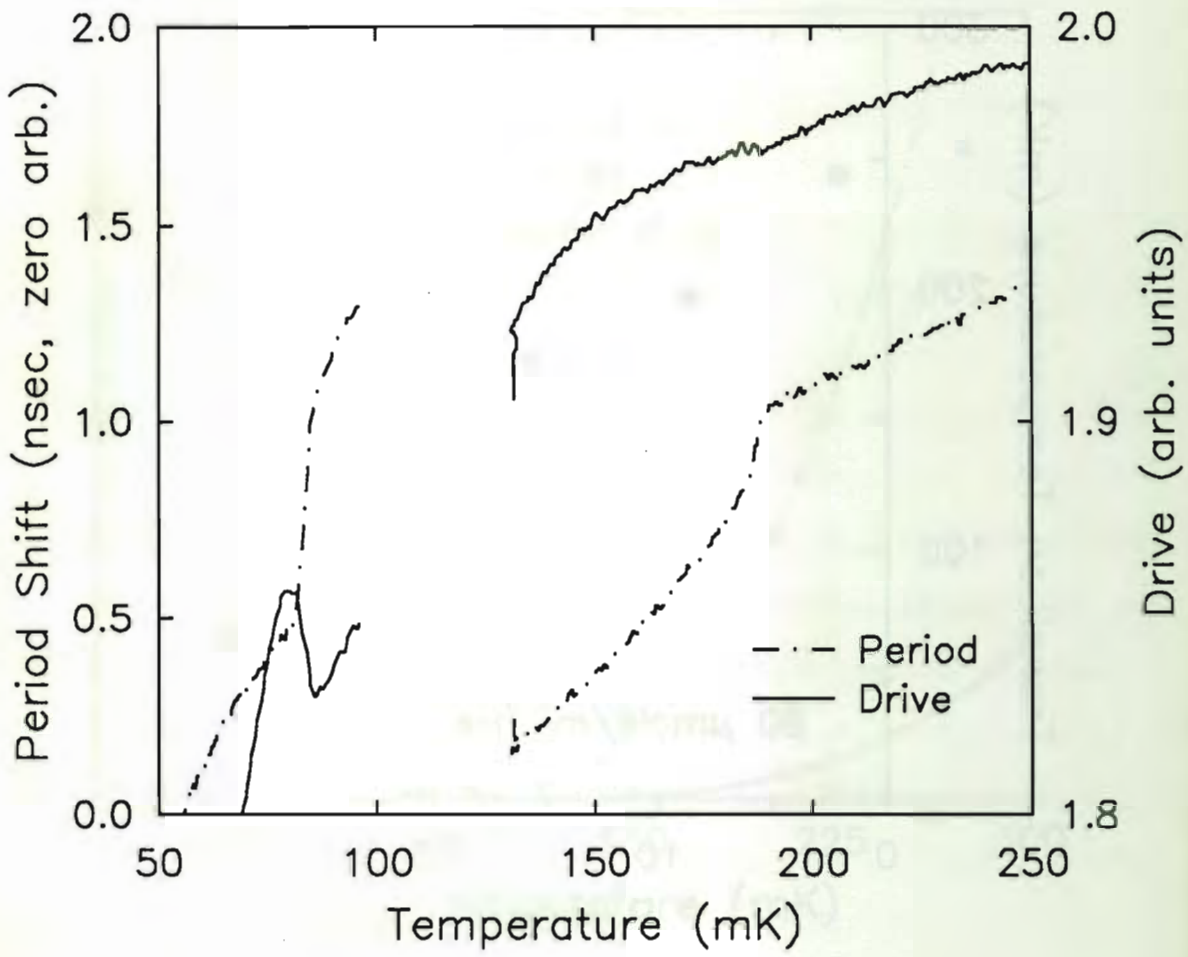

Figure 3.9

Two transitions (raw, oscillator backgrounds not subtracted), at 80 mK (29.3 bar) and 190 mK (8.7 bar). The stage temperature was regulated at the vertical section of the low pressure trace.

separation line will be approached.

We have measurements of the pressure dependence of the transition temperature for one ^{4}He coverage, 90 μmole/m^2. It is actually difficult to ensure a constant ^{4}He coverage on the mylar. For example, it may take a long time to establish the equilibrium concentration of ^{4}He in the fill line heat sinks. We introduced the ^{4}He into an empty cell, and shortly thereafter admitted ^{3}He and pressurized to 9 bar. We had paused at a ^{3}He coverage of 20 monolayers, which was the last time we were able

to resolve the dissipation peak associated with the Kosterlitz-Thouless transition (at 650 mK). The transition at 0 bar was measured twice: once with capillary condensed ^{3}He, and then again with the bulk volumes in the cell also filled (which nearly doubles the quantity of ^{3}He). We had hoped to estimate the ^{4}He solubility from these two measurements, in the manner of Ref. 14, but T_{slip} actually *increased* from 320 to 340 mK with the extra ^{3}He. This indicates that the ^{4}He coverage had not been uniform. The transitions do agree well with a measurement of McQueeney[21] under similar conditions. A feature reminiscent of a dissipation peak in Dave's data supports the assertion that we are indeed witnessing the Kosterlitz-Thouless transition. The 9 bar transition was at 240 mK, initially. Several days later, following a demagnetization, it had moved to 190 mK. We postulate that some of the ^{4}He migrated up the fill line to dissolve in the pure ^{3}He with which we had pressurized.

The pressure dependence of the transition temperature for the (nominally) 90 μmole/m^2 coverage was then measured, and is shown in Figure 3.8 . We began at 29.3 bar and tracked the transition temperature as rapidly as possible during a depressurization. The sweep took a couple of days because of the long thermal time constants. We are reassured by the fact that the 9 bar transition reproduced quite well, appearing this time at 198 mK.

The amount of Kosterlitz-Thouless superfluid is only a few μmole/m^2 at 200 mK. As much ^{4}He is dissolved in the ^{3}He in our cell when the solubility is of order 0.1%. The initial drop in transition temperature may reflect, in part, the increasing solubility of ^{4}He in ^{3}He at low pressures. Note in particular that the substrate prevents the ^{4}He film from solidifying completely at the bulk melting pressure, 25.3 bar. The relative sizes of transitions at 190 mK and at 80 mK are shown in Figure 3.9 . These are a convincing demonstration that we are not simply observing an increase in the ^{4}He surface coverage due to phase separation.

3.4 Conclusions

We have looked at the effective viscosity of normal ^{3}He in a thin cylindrical shell, in order to determine the consequences of changing the boundary condition with ^{4}He. Our main conclusions are the following:

I. The slip of the ^{3}He at the surface, as determined by the damping of the torsion pendulum, increases with increasing ^{4}He coverage. There is a transition in the system, most likely the superfluid transition of the surface ^{4}He, at which the boundary condition on the ^{3}He changes abruptly. There is a possibility that the microscopic details of the ^{3}He-surface scattering change at the ^{4}He superfluid transition.

II. Freezing of the surface of a ^{4}He multilayer on mylar is inhibited. In these stratified systems, film superfluidity can be studied at pressures well above the bulk solidification point.

The dependence of the low temperature dissipation on ^{4}He coverage is unmistakable. It would be interesting to pursue this with other adsorbed gases, to look for dependence on the van der Waals potential. Different isotopes can be used in order to control the magnetic channel. The high pressure transition is also definite. The superfluid transition is a particularly nice indication that the surface of the ^{4}He film is a liquid and not a disordered solid. In this case melting is promoted by the amorphous nature of the substrate, but the effect may also occur for ^{4}He registered on other solids. The slip amplifier technique lends itself to further study of substrate and dimensionality effects on freezing. Graphite would be interesting because it does not appear to disorder the solid. Increasing pressure freezes solid layers on graphite in a stepwise manner[6]. Small surface area substrates can also be used, and typically are easier to control and to characterize.

A number of questions do hang over the 'slip transition'. We do not believe it to be the result of phase separation, as that should produce a much larger signature

at 200 mK than at 100 mK. The effect may be due, in part, to trivial film thickness changes due to film flow driven by temperature gradients. There is also a substantial equilibrium component, however, at least at the higher temperatures. A measure of the influence of ^{4}He superfluidity on ^{3}He quasiparticle scattering could come from the ^{3}He superfluid response at pressures high enough to completely solidify the ^{4}He layer. The present cell expired prematurely somewhere along the melting curve in an initial attempt.

The experiments need to be pursued in cells specifically designed for the purpose, in order to test our conclusions. In one type of cell, the ^{3}He must be better locked. The same type of submicron-gap parallel plate geometry would serve well, without the circumferential crack. We would like to observe the dissipation peak associated with the Kosterlitz-Thouless transition in order to verify directly that the ^{4}He layer is producing superfluid. Then, in order to study the slip effects quantitatively, a cell for deliberately defined thicker films is required.

References for Chapter 3

3.1 D.S. Betts, D.F. Brewer and R. Lucking, *LT-13 Proceedings* (1972), p. 559.

3.2 A.P. Borovikov and V.P. Peshkov, *LT-14 Proceedings* (1975), p. 352.

3.3 D.A. Ritchie, J.Saunders and D.F. Brewer, Phys. Rev. Lett. **59**, 465 (1987).

3.4 S. Balibar, D.O. Edwards and C. Laroche, Phys. Rev. Lett. **42**, 782 (1979).

3.5 C. Lie-zhao, D.F. Brewer, C. Girit, E.N. Smith and J.D. Reppy, Phys. Rev. **B33**, 106 (1986).

3.6 S. Ramesh, Q. Zhang, G. Torzo and J.D. Maynard, Phys. Rev. Lett **52**, 2375 (1984).

3.7 J.D. Reppy, in *Physics at Ultralow Temperatures,* Proceedings of the 1977 Hakoné Symposium, p. 89.

3.8 We use the tabulation of Wheatley in Rev. Mod. Phys. **47**, 415 (1975).

3.9 E.H. Kennard, *Kinetic Theory of Gases,* McGraw-Hill, New York 1938, Ch. VIII. A good introduction to the ideas, and an interesting historical perspective.

3.10 H. Højgaard Jensen, H. Smith, P. Wölfle, K. Nagai and T. Maack Bisgaard, J. Low Temp. Phys. **41**, 473 (1980).

3.11 D. Einzel, H. Højgaard Jensen, H. Smith and P. Wölfle, ibid. 53, 695 (1983).

3.12 H. Smith, Physica **126B**, 267 (1984).

3.13 J.E. Jaffe, J. Low Temp. Phys. 37, 567 (1979).

3.14 D.F. McQueeney, G. Agnolet and J.D. Reppy, Phys. Rev. Lett **52**, 1325 (1984).

3.15 J.P. Laheurte and J.R.G. Keyston, Cryogenics **11**, 485 (1971).

3.16 M. Knudsen, *Kinetic Theory of Gases,* Methuen, London (1950).

3.17 J.M. Parpia and T.L. Rhodes, Phys. Rev. Lett. **51**, 805 (1983).

3.18 H. E. Hall, in *Liquid and Solid Helium*, C.G. Kuper *et al.*, ed.s, Wiley, New York (1975).

3.19 J.D. Reppy, private communication.

3.20 Physics Today, May 1988, p. 17.

3.21 See D.F. McQueeney, Ph.D. Thesis, Cornell University, 1988.

3.22 M. Nakamura, Y. Fujii, T. Shigi and K. Nagao, preprint.

Appendix A

The Cryostat and Experimental Techniques

It's ... Colder than the nipple on a witch's tit! Colder than a bucket of penguin shit! Colder than the hairs of a polar bears ass! Colder than the frost on a champagne glass!

Thomas Pynchon

A.1 The Cryostat

Before the experiments described in this thesis ran their course, the H-corridor copper nuclear demagnetization rig (in the old shielded room) was extensively renovated. This project, done in collaboration with Bob Germain, aimed at improving the mechanical, electrical and cryogenic environments of the apparatus. The modifications are described in this Appendix, which also points out areas in which the renovation is incomplete and further improvements can be made. I am grateful to Wolfgang Sprenger, who was spending a year at Cornell while these designs were prepared, for useful conversations.

A.1.1 Mechanical

As will be discussed in the cryogenics section later in this appendix, the old copper wire bundle has been replaced by a slotted solid copper bar. The only disadvantage

of this new nuclear refrigerant is that it is about a thousand times more susceptible to eddy current heating, having large areas in its cross section for the current eddies. We have therefore become more vigilant about decoupling from external sources of vibration. The most harmful vibrations are those which cause relative motion of the stage and the magnet in the region of a field gradient, although a.c. motion even in a uniform field causes some heating from the redistribution of charge associated with the Hall effect. All vibrations are damped by internal or external friction of some sort and will cause heat leaks. We are also interested in reducing interference with mechanical transducers, such as the torsional oscillator.

In this context, one thinks of a cryostat as an extremely large number of coupled oscillators, driven at subsonic and low audio frequencies by building and pump vibrations, and at higher audio frequencies by acoustic pick-up. We monitor the incoming vibrations with accelerometers and piezoelectric transducers[1], and Wolfgang has been known to study the cryostat response by sweeping the drive with a loudspeaker. But it is unrealistic to expect to find all of the important driving terms and responses, and the general approach must be to select a relatively static part of the building, mount the apparatus from a rigid frame which has resonances only far away from the response of the cryostat/air-spring combination, and hope for the best.

The new cryostat suspension begins with five inch aluminum columns anchored to the roof and supporting a triangular frame of six inch aluminum H beams. The top plate of the apparatus then floats on Firestone air-mounts[2] (discards of Dave McQueeney). Vibration isolators of the opposing bellows design are used on the still and 1K pot pumping lines. Although this arrangement has proved completely adequate in practice, I am compelled to point out the ways in which each component is less than optimal.

From the vibrational perspective, a steel frame built up from the floor would be better than the aluminum frame attached to the ceiling. Higher resonant frequencies

are possible with steel because its Young's modulus is greater than that of aluminum by a factor of three[3]. The concrete ceiling above the cryostat is not very rigid and has a significant vibrational amplitude with a peak at 17 Hz. The floor in the area is much better but also disappoints. The strongest floor mode is at 30 Hz, with about one-third the amplitude of the 17 Hz ceiling mode. The floor-mount option was eliminated by the high premium on space inside the shielded room. The extra rigidity of steel is unwarranted, given the compliance of the ceiling. The aluminum frame was particularly easy to install. It was assembled with the cryostat in place. The old support was dismantled after the weight of the platform had been transferred.

The resonance of the platform on the Firestone springs is about 1.3 Hz with the dewar raised. The tires are inflated with house air, which is allowed to bleed out slowly. acts resonance holds well enough that adjustments every other week are sufficient to keep all of the stops from touching. The platform is not loaded with extra mass, as that lowers the resonant frequency of the beams. Dave McQueeney found that mass loading these air-mounts made only small differences in the frequency (which for some reason was closer to 3 Hz on his apparatus). The Firestones have been installed in a way that enables their removal without disturbing the cryostat. Upgrading to Technical Manufacturing Corp. or other commercial legs is possible, should lower resonant frequencies ever be required. To make substantial improvements over the present performance would require active feedback.

In operation I have found one situation in which the effect of the air suspension is dramatic. A common observation is that the heat leak into a nuclear demagnetization cryostat may be small in zero field and at high fields, and actually peak at some intermediate field. The reason for this is unclear. It is certainly true that the motion of the bundle is damped by eddy currents, but if most of the vibrational energy is sunk in this manner then we would expect the heat leak to be field independent. The vibrations may not couple as strongly to the bundle modes when their Q's are

degraded by the field. It may be significant that eddy current damping in the shields quiets other sections of the cryostat. In any case, before inaugurating the air suspension I discovered that the heat leak at 2.4 Tesla was 75 nW, almost two orders of magnitude larger than the usual static heat leak. This problem was cured completely by pressurizing the air-mounts.

No improvement in the performance of the torsional oscillator was ever correlated with floating the cryostat. The dominant noise on the raw oscillator signal was a 7 kHz vibration from the 1K pot. This noise appeared also on the piezoelectric transducer mounted on the mixing chamber. Jeevak Parpia's solution to this problem is to run the pot dry or almost dry to minimize the boiling. I conducted a brief search (in vain) for a sweet operating point. The pot noise was far enough removed from the actual oscillator frequency to have only a minor influence on the period and amplitude stability.

I encountered two other dramatic heat leak problems. The first, during the initial cool down of September 1986, was an unsteady vibrational heat leak which averaged about 5 nW in low magnetic fields. It was damped out by high fields, but burned with a vengeance during transfers. The problem was attributed to rubbing between the bundle and graphite fingers on the mixer can tail cap (which were intended to prevent touches). Such spacers are unnecessary provided the shield is carefully centered, so the fingers were chopped off before the next run. This seemed to cure the heat leak problem. During the November 1987 - March 1988 run, I was surprised to be visited again by the transfer-induced flaming (the ambient heat leak remained small). This time I discovered that the problem would vanish completely if I vented the dewar during the transfer. The problem seemed to be some sound wave generated in the recovery system, generated by the check valve or the meter or the combination of the two. I chose to bypass both of them during transfers in order to eliminate the heating. Russ kindly offered to compensate for this in figuring our recovery rate.

A.1.2 Electrical

The former cryostat support structure, an array of 3/8 inch threaded rods terminated by lead anchors in the ceiling, seriously compromised the integrity of the shielded room (in addition to falling short of the mechanical isolation required by the new stage). In the new arrangement, the top of the shielded room is extended up to the concrete ceiling by three 'top hats' which envelope the support columns. The hats consist of twelve inch aluminum plates bolted to the ceiling with two-ply, ten mil nickel bellows[4] forming a flexible, electrically shielding coupling to the shielded room. The ends of the bellows are flanged and bolted to the aluminum plates and to brass hoops which are 157 soldered to the galvanized steel of the room. The seal is made with Chomerics electrically conductive gaskets[5]. The seal between the inner and outer layers of galvanized steel is maintained by brass penetrations which are soldered to the upper hoops and Cho-bonded to the inner shielded room surface. The bellows are made of nickel which (like steel) has a short skin depth thanks to its magnetic permeability, and is a workable material for making thin bellows. By using flexible bellows we decouple the cryostat frame from vibrations caused by walking in and rolling dewars around the room, and avoid the potential problem of pulling the fundamental vibration of the shielded room roof into resonance with the 17 Hz concrete ceiling mode.

The major shortcoming of the shielded room now is that some primaeval Clark Hall water leak was allowed to rust right through the joints between roof panels. These joints must be disassembled and sanded clean if the room is to function properly. Ray-Proof recommends re-tightening of these seals every two years. I never got around to the experiment which I had planned that required good rf shielding. In my case, the room was more valuable as an acoustic barrier.

The other significant electrical improvement to come out of the renovation is elimination of multiple ground connections to the cryostat (Bob has recently achieved

a resistance of over 1 kΩ between the cryostat and ground). The pumping lines are attached using KF flanges with Macrovac plastic o-ring retainers and Huntington plastic clamps. There are no such electrically isolating breaks in the high pressure lines from the ^{3}He gas handling systems, since the gas racks need not be grounded elsewhere. The cryostat itself is grounded through a heavy copper braid to the feed-through panel at the shielded room wall. All important signals are amplified at the cryostat head using preamps powered by floating dc supplies. Signal grounds are broken at the shielded room wall, either by transformers or by floating op-amps. The melting curve ratio transformer control lines are optically isolated at the wall. The only other electronics inside the room are the resistance bridges, which keep track of the status of the refrigerator, and magnet power supplies (normally off). Off-balance and monitoring outputs from these are run through the isolation amps before reaching the feed-through panel.

A.1.3 Cryogenic

The heart of the cryostat, the nuclear demagnetization stage, is described in this section. The primary constraints going into the design of the stage came from NMR requirements, but more generally the intent was to make the stage easily adaptable to different kinds of experiments and well matched to the modest cooling power of the dilution unit. That summarizes how the finished product came to be a small copper bundle attached by a thermal compression joint to a silver disk. The performance has been very satisfying. The new stage gets down farther than its predecessor, can get there faster and hold it longer.

The stage is depicted in Figure A.1. The main plate is half inch thick cold-rolled fine silver ($3\frac{1}{2}$nines) from D.F. Goldsmith[6]. Silver has two advantages: a small gyromagnetic ratio which yields a small nuclear heat capacity in the field of the NMR solenoid; and, a larger coefficient of thermal expansion than copper, for driving the compression joint. Cold-rolled plate is used for its relative hardness. As-cast silver is soft like butter. The stage must survive the threading in of thermometers and heat sinks, as well as compress around the bundle without flowing plastically. The favorable aspect ratio of the plate means that the residual resistance of cold-rolled silver is far from limiting the thermal contact.

An OFHC copper bar was machined and annealed to serve as the nuclear refrigerant. Higher purity material is unnecessary in this case. Lorinda Opsahl performed many test anneals and found that a residual resistivity ratio (RRR) of 300 could be counted on for the stock used in the bundle. (Recipe: $\sim$ 1 day at 850 C in O_2 partial pressure of 10^{-5} torr; pressure maintained by continuous pump and bleed because of outgassing. See Ref. 7 for further information.) The design goal of the stage was to reach 100 μK with a 1 nW heat leak. This can be done with a thermal resistance equivalent to 150 nΩ, so the 50 nΩ resistance along the bundle with RRR=300 is not a constraint. In the figure the bundle is shown in cross section at various points. The slots were gang-milled using sixteenth-inch mill saws with side-cutting teeth. The remaining copper fins are also one-sixteenth of an inch thick. We estimate the eddy current heating to be of order 10 nW for typical demagnetization rates. The vibrational heat leak is much harder to estimate, given that we don't know the driving forces and responses. The most susceptible area is between the high field and compensated regions of the solenoid, where there are large field gradients. We minimize this problem by machining away most of the metal in this transition region. The 80 mil thick fins of the remaining cross piece provide adequate rigidity and thermal contact.

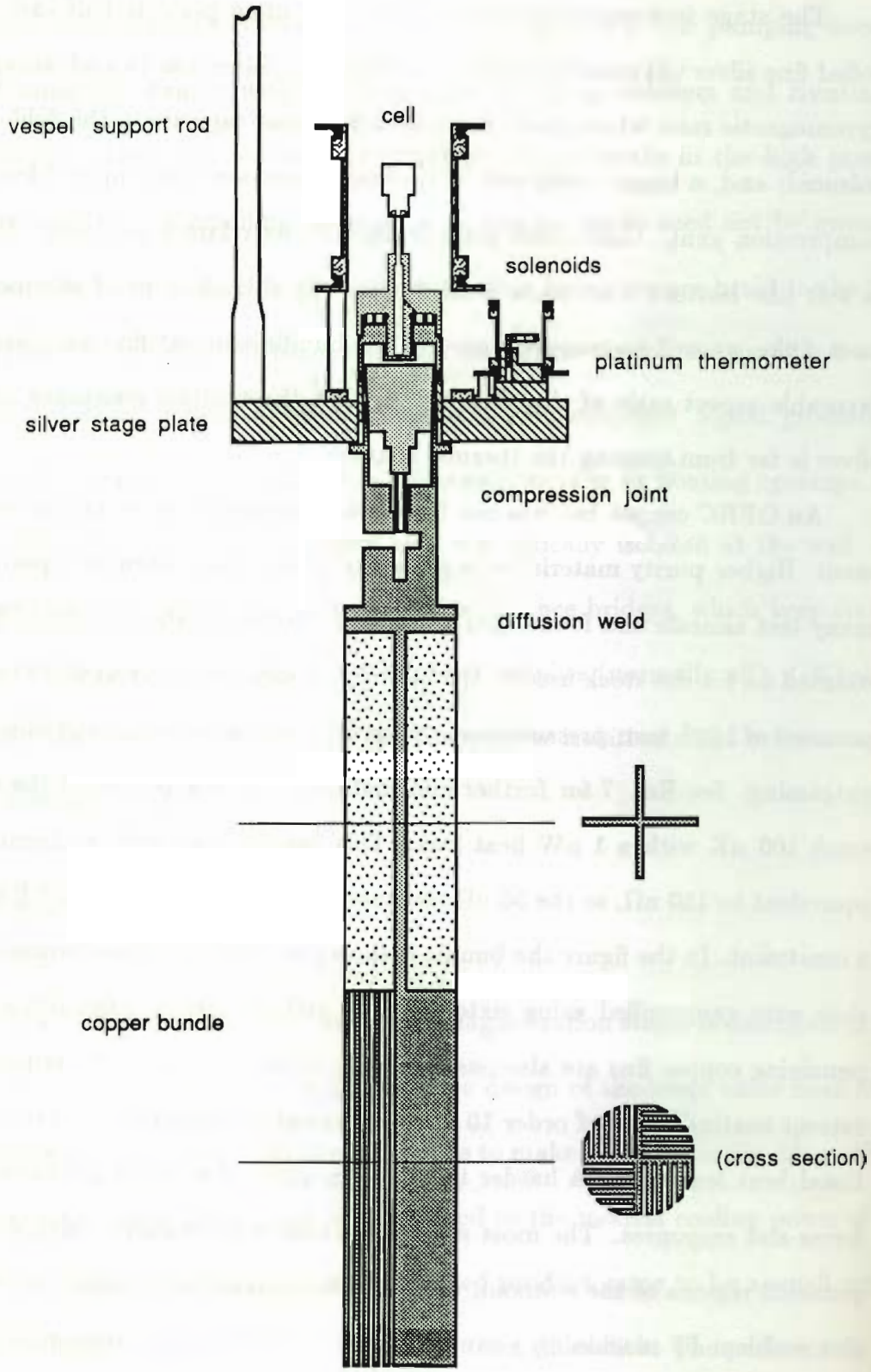

Figure A.1 The Nuclear Stage (scale 1:2).

Details of the joint between the bundle and stage are shown in Figure A.2. It is essentially a poor-man's version of the compression collar designed by Wolfgang at Bell Labs. The Sprenger joint uses the differential thermal contraction of coin silver and tungsten to generate a pressure of about 8000 psi on a slotted copper sleeve gripping a cylindrical silver bar. This pressure is *nominally* the yield strength of annealed silver and if exceeded will cause the joint to slacken from thermal cycling. (The yield strength is determined from the force required to cause some permanent deformation of the material, usually 0.5 %. Taking a piece of cast silver to the hydraulic press in TOL, I produced a 2 % deformation with repeated cyclings to 4000 psi. The initial compression was by $\sim$ 0.75 %.) The slots ensure that the compression force will be transmitted radially and not taken up around the ring. A taper is used to remove all play from the joint at room temperature. This is the most crucial aspect, as the displacement from differential contraction is only a fraction of a mil.

Our version of the compression joint is shown in Figure A.2. 20 mil radial slots are spark cut to divide the sleeves at the top of the bundle and the base of the cell each into twelve 'fingers'. The sleeves overlap and are squeezed between the silver stage plate and a tapered plug. Using results for the strain components of a thick tube under internal and external pressure[8] and tabulated values of the thermal contractions of different materials[9], we estimate the pressure across the interface between a disc and a cylinder around which it shrinks. The answer becomes independent of cylinder radius, r_1, in the limit in which $r_1 \ll r_0$, where r_0 is the outer radius of the disc. For silver contracting on copper, we expect 5000 psi to develop upon cooling to helium temperatures. Again, this assumes that the surfaces mate perfectly at room temperature. We have taken into account the elastic deformation of the copper (its Young's modulus is similar to that of silver). 5000 psi seems ideal, as the joint should remain nearly elastic while developing a high enough pressure to establish good electrical contact.

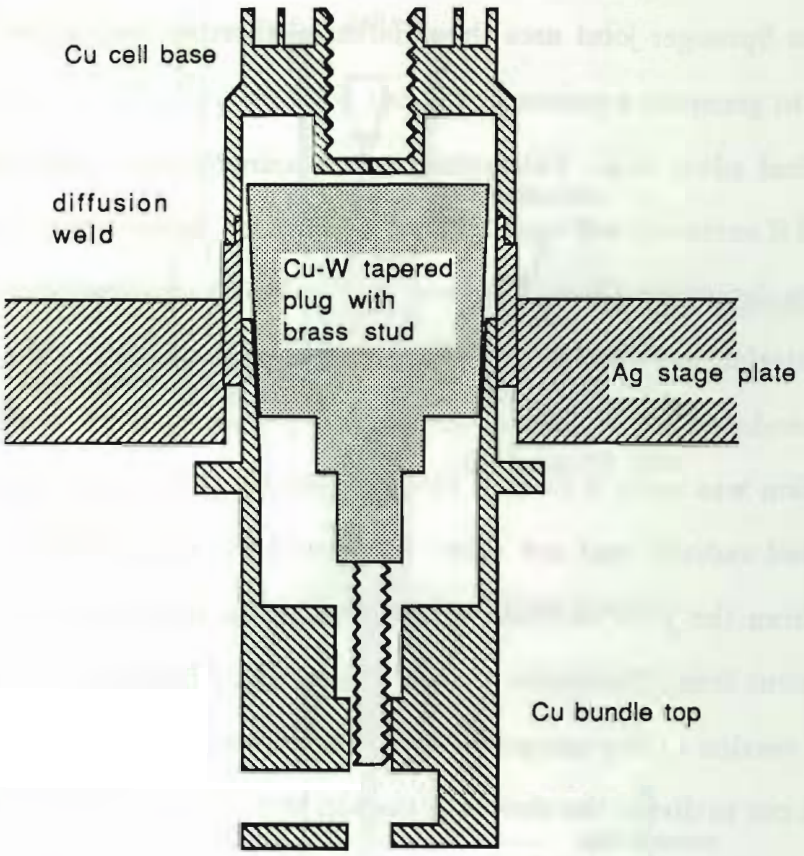

Figure A.2 Detail of the compression joint (scale 1.5:1).

The performance with a copper plug was disappointing. The electrical resistance of the joint, determined from the thermal resistance at low temperatures, was 1.5 $\mu\Omega$. Our initial presumption was that this was due to insufficient compression, and we replaced the copper with machinable copper-tungsten alloy[10], a lower thermal contraction material[9]. This lowered the resistance to 0.6 $\mu\Omega$, a substantial improvement but still much larger than it ought to be (compare the resistance along the length of the bundle). It is likely that the compression is adequate and that the limiting factor is now the condition of the surfaces. We tested some press

joints using $\frac{1}{4}$ - inch square copper and silver bars, bolted together with one axial 4-40 screw. The pressure at the interface is probably about 1500 psi. The room temperature resistance of the test piece was typically 11 $/mu\Omega$. The low temperature resistance was dominated by the joint, and depended strongly on surface preparation. The lowest resistance, 350 nΩ, was obtained by etching both surfaces (Cu in $HN0_3$, Ag in 50/50 conc. NH_4OH and 30 % H_2O_2) prior to assembly. Gold plating on one or both sides increased the resistance respectively to 1.5 and 15 $\mu\Omega$. No surface treatment beyond simple cleaning gave 3 $\mu\Omega$. All surfaces in the bundle joint were lightly gold plated, and the 0.6 $\mu\Omega$ resistance corresponds to 7 $\mu\Omega$ over the area of the test piece. We have not pursued this matter further, but it is clearly of central importance.

The beauty of this technique is that the refrigerant effectively becomes an extension of the cell. One is then free to optimize the bundle to suit the experiment, for example by using $PrNi_5$ if the minimum temperature requirements are modest. There is also no impediment to omitting the nuclear refrigerant completely. This gives great flexibility for performing experiments at mixing chamber temperatures in high magnetic fields.

The link to the mixing chamber is a cast silver bar, expertly welded to the plate by Bob Snedeker. A tin heat switch is used. A single 10 mil foil bridges the $\frac{1}{8}$inch gap from the silver bar to a copper post from the mixing chamber. Each side is pre-tinned and the foil is easily fused in place, without flux, using a large soldering iron. A small U-bend in the tin prevents tearing from the differential contraction of the silver bar and the vespel/brass stage support legs. The foil is from Materials Research Corporation and is nominally 6-nines pure. A test piece had a RRR of 3500 even after repeated bending. It is important to do these tests and not accept high-purity materials at face value. I obtained purported 6-nines copper from MRC which had a RRR of 40 as received, and increased to a stunning 150 after an oxygen

anneal (marginally superior to an OFHC copper lathe tailing). Their compositional analysis conveniently omitted most of the periodic table, including Mn, Zn and all of the refractory metals. The heat switch is positioned above the mixer can flange to reduce the overlap of stray fields from the heat switch and NMR magnets. The heat switch solenoid slips inside a mu-metal sleeve.

We have replaced the old hair ball heat exchanger inside the mixing chamber with 5 μm copper and 200 nm silver sinters in a copper base. The base temperature of the fridge is now less than 10.5 mK, improved by almost a factor of two from several years ago.

The new stage plate maximizes the available room for installing an experiment. The old stage plate, able to accommodate four liquid experiments at a time, itself occupied half of the vertical space below the mixing chamber. At low temperatures the ^{3}He dominates all contributions to the entropy outside of the nuclear refrigerant, so having less of it means more reversible demagnetizations. In order to reduce pre-cool times, we have also reduced the amount of refrigerant. This can be achieved with no penalty in staying power, provided that the heat leak is simultaneously decreased.

Special attention must be paid to the alignment of the shields when preparing the cryostat for cool-down. The present shimming of the platform is such that the still pumping line hangs vertically. Plumb bobs may then be hung from the 4K flange (I tape them to the outside) and used to center the tails of the bundle and of the shields. The wooden end of a Q-tip will clear between the flat sides of the bundle and the mixer shield when it is properly centered. I float the still shield electrically, using Kapton tape around the flange and nylon bushings under the screw heads. A lead is indium soldered to the shield. This is connected to an audio alarm which sounds if the path to ground is completed by a touch between the still shield and the vacuum can or the mixer shield.

A.2 NMR Stuff

These are some miscellaneous notes on solenoid design and construction, the Pt NMR thermometer, and the computer-controlled NMR spectrometer, for the perusal of any interested parties.

The solenoid designs are based on the article of Garrett[11]. The configuration is shown in Figure A.3, with dimensions appropriate to the Pt solenoid. A scaled up (2×) version of this surrounds the helium cell and was also used in the SQUID NMR development (Appendix C). The field of the straight solenoid peaks in the middle, and this gradient is bucked out to high accuracy by that of the field of the two paraxial coils. I chose this arrangement because the aspect ratio is more convenient than that of the more common straight solenoid with over-wound ends (this magnet has a larger bore for the same length). In Garrett's design the square end coils are treated as thin filaments of current. The first error term, or deviation from uniformity, is in this case proportional to an eighth order Legendre polynomial. According to Garrett, "the field of this three-element combination is more uniform than that of any other known system of comparable simplicity." The design was tweaked for the effect of the finite thickness of the real coils using the magnet routines which date from Hans Bozler's tenure in the low temperature group. These calculate the field due to cylindrical elements using the elliptic integral formulas.

The coil form is of metal, in this case brass, for dimensional accuracy. Brass is chosen at some risk, as it has been known to contain magnetic inclusions, such as bits of tool steel that may have been swept off a shop floor somewhere. The coils are wound using 4.2 mil diameter formvar insulated copper-nickel clad niobium-titanium monofilamentary wire. In the multilayer sections we obtain a winding density of about 8900 turns/cm^2 with this wire. Kapton tape was wrapped on the brass before winding, as insurance against shorts. The larger incarnation of the coil form was coated with epoxy and then machined to its final dimensions.

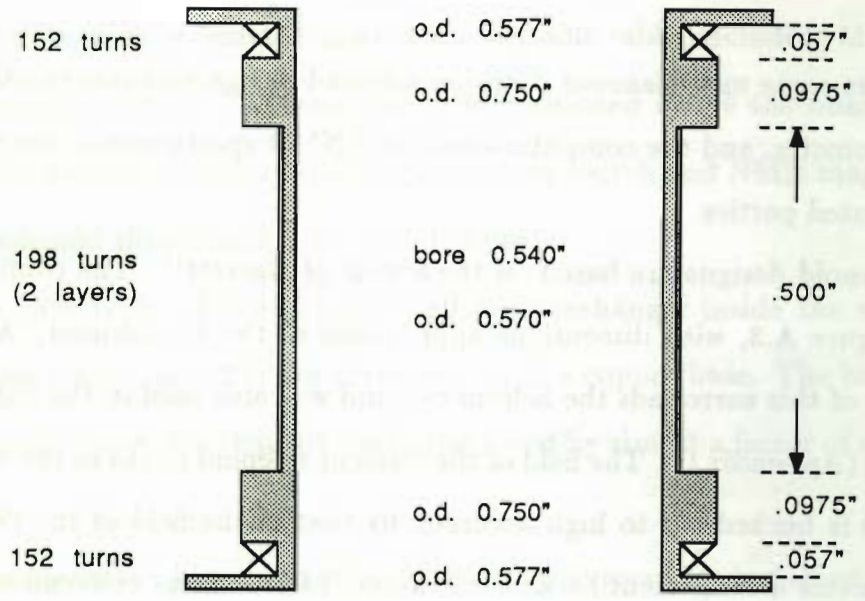

Figure A.3 Dimensions of the eighth-order solenoid for the Pt thermometer.

In practice it is easy to design for a much more homogeneous field than can be achieved with the actual winding. The larger magnet was wound using separate lengths of wire for each coil section. This way the field can be shimmed by adjusting the currents independently. The variation across a cylindrical sample of quarter-inch dimensions is approximately 5 parts in 10^4. The Pt solenoid has no shimming capability, as a homogeneity of a few parts in 10^3 suffices, given the intrinsic linewidth of the resonance. Most of our data was taken using an American Magnetics solenoid which slips between the vacuum can and the compensated region of the MCA demag solenoid. This coil is much larger than our home-made magnets, and is wound to be uniform to 1 : 10^5 in a 1 cm diameter spherical volume, without shimming. (The design is good to 10^{-7}, by the way.) In practice we obtained 1 : 10^4, limited by gradients in the field from the demag coil. Some improvement was obtained through shimming with external (room temperature) gradient coils. Note that the American Magnetics solenoid is rated to 1 T, although I only used it up to 30 mT.

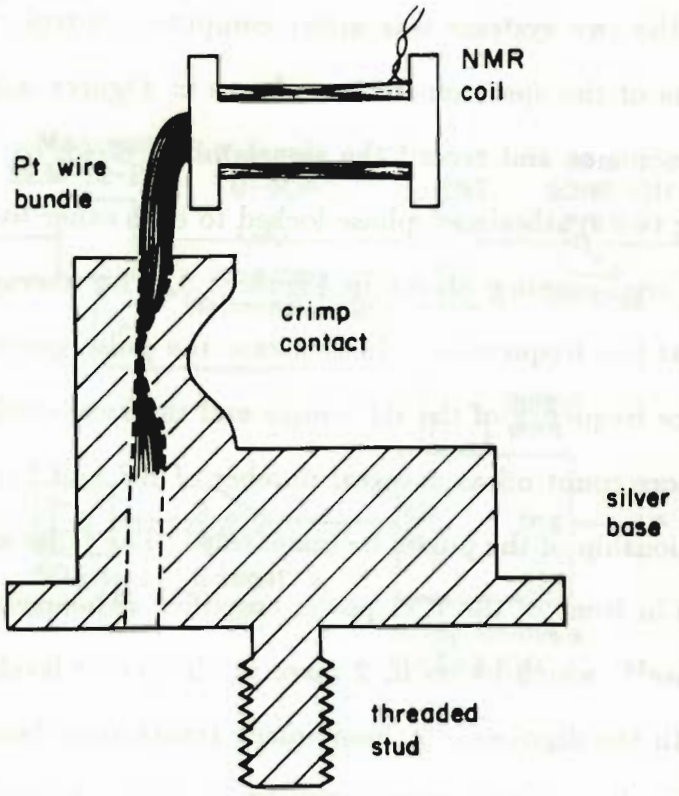

Figure A.4 The Pt NMR thermometer (scale 5:1).

The Pt NMR sensor is depicted in Figure A.4. This design was inspired by the paper of Buchal *et al.* [12]. 1 mil bare Pt wire from Sigmund Cohn (a 1972 batch) was wrapped into 500 loops and pulled into a 70 mil hole in the silver base. In retrospect a 60 mil hole would have sufficed. The silver was crushed around the wire bundle using about 100,000 psi applied to a $\frac{1}{8}$ inch diameter area with a brass jig. The free end of the bundle was clipped, and the wires splayed out for deposition of an insulating layer of SiO_2. This was done in the e-beam evaporator in TOL, using the rotating mount built by Tom Klitsner. 1 μm of SiO_2 was put down. It did not stand up under the abuse of ohm-meter probes, but complete insulation is not required in this application.

The Pt and ^{3}He NMR signals were acquired using the same spectrometer. Toggling between the two systems was under computer control. The transmitter and receiver sections of the spectrometer are shown in Figures A.5 and A.6. Typically we pulse on resonance and record the signal mixed down to 10 kHz. We had the luxury of using two synthesizers, phase locked to each other by a common reference. The particular configuration shown in Figure A.5 is for averaging (required for the helium signal at low frequencies). In this case the pulse generator must be clocked at the difference frequency of the RF source and the local oscillator, and this period must furthermore count off an integral number of RF and LO cycles, in order that the phase relationship of the pulses be maintained. The pulse amplitude is controlled by attenuators in front of the ENI power amplifier. The cryostat is protected by a $\frac{1}{16}$ amp RF fuse[13], which blows in 2 msec at the power levels we use (this is easy to measure with the digitizer). A home-made transformer breaks the ground at the shielded room wall, and the pulse is shuttled into the helium or platinum side by and RF relay within the shielded room. Several pairs of crossed diodes block any RF leakage from the transmitter. Isolation between the transmit and receive sides is provided by crossed coils for the ^{3}He, and for the Pt by a lumped-element quarter-wave network, as described in Fukushima and Roeder[14] (the Pt is a fixed frequency, single coil operation).

The receiver is a chain of commercial 50 ohm amplifiers[15]. The coils are tuned to 50 ohms using Voltronics cylindrical capacitors[16], which are tremendously easier to adjust and more stable than air-gap plate capacitors. The Anzac AM-109 and AM-110 are rather noisy, with 5 dB noise figures, but their compensating features are high input compression points, which make them well-behaved in pulse applications. These are followed by a chain of Comlinear video amps, in order of increasing noise figure. Two local oscillator signals with a relative phase shift of 90°are obtained using a Merrimac quadrature hybrid[17].

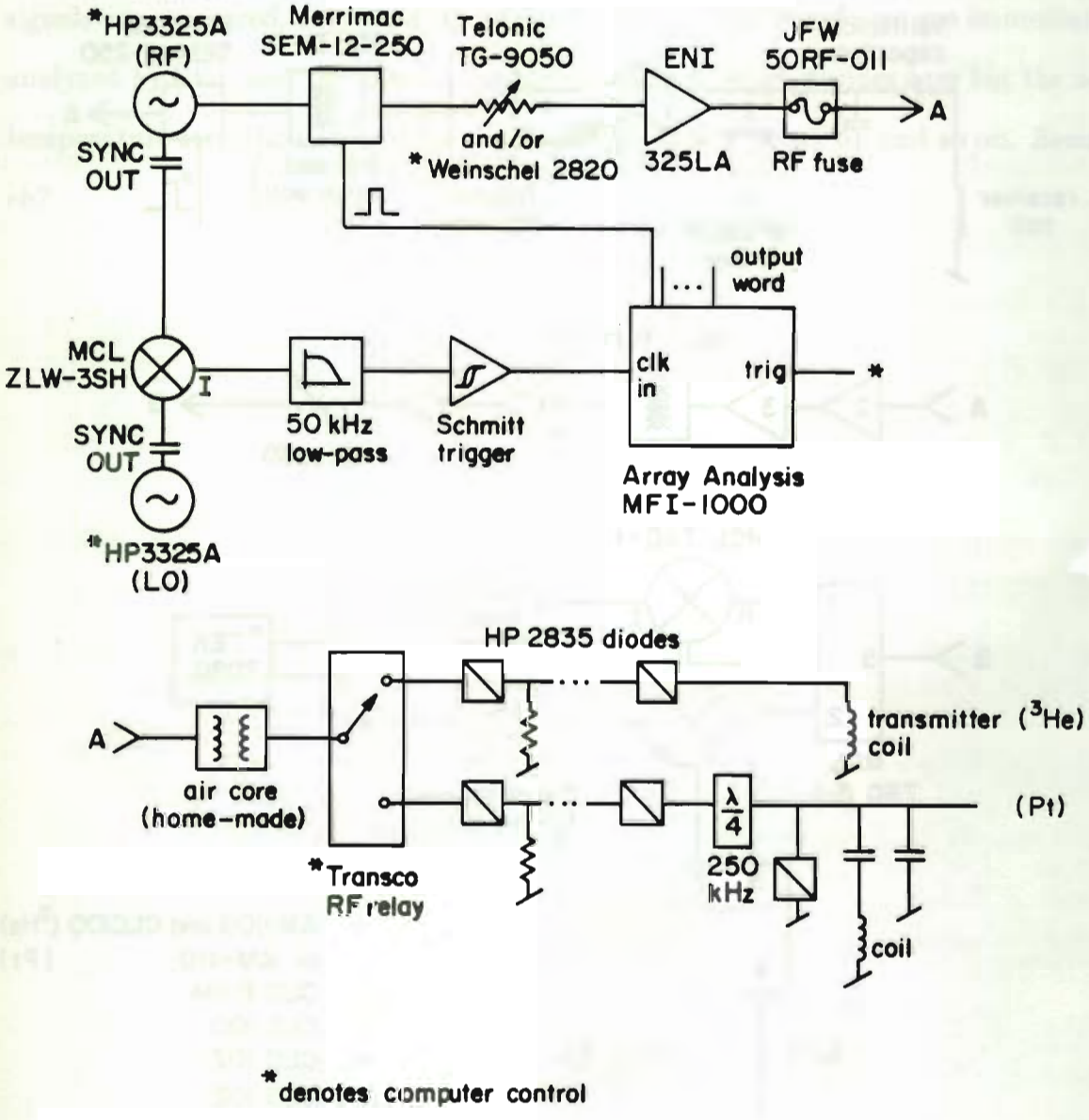

Figure A.5 The transmitter arm of the spectrometer.

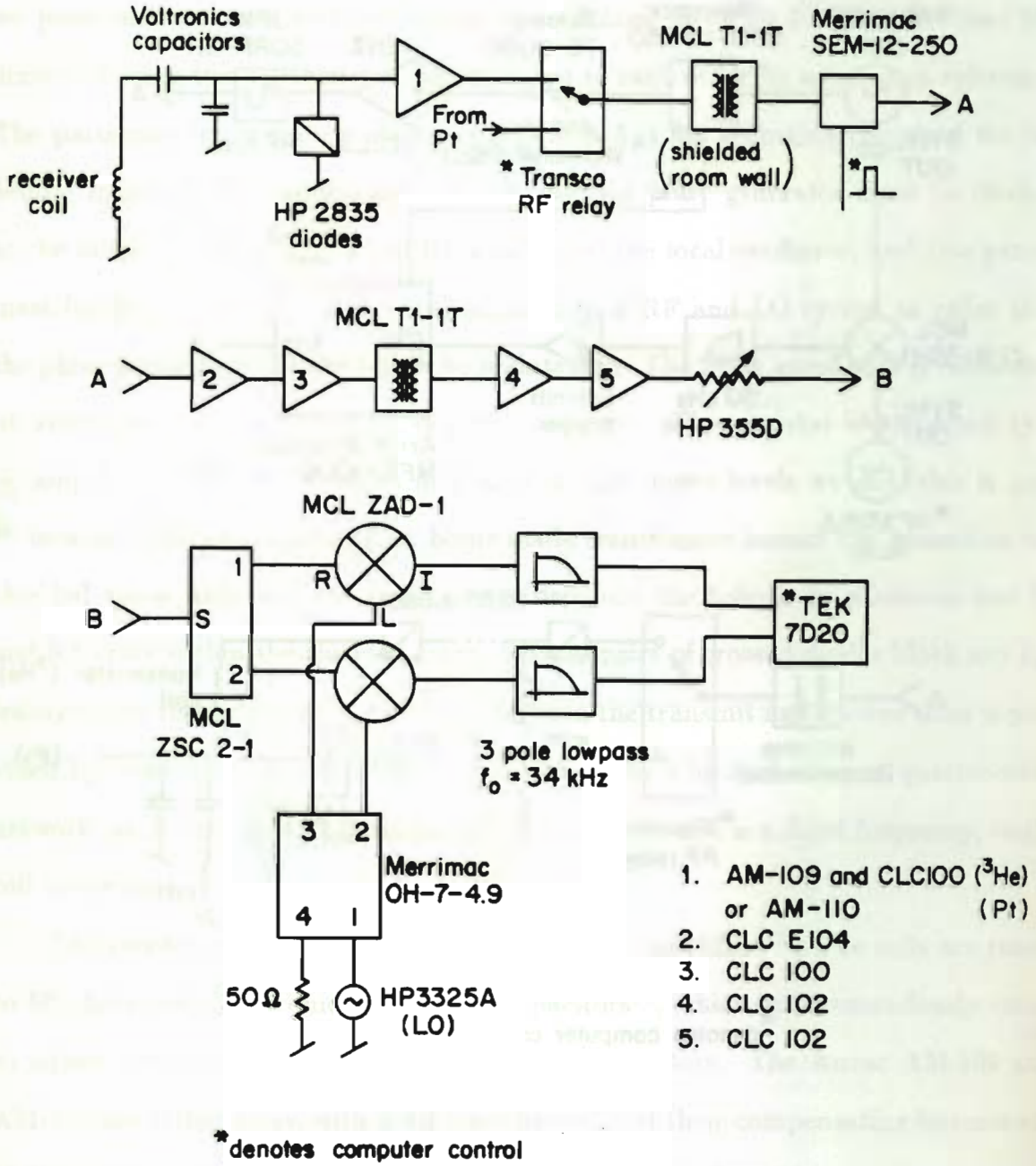

Figure A.6 The receiver arm of the spectrometer.

It was incredibly easy to automate the experiment using the Hazel(Medusa)/Plot monolith of McQueeney *et al.*. The magnets are persisted, and the temperature changed by heat pulses into the stage. After waiting for equilibrium, the Pt and ^{3}He signals are measured, at several tip angles if desired. The waveforms are immediately analyzed by Plot, and the answers returned to Hazel, which decides how big the next temperature step should be, what the frequency should be set to, and so on. Beauty, eh?

References for Appendix A

A.1 The accelerometers used are the Geophone seismometers in TOL; piezo transducers are from Piezoelectric Products, Metuchen NJ, and are mounted inside the cryostat.

A.2 Firestone Tire and Rubber Co., Akron OH.

A.3 See Timoshenko and Young, *Elements of the Strength of Materials*, 5^{th} ed., Van Nostrand 1968, for problems involving bending of beams and other elastic phenomena.

A.4 Hyspan Precision Products, Inc., Chula Vista CA.

A.5 Chomerics, Inc., Woburn MA.

A.6 D.F. Goldsmith Chemical and Metal Corp., Evanston Ill.

A.7 A.C. Ehrlich, J. Mat. Sci. **9**, 1064 (1974) (annealing of Ag); F.R. Fickett, J. Phys. F. **12**, 1753 (1982) (annealing of Cu).

A.8 A.E.H. Love, *A Treatise on the Mathematical Theory of Elasticity*, 4^{th} ed., Dover, 1944, article 100.

A.9 Linear thermal contractions, RT to 0 K: Cu 0.33 %, Ag 0.41 %, W 0.09 % (from White); CW-80 0.15 % (my measurement).

A.10 Mi-Tech Metals, Inc., Indianapolis IN. The CW-80 alloy (80 % W and 20 % Cu) is good for low temperature use because it does not contain Ni or Fe.

A.11 M.W. Garrett, J. Appl. Phys. **22**, 1091 (1951).

A.12 C. Buchal, J. Hanssen, R.M. Mueller and F. Pobell, Rev. Sci. Inst. **49**, 1360 (1979).

A.13 JFW Industries, Inc., Beech Grove, IN.

A.14 E. Fukushima and S.B.W. Roeder, *Experimental Pulse NMR, a Nuts and Bolts Approach*, Addison-Wesley, Reading (1981).

A.15 Adams-Russell, Anzac Division, Burlington MA.; Comlinear Corp., Fort Collins CO.

A.16 Voltronics Corp., East Hanover, NJ.

A.17 Merrimac Industries, Inc., West Caldwell, NJ.

Appendix B

Calibrations and Data

I would like to go on and on.

Yasumasu Kanada, World Champion Evaluator of π

This Appendix records a couple of important calibrations, presents a few aspects of the data which were not treated in the main chapters, and summarizes some of the superfluid density and NMR shift measurements for reference purposes.

The calibration of the Platinum thermometer against the melting curve, shown on the following pages, indicates that the most recent melting temperature scale of Greywall (Ref. 2.3) is more correct than earlier scales. We then show the total period shift of the oscillator upon filling with ^{3}He, as a function of pressure, along with the (calculated) component due to the ^{3}He moment of inertia alone. In effect, the empty cell period is a weak function of pressure because of the slight shape change which occurs. It is essential to take this into account when normalizing period shift data in order to extract superfluid densities. Some NMR lineshape information is presented, in particular the linewidth in the vicinity of the transition and a plot showing the spin-wave mode which appears in the superfluid phase. We show the results of a (fruitless) depressurization run, which was undertaken as an efficient means of searching for the A-B transition line. Finally, we collect together some of the NMR frequency shifts and the raw oscillator period shifts for the superfluid with and without the surface ^{3}He layer.

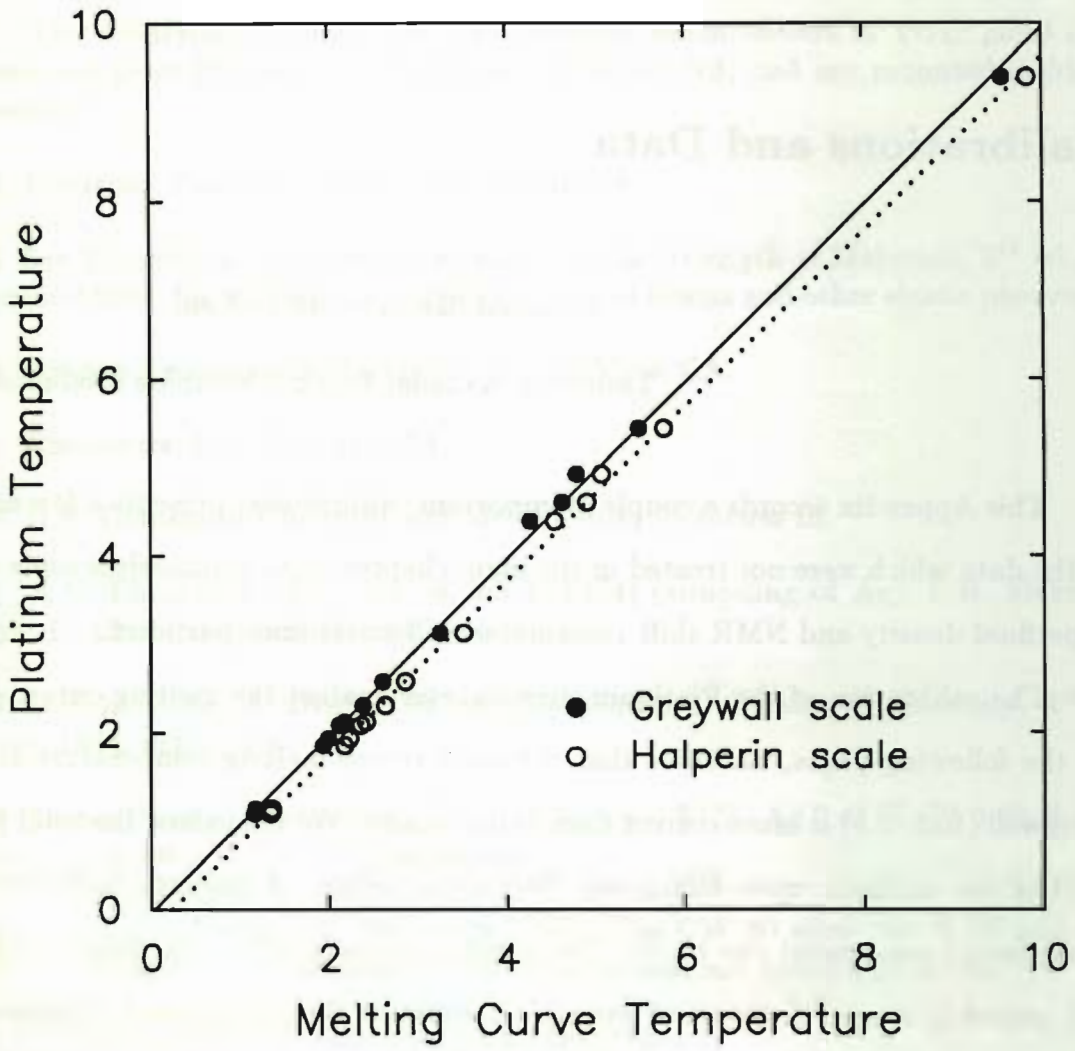

Figure B.1

Calibration of the platinum thermometer using the melting curve. When plotted against the Halperin melting curve, the linear least-squares fit to the inverse platinum susceptibilty does not pass through the origin. Rather, it has an intercept around 250 μK. Using the recent Greywall calibration, we find the expected Curie-law behaviour. This is an independent test of the validity of the new temperature scale.

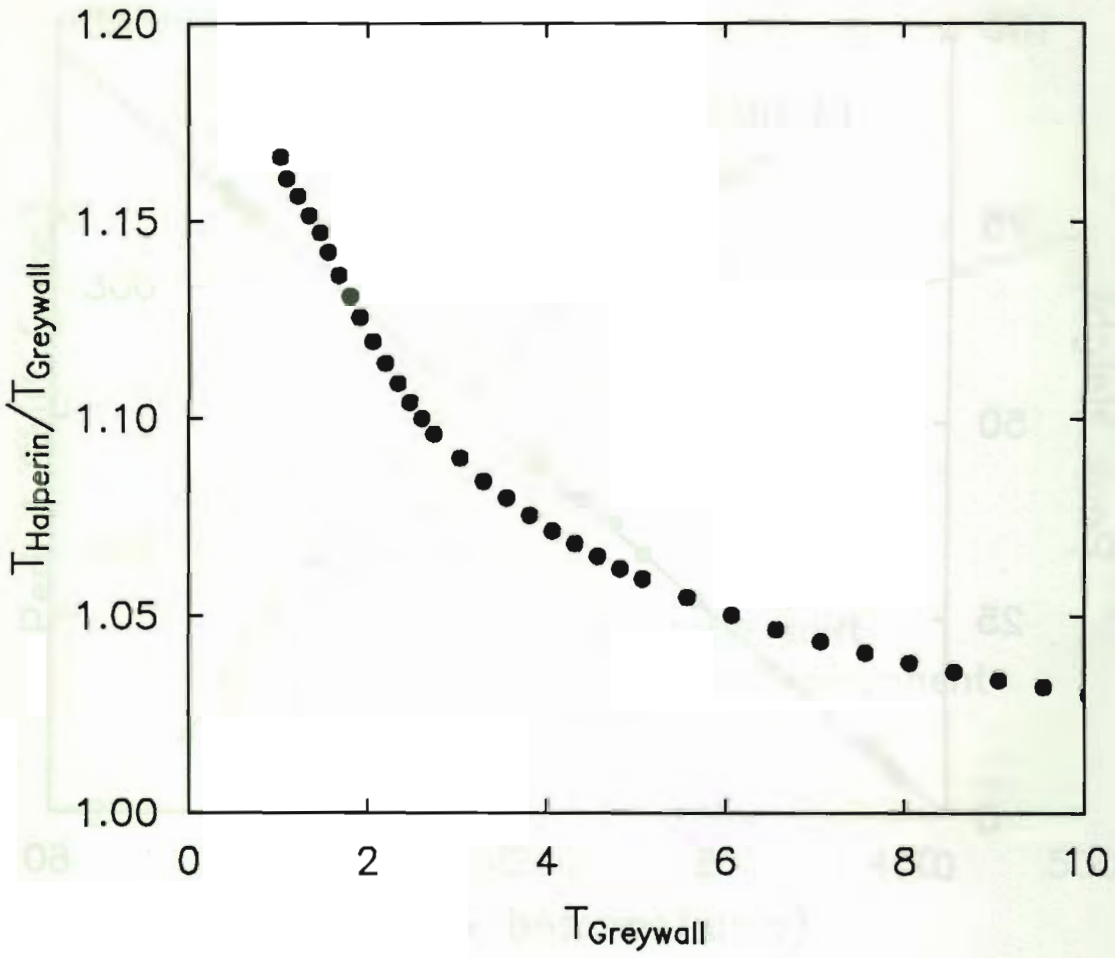

Figure B.2

A plot of the ratio of temperatures, Halperin to Greywall *at the same melting pressure*, as a function of the Greywall temperature. The nonlinearity is the cause of the offset seen in the platinum calibration.

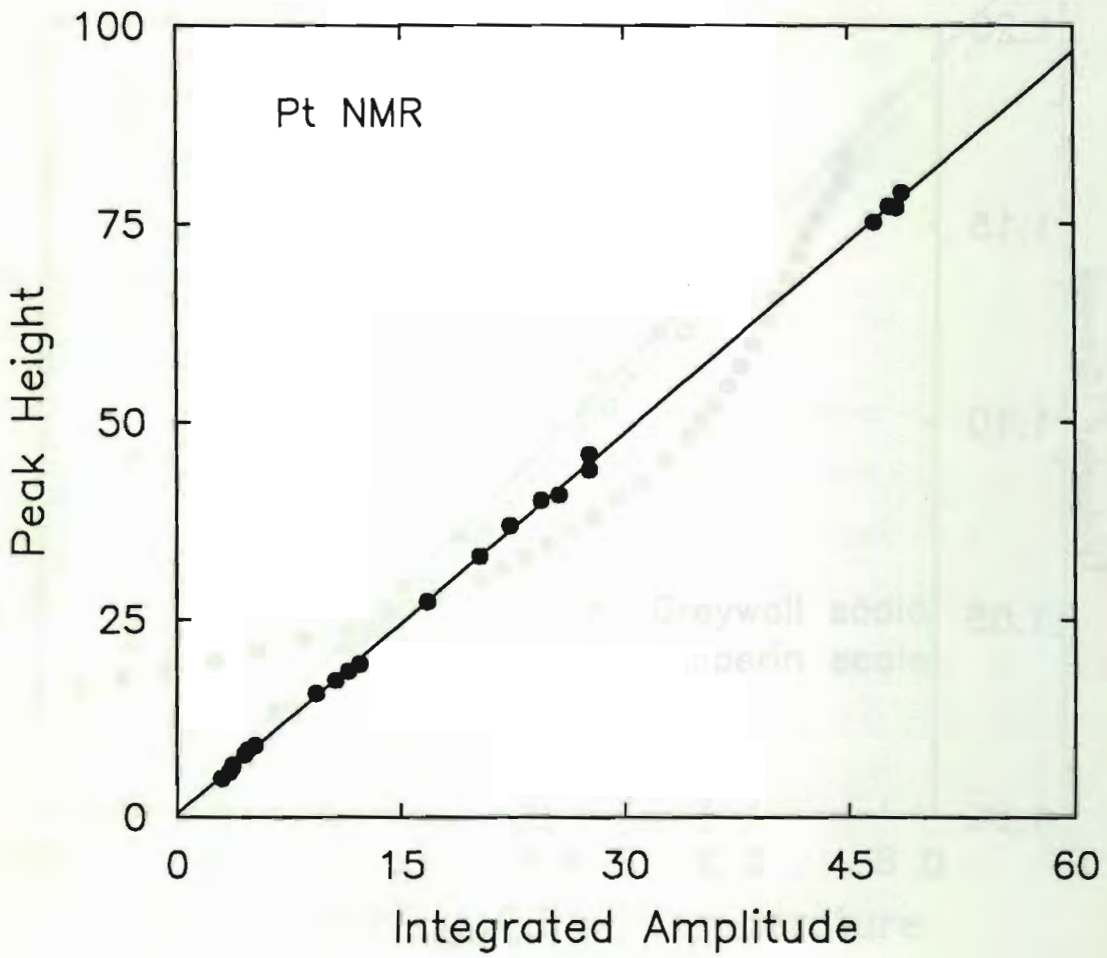

Figure B.3

Proportionality of the peak height and integrated amplitude of the Fourier transformed Pt free induction decays. This demonstrates temperature independence of the lineshape, a requirement for reliable thermometry.

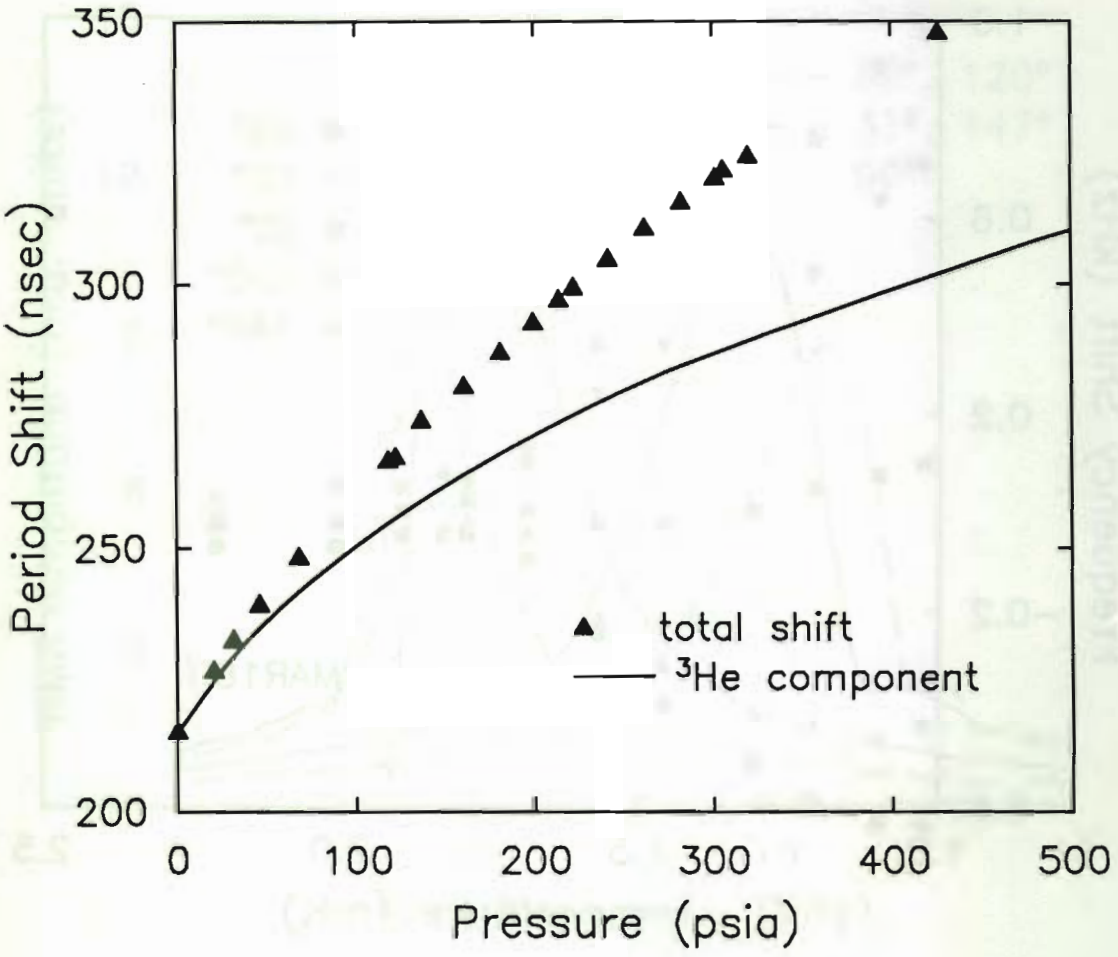

Figure B.4

Shift of the oscillator period from its empty value, measured at low temperatures (with all of the helium locked). The excess shift at high pressures is due to a slight (of order 1 micron) bowing of the epoxy capsule. Because of the order of magnitude difference between the densities of epoxy and of liquid helium, when the sidewalls flex the effect of the increased radius of the capsule dominates that of the extra mass due the slightly enlarged helium volume. ($I \propto MR^2$.)

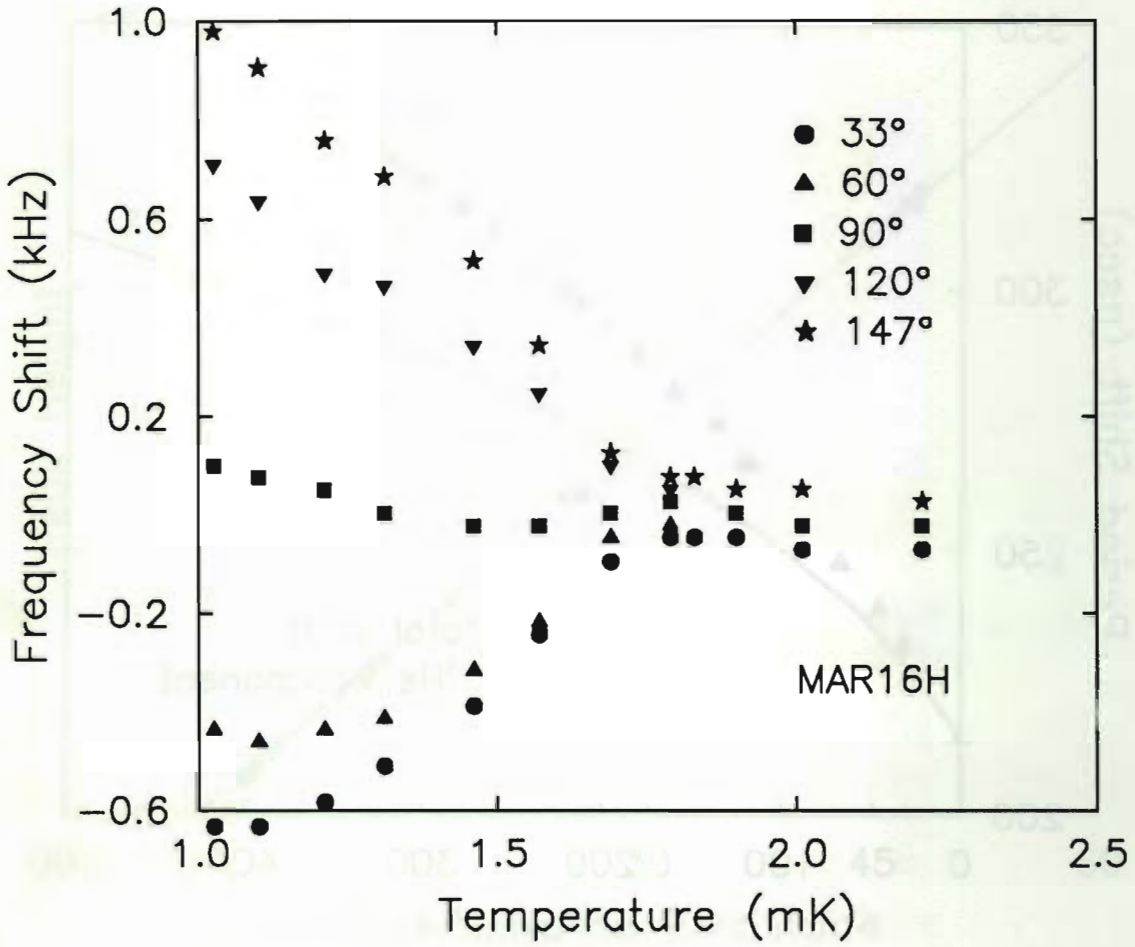

Figure B.5

This is a 9 bar, 31 mT pure ^{3}He data set in which measurements are recorded for five tip angles. The two subsequent plots show lineshape information under these conditions.

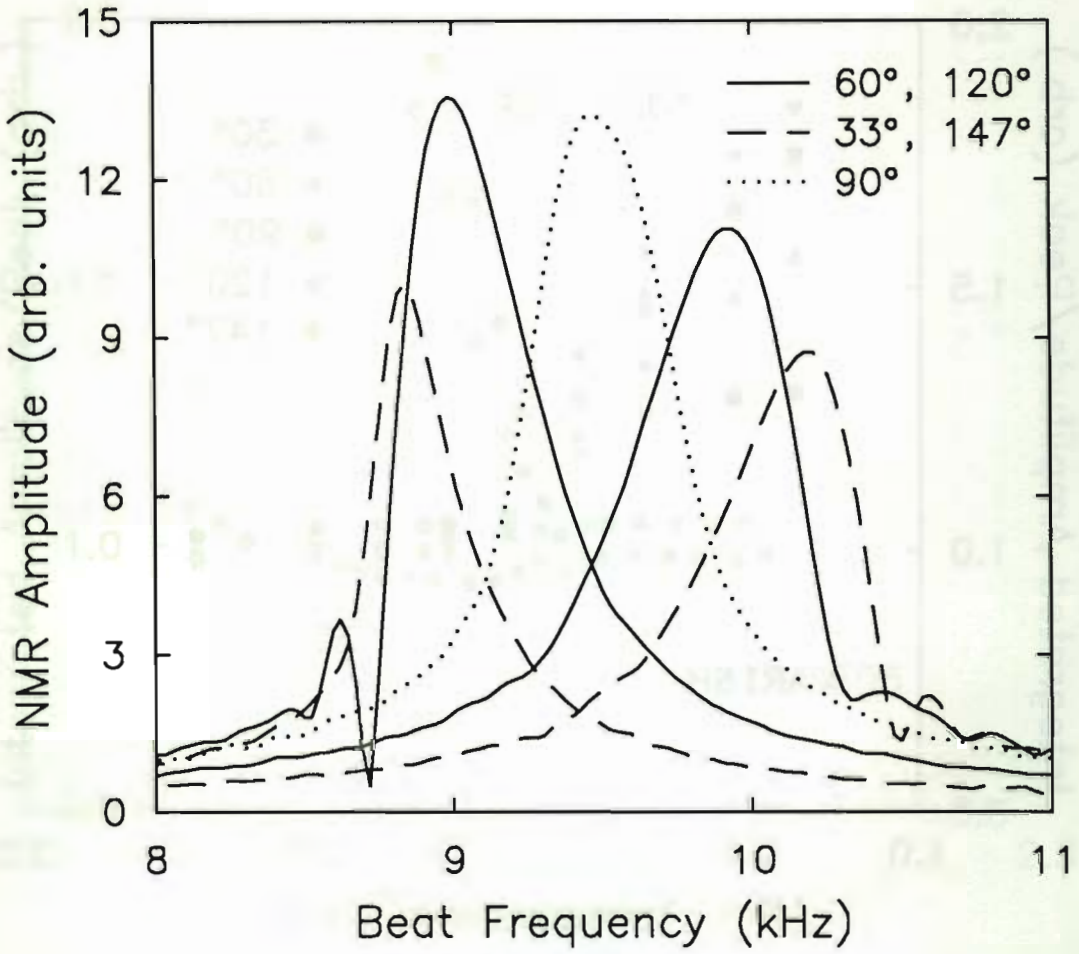

Figure B.6

These are the Fourier transformed free induction decays at 1.21 mK from the MAR16H data set. The pulses are applied at the 8.5 kHz position on the abscissa. The 147° pulse is 88 μsec in length. Two features are of note. First, there is an approximate mirror symmetry about 90°. Because of this reflection, we speculate that the feature causing the asymmetry in the lines is a nonlinear spin-wave. Second, the line*width* increases gradually with increasing angle of tip. This may be due to a dispersion of the tip angle in the presence of the substantial frequency shift. We have not examined the extent to which it could be an intrinsic effect.

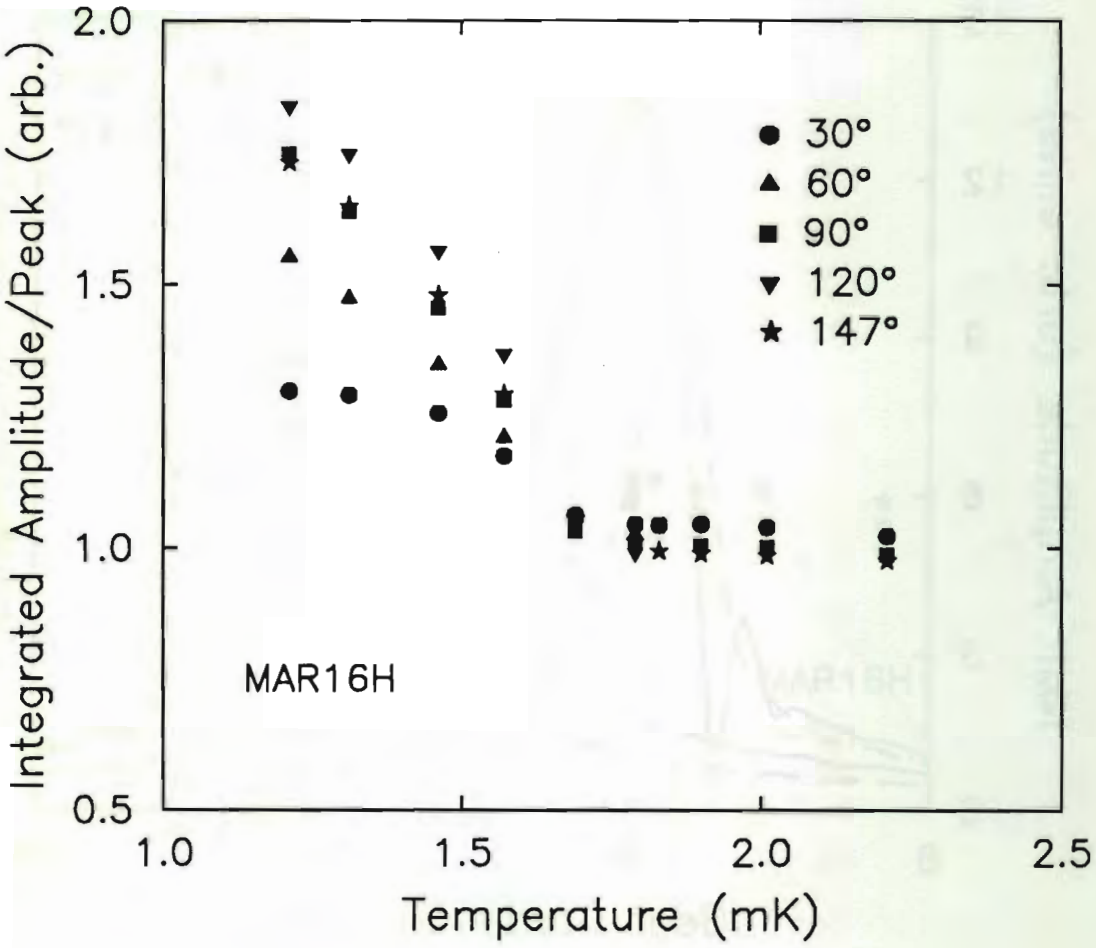

Figure B.7

Continuing with the data of Figures B.5 and B.6, this is a parametrization of the linewidth (integrated amplitude over peak height) in the vicinity of the superfluid transition.

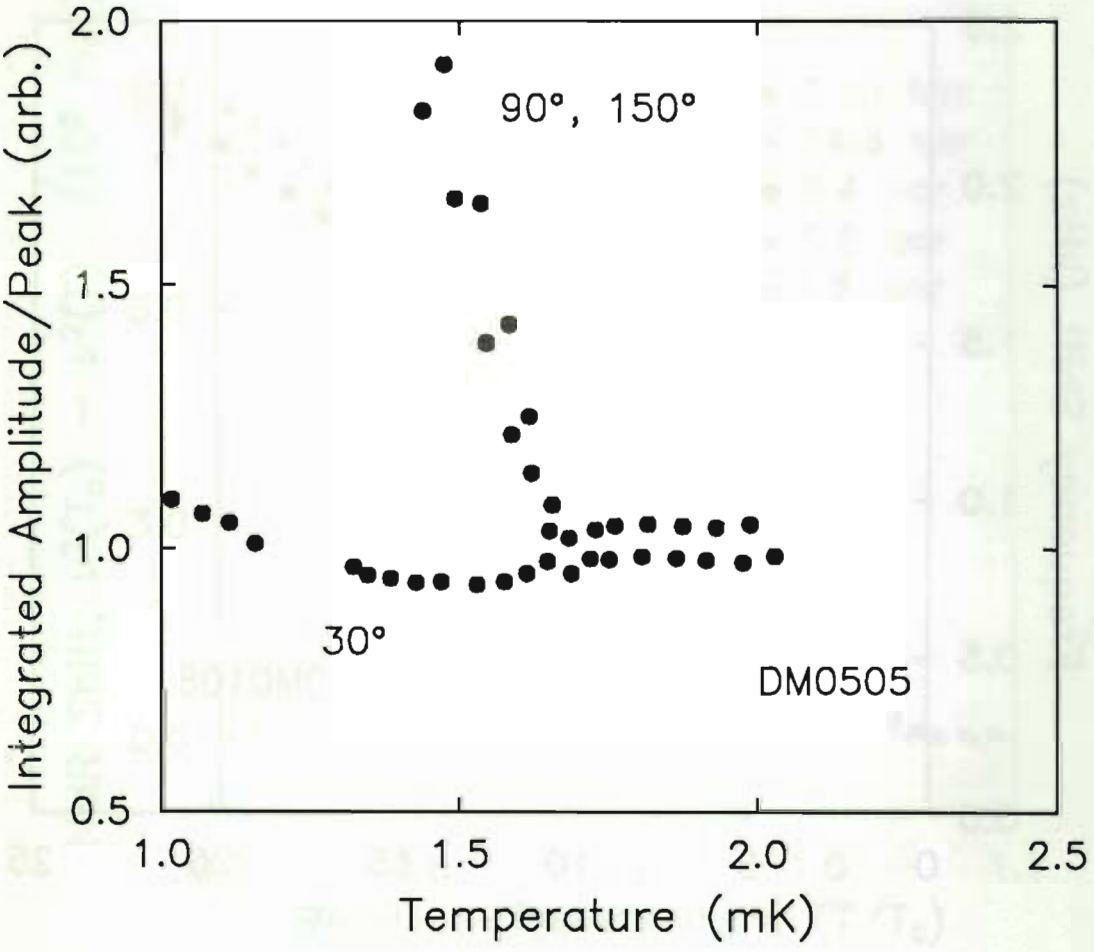

Figure B.8

The 'linewidth' when the surface ^{3}He layer has been displaced. The line actually *narrows* slightly at the transition for small tipping angles in this case. A systematic investigation for different pulse durations would be important for understanding this behaviour. The frequency shifts are larger here, without the solid layer magnetization, than in the preceding Figures.

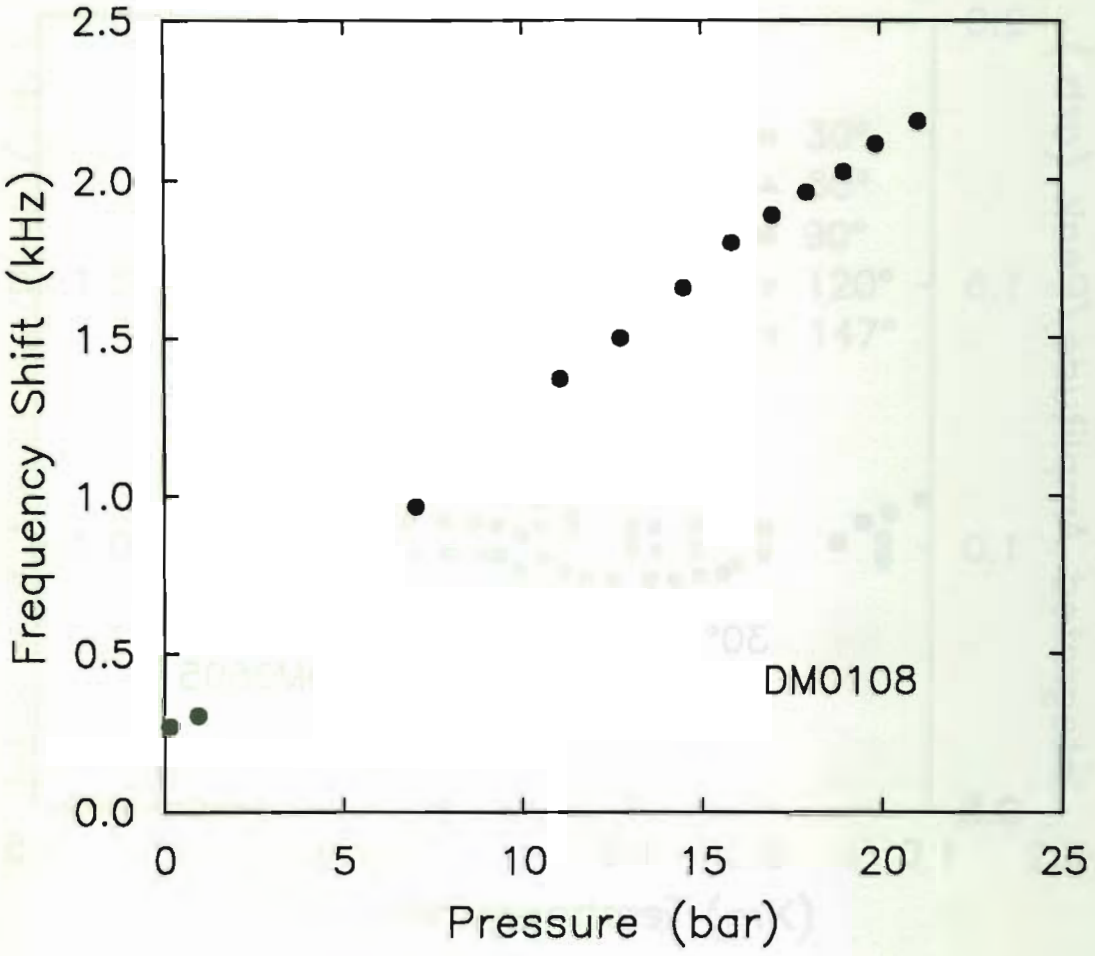

Figure B.9

The result of mapping a vertical slice of the P, T phase diagram by depressurization. The starting temperature was 0.63 mK, and the stage warmed to over 0.7 mK before we reached the lowest pressure (2.5 psia). The highest temperatures at which the distorted B phase is stabilized are expected to occur between 10 and 20 bar. We are surprised to find no evidence of a transition under these conditions.

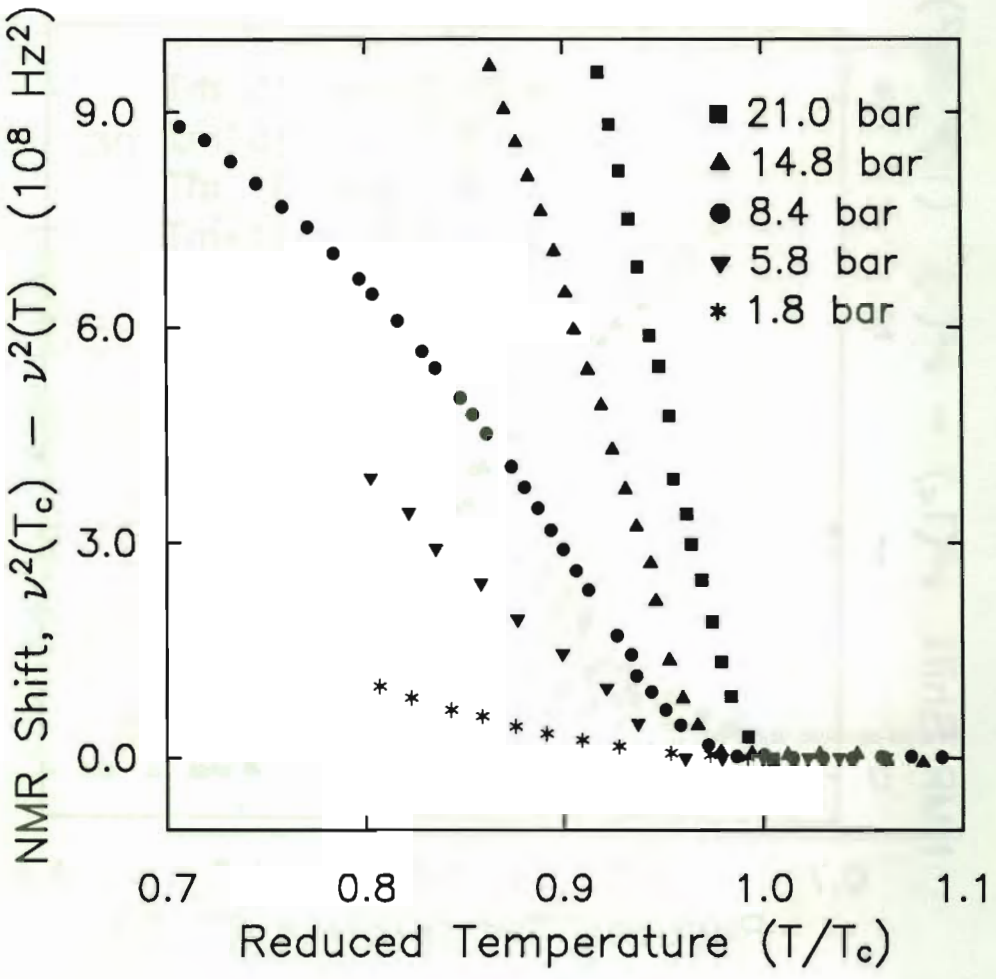

Figure B.10

A summary of pure ^{3}He NMR frequency shift data near the transition. All of these measurements are made with 30°pulses, and reflect the response of the total (liquid plus solid) magnetization. The particular data sets are: 21 bar, DM0106; 14.8 bar, DM1227; 8.4 bar, DM1208; 5.8 bar, DM0305; 1.8 bar, DM1219.

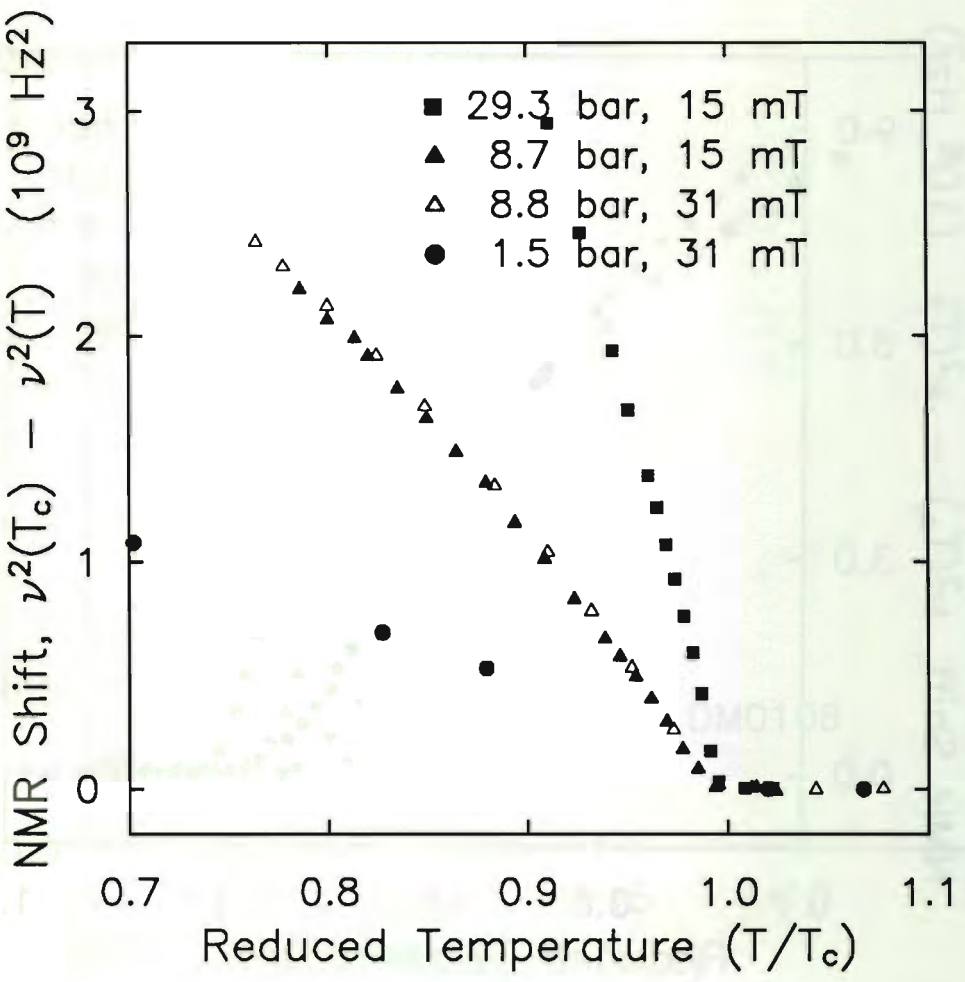

Figure B.11

The NMR frequency shift for ^{3}He with of order 70 μmole/m^2 ^{4}He coating the mylar surface. The measurements are with 30 °tips. The data sets are: 29.3 bar, DM0229; 8.7 bar, DM0227; DM0505, 8.8 bar; DM0424, 1.5 bar.

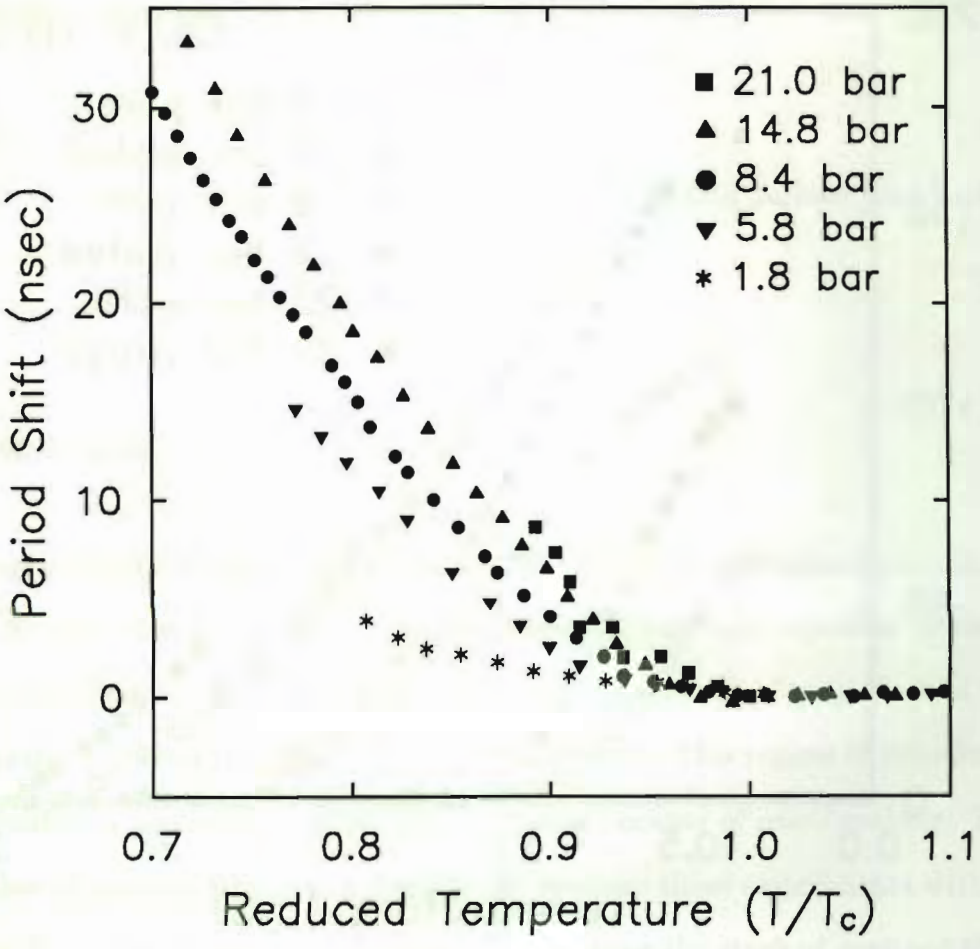

Figure B.12

Raw period shifts in the transition region. These curves are from the same runs as the NMR results of Figure B.10.

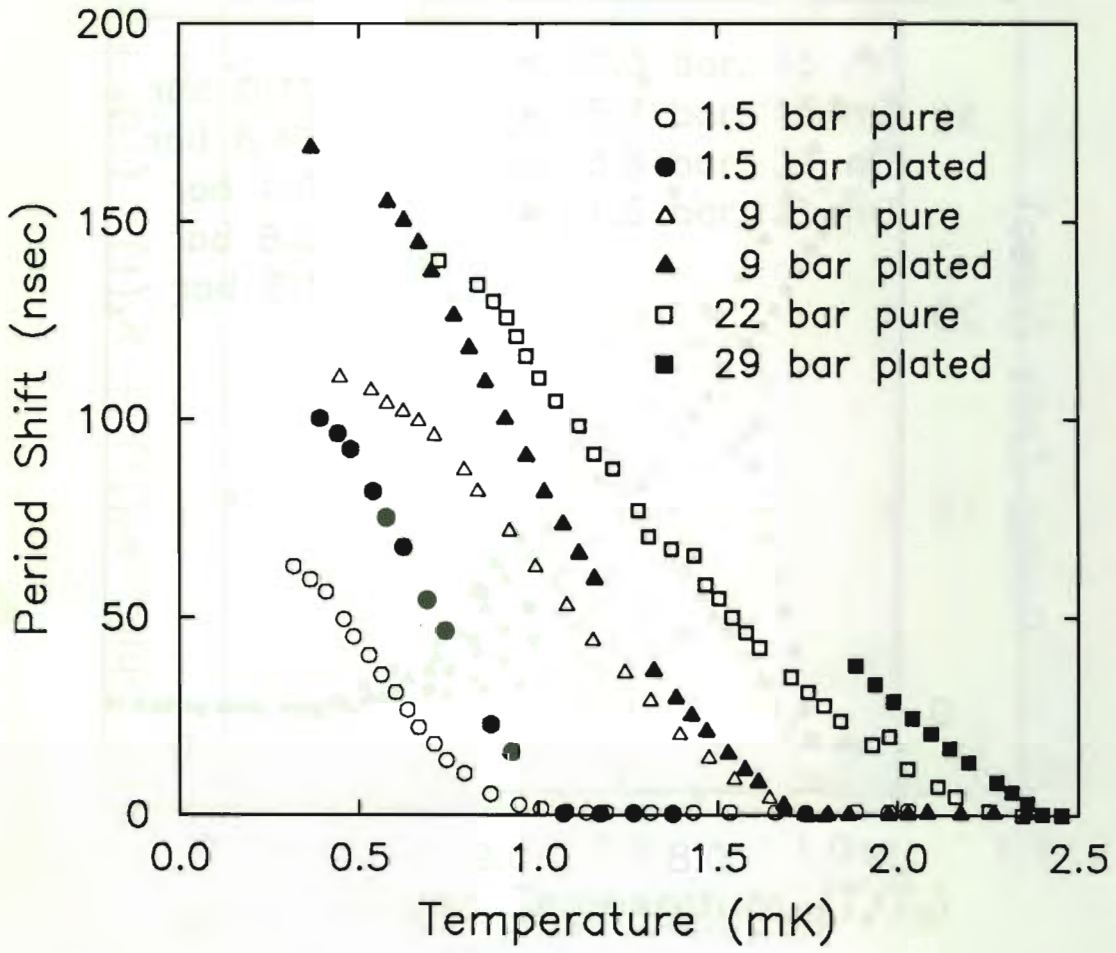

Figure B.13

A compendium of period shift data for pure ^{3}He and for ^{3}He with a surface layer of ^{4}He thick enough to form superfluid. The data sets are: 1.5 bar pure, DM0402; 1.5 bar plated, DM0424; 9 bar pure, DM0325; 9 bar plated, DM0505; 22 bar pure, DM0701; 29 bar plated, DM0229.

Appendix C

SQUID NMR

There is more to Guy Lafleur than hockey stick!

Guy Lafleur

C.1 Motivation

One of the most important results of this thesis is the demonstration that superfluid ^{3}He films can be produced, in the laboratory, on highly specular surfaces. The obvious application of this result is to the study of superfluidity in films of thickness comparable to or less than the bulk correlation length. This regime of two-dimensional superfluidity is inaccessible with diffuse surfaces because of pair-breaking. There are a number of reasons why it is preferable to continue these experiments with a single or a small number of saturated ^{3}He films, rather than the stack of confined films as in the present case. Our technique for establishing the gap between mylar sheets must be reaching its limits at 300 nm. Variations in the mylar thickness and surface dirt will cause a greater distribution of spacings if smaller average separations are attempted. A couple of problems prevent us from studying saturated films in the present cell or one like it. One is that we cannot cool the films through the substrate: we rely on the column of bulk liquid in the torsion rod for thermal contact. The other problem is that the films tend to capillary condense between the mylar sheets before filling the larger voids in the sample cell, making control of the film thickness very difficult. In this appendix, we describe a technique that makes it possible to survive the penalty

in signal-to-noise imposed by going to a single film, namely detection of NMR using a dc SQUID preamp. Some of this work appeared in Applied Physics Letters[1]. An attractive substrate for the ^{3}He experiment is a quartz microbalance. This allows measurement of the film thickness and can be used to probe the normal fluid slip and the superfluid density. Development of a quartz microbalance cell was begun in collaboration with Roman Movshovich.

C.2 The Spectrometer

An optimized nuclear magnetic resonance spectrometer operating at room temperature typically has a noise temperature of order 100 K [2], meaning that the device noise of the amplifier chain equals the Johnson noise from the probe when the latter is cooled to 100 K. Noise matching to colder probes has been achieved through use of a number of different cryogenically cooled amplifiers, all of which have different limits of applicability. Commercial rf and dc SQUIDs operating in a feedback mode have been used to detect NMR at frequencies below 100 kHz [3,4,5], and cold FETs have attained noise temperatures of order 5 K at megahertz frequencies[6]. Here we use a dc SQUID small signal amplifier as the front end of a receiver to demonstrate noise matching for pulse NMR probes down to millikelvin temperatures. The technique is similar to that used recently to detect nuclear quadrupole resonance[7].

The work is performed in a 1K cryostat constructed for testing of rf and low-noise electronics at low temperatures (Figure C.1). The low frequency wiring is brought in through two Detoronics 26 pin hermetic connectors. Adapter boxes plug into these connectors at the top of the cryostat and contain EMI filters for all of the lines. One connector is used for utility wiring, while the other launches a collection of shielded twisted pairs for use with the devices under test. Four of the signal pairs go to a junction box at 4 K where 1 kΩ series resistors provide additional filtering in concert

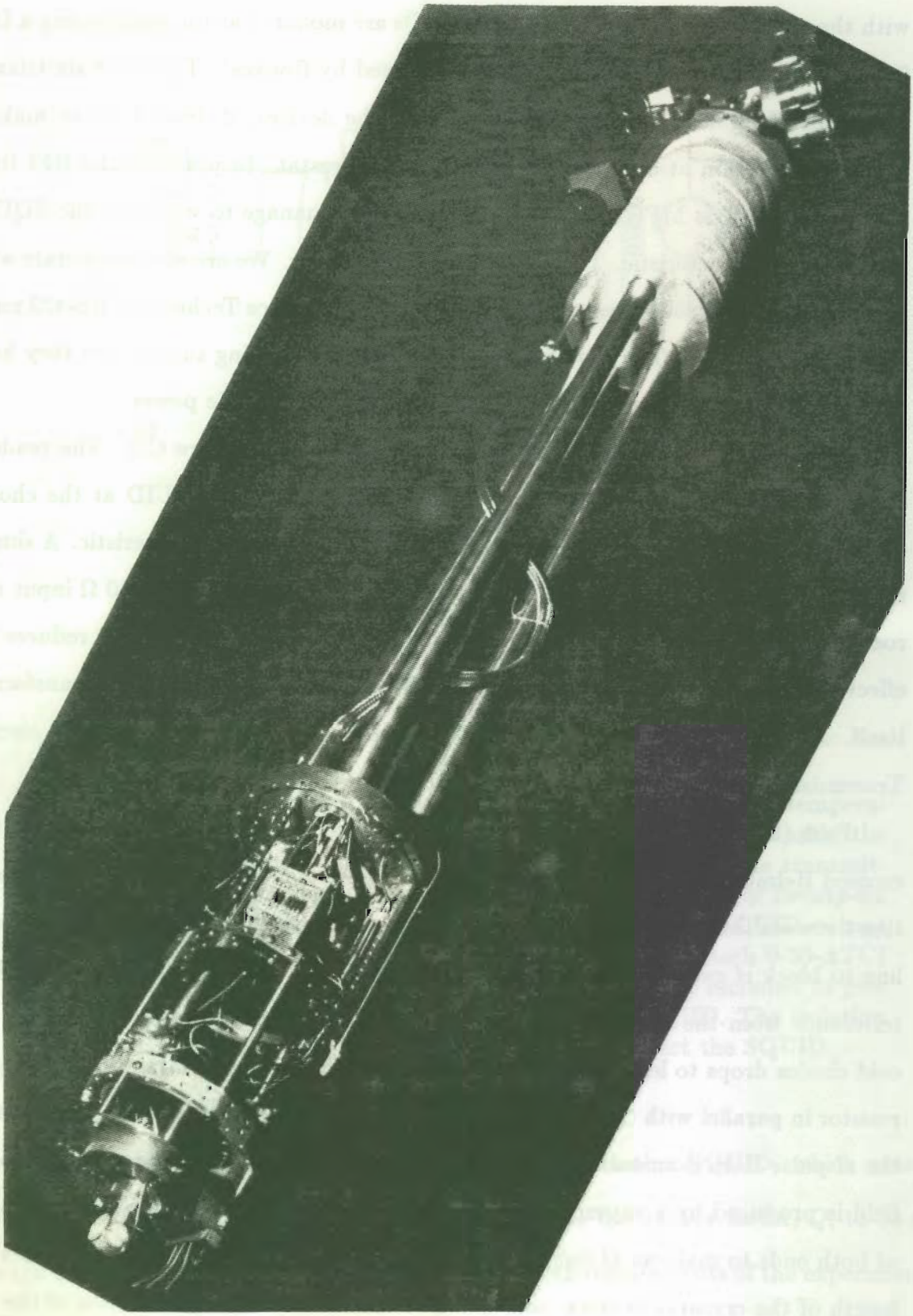

Figure C.1 The Big Dipper.

with the capacitance of the lines. The SQUIDs are mounted at this point using a DB-09 connectorized version of the packages designed by Roukes[8]. There are six triaxial cables for rf signals. This enables us to float the devices, if desired, or to make a ground connection at only one point inside the cryostat. In practice, the RFI from the Array Analysis MFI-1000 pulse sequencer does manage to wash-out the SQUID flux-voltage characteristic. This is the only real offender. We are able to operate with the LSI-11, the HP8566 spectrum analyzer and the Interface Technology RS-432 pulse sequencer operating. The Array Analysis unit has a switching supply, but they have made a provision for the user to supplant this with external dc power.

A schematic of the measurement system is shown in Figure C.2. The readout circuit is shown in part (b.). The dynamic resistance of the SQUID at the chosen operating point is 2 Ω, measured from the dc current-voltage characteristic. A simple resonant transformer is used to step this impedance up to match the 80 Ω input of a room temperature amplifier. Placing this transformer inside the cryostat reduces the effect of loss in the triaxial readout line, and lowers the added noise of the transformer itself. A tuned readout can be used here because of the high Q of the input circuit. Transmission line transformers can be used to obtain more bandwidth.

Part (a.) of the figure illustrates the input circuit. The NMR cell consists of crossed Helmholtz coils wound on accurately orthogonal forms. At 2 MHz, the isolation between the coils is 60 dB. Crossed diodes, traditionally placed in the transmitter line to block rf gate feedthrough, are mounted at 4 K to reduce the possibility of interference from the room coupling into the excitation coil. The attenuation of the cold diodes drops to less than 1 dB for rf levels greater than 2 volts rms. A damping resistor in parallel with the transmitter coil is necessary to prevent the ringdown after the rf pulse from dominating the recovery time of the receiver. The static magnetic field is produced by a superconducting solenoid wound on a brass coil form, capped at both ends to make an rf tight shield around the cell. The transmitter line runs the length of the cryostat as triax, converting to twisted pair at a penetration of the cell enclosure.

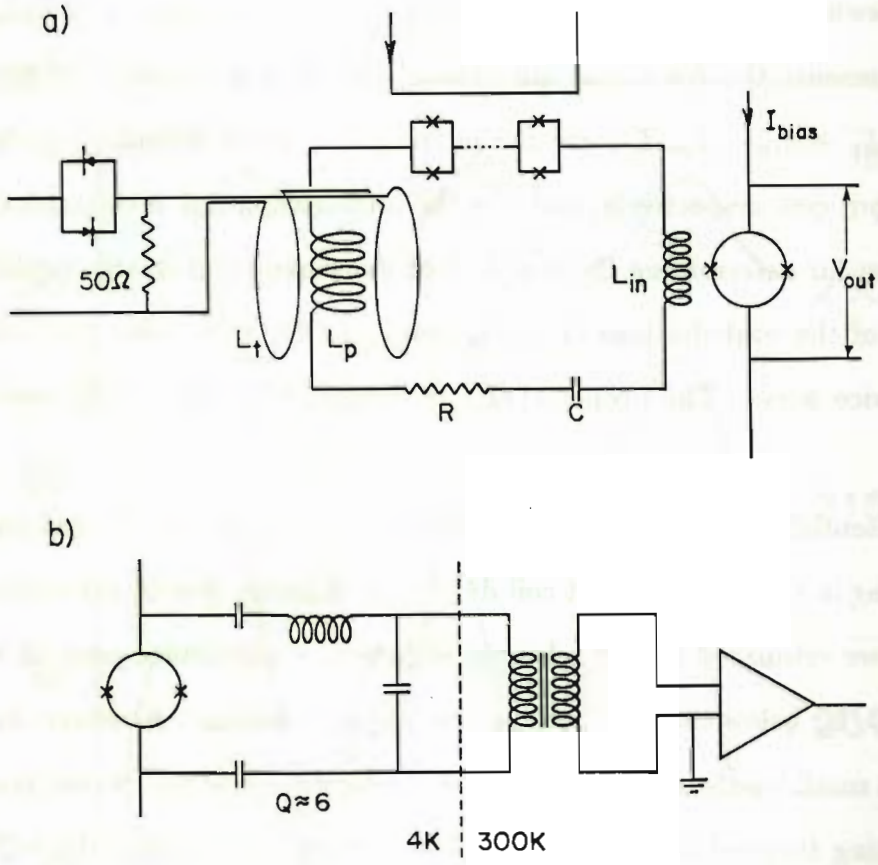

Figure C.2

a.) The series tuned input to the SQUID, shown with the low temperature components of the transmitter circuit. The spin system is inside the pickup coil L_p, which is an Helmholtz pair perpendicular to the transmitter coil L_t. The superconducting interferometer array consists of twenty-six devices and is modulated by a single control line. **b.)** The SQUID output impedance is matched to a room temperature amplifier (Trontech W50-ATC) using a cooled, tuned transformer. Blocking capacitors are included to prevent shunting of the dc bias current away from the SQUID. The isolation transformer (MCL T1-1T) is normally included to protect the SQUID.

The optimal circuit for coupling an NMR signal into a SQUID, which senses current, is a series tuned tank. In general, one wants the quality factor, Q, to be as large as possible without impinging on the bandwidth requirements of the experiment. The noise temperature of the detector is minimized when $Q\rho \approx 1$, the exact condition

being somewhat dependent on device-specific parameters. Here $Q = \omega(L_p + L_{in})/R$, and ρ represents the fractional inductance contributed by the SQUID input coil, $\rho = L_{in}/(L_p + L_{in})$. L_p, L_{in} are the inductances of the Helmholtz pickup coil and SQUID input coil, respectively, and R is the total dissipation in the tank circuit. This prescription for determining the coupling of the pickup coil to the SQUID results in a balance of the contributions of voltage and circulating current fluctuations to the overall device noise. The proper choice of component values is discussed briefly in Ref. 9.

An essential component of the input loop is a limiter to prevent large currents from flowing in the SQUID input coil during the rf pulse. For an early circuit without a limiter, we estimated that our largest rf pulses would induce emfs of 1 mV across the SQUID, far below the threshold for any physical damage. However, we found that even much smaller pulses significantly alter the bias point of the device, presumably by redistributing trapped flux lines. Without feedback, this renders the SQUID useless as an amplifier. Flux-voltage transfer characteristics of the device (PT-1, wafer 3-1, A3) used for the measurements reported below are shown in Figure C.3. This device is from a test vehicle having high critical currents and exhibiting hysteresis in the transition to the normal state. There is, however, a useful range of bias currents (near $4I_c$, where I_c is the critical current per junction) where the shape is nearly sinusoidal and the modulation depth is not too small. The dashed line in Figure C.3 is tangent to a typical operating point in small-signal mode. This point is selected by a dc flux bias from a control line on the SQUID chip.

An elegant solution to this problem of pulse-recovery has been devised by Hilbert et al.[7], who connect a string of Josephson junctions in series with the input coil. The junctions act as a current clamp, in much the same way as diodes are often used to clamp the voltage at the input of a conventional NMR receiver. The performance of the limiter is largely independent of the amount of hysteresis in the current-voltage

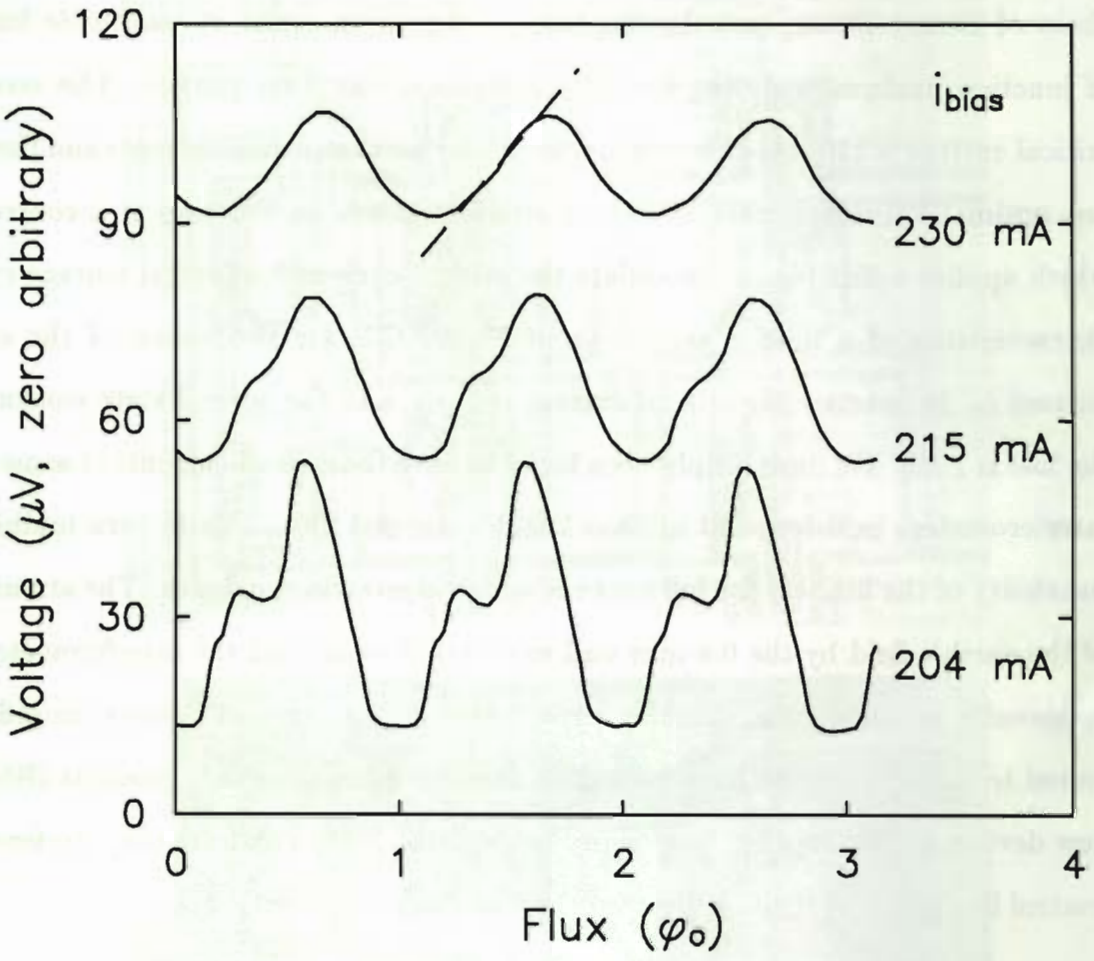

Figure C.3

Some flux-voltage characteristics, showing the periodic response of the SQUID to flux applied in units of the fluxoid quantum, $\phi_o = 2 \times 10^{-15}$ Wb. The slope of the dashed line is the gain at a typical operating point.

characteristic. The junctions remain in the zero voltage state once the signal amplitude has decayed below the maximum critical current, because the signals are ac. In addition to SQUID protection, a key advantage of this technique is the ability to drastically reduce pulse recovery times for high Q circuits. The deadtime of the receiver is basically determined by the ringdown of the tank from the critical current of the limiter, with the characteristic time constant Q/ω.

Figure C.4a is a photograph illustrating the limiter used for the present work. A chain of twenty-six superconducting interferometers in series, it was made for tests of junction uniformity during the IBM Josephson computer project. The zero field critical current is 110 μA, orders of magnitude larger than signal currents and therefore not optimal. Running past all of the interferometers on the chip is a control line which applies a flux bias to modulate the critical current[10]. Typical voltage-current characteristics of a limiter are shown in Figure C.5, for two values of the control current i_c. In practice the critical current is 5 μA, and the normal state resistance of the line is 1 kΩ. We have simply been lucky to have the critical currents of some of the interferometers held low, but not too low, by trapped flux. This in turn inhibits the tunability of the limiter, the full range of which is given in the figure. The attenuation of the earth's field by the 0.8 mm wall mu-metal box around the interferometer chip apparently is inadequate. Smaller area, lower critical current devices more ideally suited to this application have been fabricated by Bill Gallagher's group at IBM. The new devices are monolithic, as seen in Figure C.4b. Stray flux from the interferometer control line has a negligible effect on the bias point of the SQUID.

C.3 Performance

Figure C.6 shows a noise spectrum taken with 73 dB of gain following the SQUID, which is biased to have gain $dV/d\phi = 40\mu V/\phi_0$. The SQUID is of the type developed by Ketchen and Jaycox[11], having a 90 pH self inductance and a 19 turn input coil with $L_{in} = 35$ nH. The value of $Q\rho$ is 0.64, determined by $L_p = 2.2\mu$H and $R = 0.65\Omega$. The peak in the figure is due to the Johnson noise of the tank circuit. The off-resonance background level is the noise of the readout, confirmed by biasing the SQUID in the zero voltage state. The present readout scheme is not matched to the output noise of the SQUID at its optimal bias points, so we are unable to resolve the contribution of the SQUID to the noise level off resonance. This limits the noise temperature of the

a.

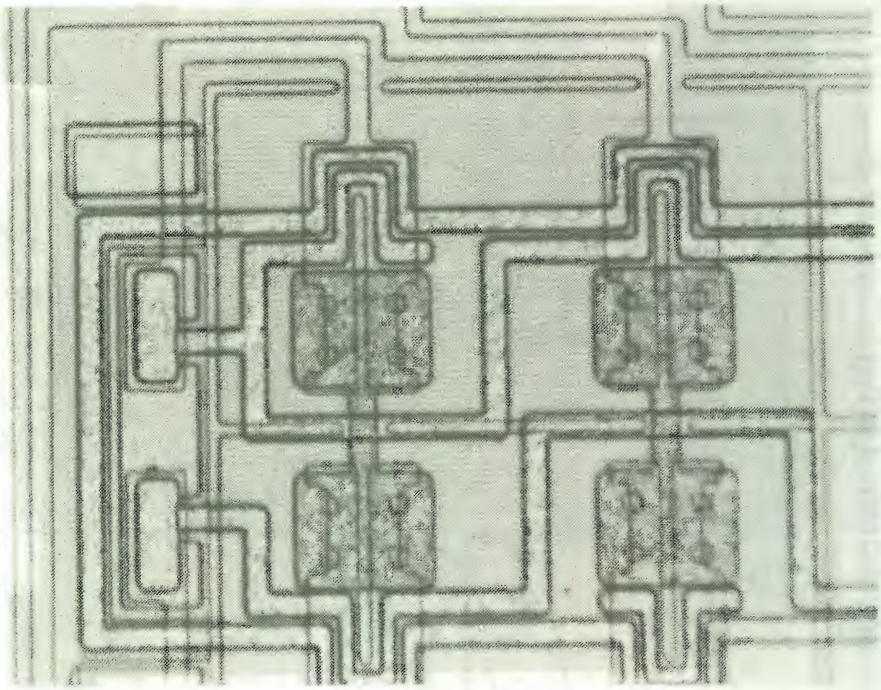

b.

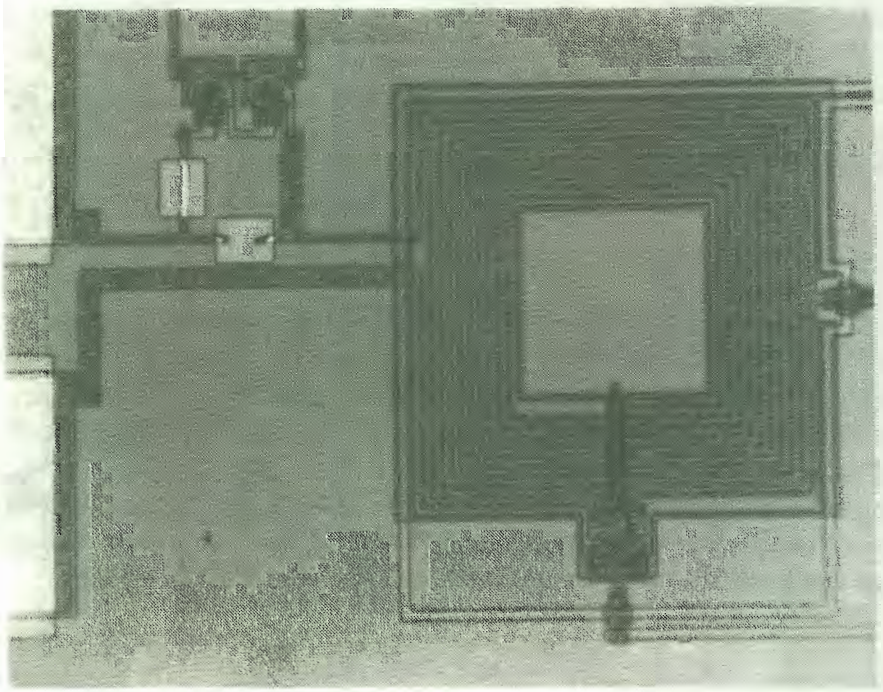

Figure C.4

a.) A section of the array of interferometers given to us by Bill Gallagher for use as a Q-killer. We use only one column of devices, 26 in all. Control lines run horizontally past all of the devices, coupling flux in through the one-half turn 'loops'. (1000×.) **b.)** A photograph showing the new monolithic design. (500×.)

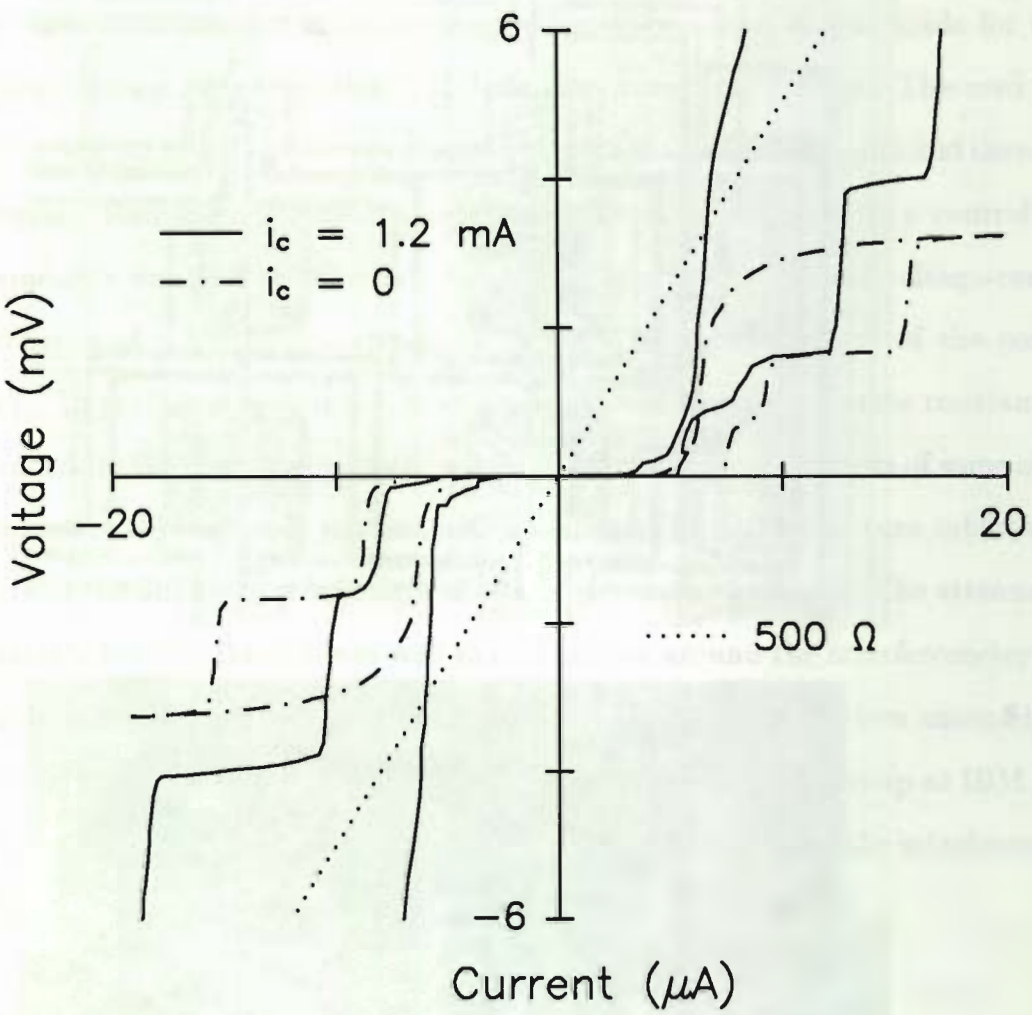

Figure C.5

The voltage-current characteristic of a typical limiter. The response is very well suited to the present application. The critical current and tuning range both would increase with improved magnetic shielding.

receiver to 300 mK. A cryogenically cooled FET second stage amplifier would take full advantage of the low SQUID noise. The solid line is a fit to the spectrum which can be used to extract various circuit parameters, in particular the temperature of R relative to some fixed point. The inset of Figure C.6 shows this temperature plotted against the reading of a germanium resistance thermometer which is in good thermal contact

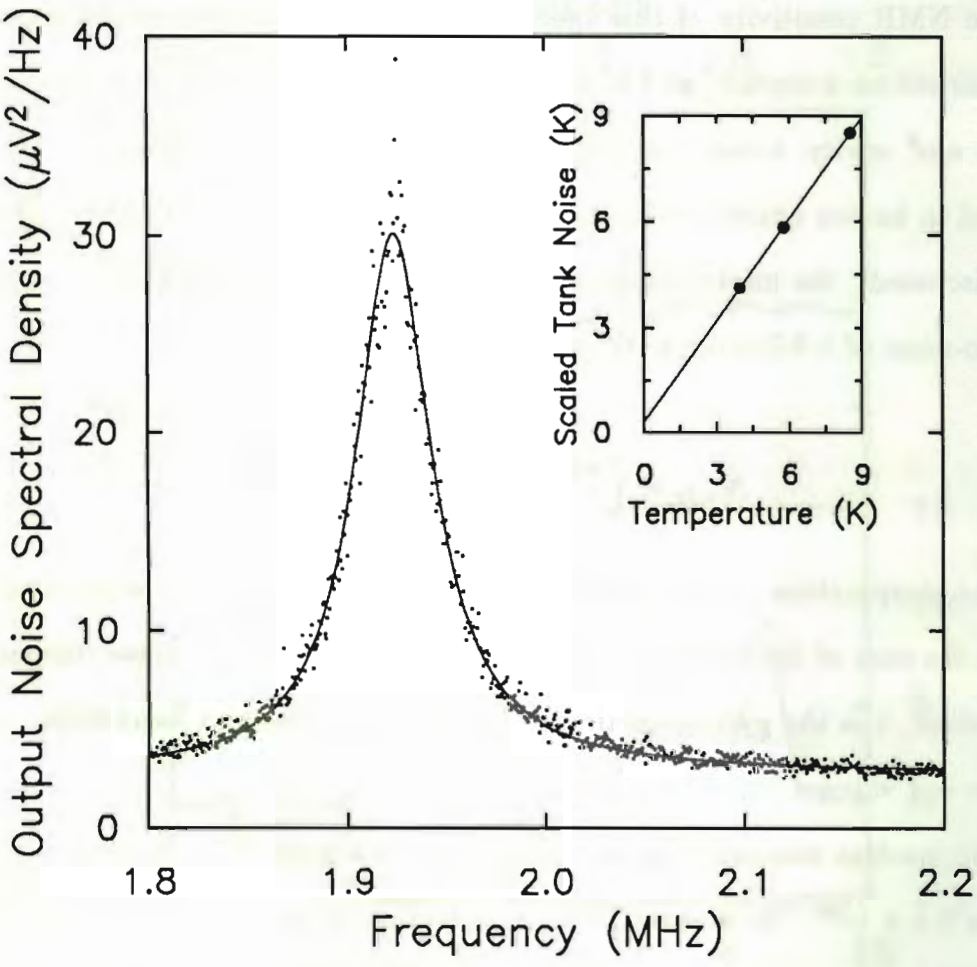

Figure C.6

A typical output noise spectrum, showing the Johnson noise peak from the tank circuit at 4 K. The noise level far off resonance is the contribution of the readout amplifier. The solid line is a nonlinear least-squares fit used to extract the temperature. This noise temperature is shown in the inset as a function of the temperature of the dominant component of the tank dissipation.

with a heater and with a short length of Advance wire, the dominant component of R. We attribute the small offset of the vertical intercept to an extra resistance in the tank which is not coupled to the heater, most likely the capacitor dissipation. If the effective flux noise of the SQUID is $10^{-6}\phi_0/Hz^{1/2}$, a value we have measured at lower frequencies using an rf SQUID readout (and the dc SQUID still at 4 K), a 30 mK noise temperature at 2 MHz is possible using a lower noise second stage.

The NMR sensitivity of this spectrometer is tested by measuring signals from ^{3}He adsorbed on a surface, at 4 K and in a static field of 60 mT. The sample volume is a 0.8 cm^3 cavity, loosely packed with 2000Å fluorocarbon spheres. ^{3}He can be admitted in known quantities from a room temperature reservoir. As we have previously discussed[9], the minimum discernible number of spins (defined by the condition signal-to-noise of 1 following a 90° pulse) can be calculated to be

$$N_{mds} = \left(\frac{4k_B T^*}{\hbar\omega}\right)\left(\frac{4k_B T_{sys} v\ \delta f}{\mu_0 \gamma^2 \hbar^2 \omega Q}\right)^{\frac{1}{2}} \qquad \text{(C.1)}$$

Here the temperature of the spin system is T^*, and the system noise temperature, T_{sys}, is the sum of the temperature of the tank circuit and the noise temperature of the receiver. γ is the gyromagnetic ratio, δf the measurement bandwidth, and v an effective coil volume.

Two nuclear resonance signals are shown in Figure C.7. In this case the cell contains 1.5×10^{20} ^{3}He atoms. The free induction decay is excited by a 16° tipping pulse lasting 40 μsec, and measured in a 200 kHz bandwidth. The recovery time is measured by injecting a small coherent signal and found to be 15 μsec. The linear dynamic range of the amplifier, also checked in this manner, is 90 dB in a 1 Hz bandwidth. The 1 dB compression point is at an input signal level of 0.25 ϕ_0 peak-to-peak, about what one expects for a sinusoidal transfer characteristic. We can also use the SQUID amplifier to detect spin echoes, as shown in Figure C.7(b). The observed signals correspond to $N_{mds} = 4 \times 10^{18}$ spins, measured in a 200 kHz bandwidth about 1.93 MHz, in good agreement with Equation C.1 for T^* and T_{sys} both 4 K. For lower temperature operation, if we take $T_{sys} = 200$ mK and $T^* = 5$ mK, then N_{mds} corresponds to one monolayer of surface ^{3}He spins (Curie-Weiss susceptibility) on a 1 cm^2 substrate. An equivalent signal is obtained from a 35 nm thick film of liquid with a magnetic Fermi temperature of 400 mK.

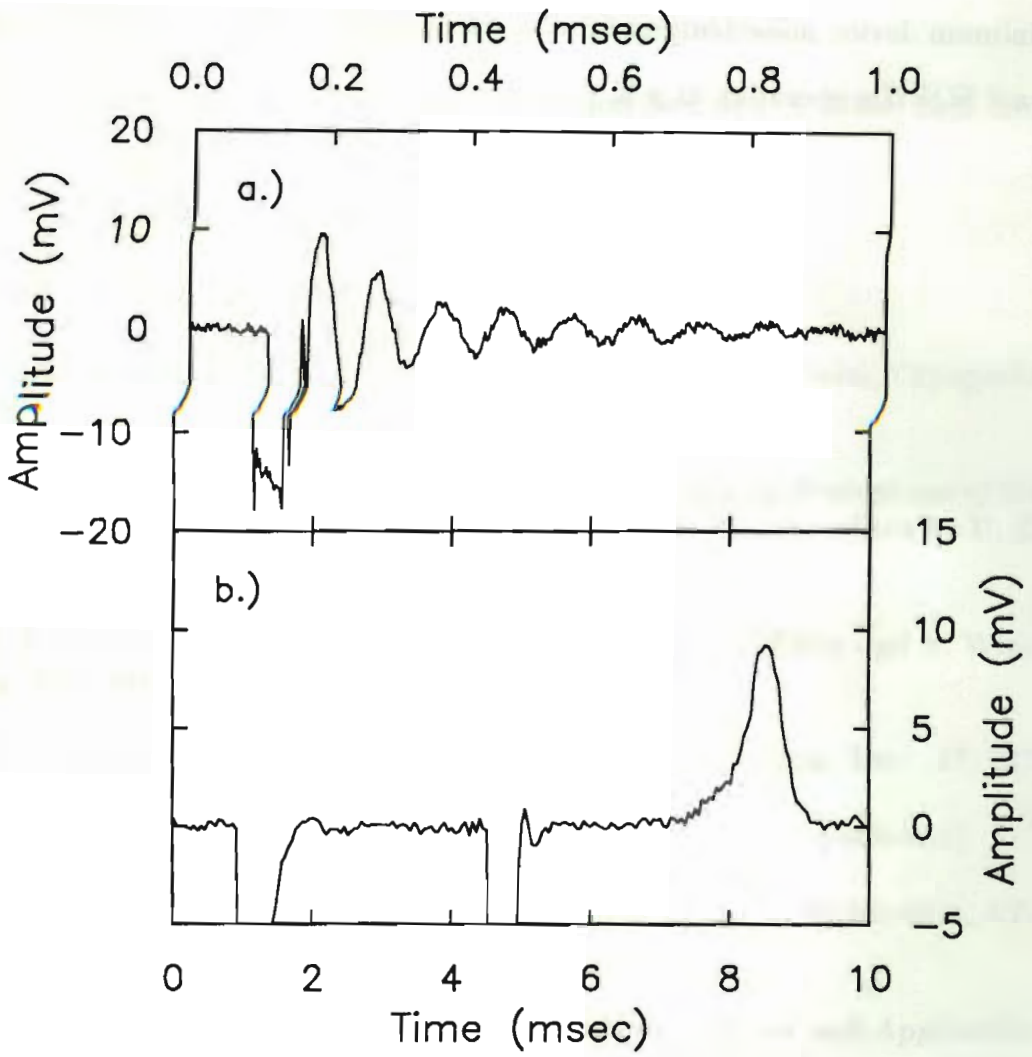

Figure C.7

a.) A ^{3}He free induction decay. The tipping pulse begins 100 μsec into the trace, and lasts for 40 μsec. The tipping angle was 16°, and the total number of spins was 1.5×10^{20}. The SQUID was followed by 73 dB of gain, and the signal recorded using a 200 kHz bandwidth. **b.)** A spin echo sequence, also seen in a 200 kHz bandwidth.

In conclusion, we have demonstrated NMR detection at 1.9 MHz and 4 K using a dc SQUID small signal amplifier. The SQUID is the best device presently available to match to the very low thermal noise of NMR probes at millikelvin temperatures, for signal frequencies, f, below about 100 MHz. The advantage held by the SQUID over other types of amplifier increases as the probe temperature is lowered towards

the minimum device noise temperature, approximately 10 mK $\times f$ (MHz) for state-of-the-art SQUIDs operating at 4 K.

References for Appendix C

C.1 M.R. Freeman, R.S. Germain, R.C. Richardson, M.L. Roukes, M.B. Ketchen and W.J. Gallagher, Appl. Phys. Lett. **48**, 300 (1986).

C.2 D.I. Hoult, Prog. NMR Spectr. **12**, 41 (1978).

C.3 R.A. Webb, Rev. Sci. Inst. **48**, 1585 (1978).

C.4 G.J. Ehnholm, J.P. Ekström, M.T. Loponen and J.K. Soini, Cryogenics **19**, 673 (1979).

C.5 A.K.M. Wennberg, L.J. Friedman and H.M. Bozler, in *Proceedings of the Seventeenth International Conference on Low Temperature Physics,* edited by U. Eckern *et al.* (North-Holland, Amsterdam 1984), p. 265.

C.6 P. Styles, N. Soffe, C. Scott, D. Cragg, F. Row, D. White and P. White, Jour. Mag. Res. **60**, 397 (1984).

C.7 C. Hilbert, J. Clarke, T. Sleator and E. Hahn, Appl. Phys. Lett. **47**, 637 (1985).

C.8 M.L. Roukes, Ph.D. Thesis, Cornell University, 1985 (unpublished).

C.9 M.R. Freeman, M.L. Roukes, R.S. Germain and R.C. Richardson, *LT-17 Proceedings,* p. 267.

C.10 See, for example, A. Barone and G. Paterno, *Physics and Applications of the Josephson Effect,* Wiley and Sons, New York 1982, Sec. 12.3.

C.11 M.B. Ketchen and J.M. Jaycox, Appl. Phys. Lett. **40**, 736 (1982).